Challenge Journal of
STRUCTURAL MECHANICS

Vol.3 No.1 (2017)

North Anatolian Fault Zone Poisson method

building codes columns continuous

girder bridge corrosion durability

dynamic analysis dynamic response

earthquake earthquake hazard finite

element analysis finite element

method optimization reinforced

concrete seismic analysis seismic

design seismic isolation seismic response

teaching-learning based optimization wind

ISSN 2149-8024

TULPAR
ACADEMIC PUBLISHING

Challenge Journal of Structural Mechanics

E-mail: *cjsmec@challengejournal.com*

Web page: *cjsmec.challengejournal.com*

TULPAR Academic Publishing
www.tulparpublishing.com

Challenge Journal of Structural Mechanics

CONTENTS

TULPAR ACADEMIC PUBLISHING

Challenge Journal of Structural Mechanics

Analytical solution for bending and buckling response of laminated non-homogeneous plates using a simplified-higher order theory

Ferruh Turan *, Muhammed Fatih Başoğlu, Zihni Zerin

Department of Civil Engineering, Ondokuz Mayıs University, 55139 Samsun, Turkey

ABSTRACT

In this study, analytical solutions for the bending and buckling analysis of simply supported laminated non-homogeneous composite plates based on first and simplified-higher order theory are presented. The simplified-higher order theory assumes that the in-plane rotation tensor is constant through the thickness. The constitutive equations of these theories were obtained by using principle of virtual work. Numerical results for the bending response and critical buckling loads of cross-ply laminates are presented. The effect of non-homogeneity, lamination schemes, aspect ratio, side-to-thickness ratio and in-plane orthotropy ratio on the bending and buckling response were analysed. The obtained results are compared with available elasticity and higher order solutions in the literature. The comparison studies show that simplified-higher order theory can achieve the same accuracy of the existing higher order theory for non-homogeneous thin plate.

ARTICLE INFO

Article history:
Received 12 January 2017
Accepted 16 February 2017

Keywords:
bending response
buckling response
shear deformation
higher-order theory
non-homogeneous plates
non-homogeneity effect

1. Introduction

Laminated composite plates are used in air craft industry, defense industry and especially structural strengthening applications. Usage of composite plates have been expanded due to their light-weight, high stiffness and high strength features compared to classical structural materials. For using them efficiently in above fields, their structural and dynamical behavior and also an accurate knowledge of their characteristic behaviors under various loading and boundary conditions are requested (Patel, 2014; Sadoune et al., 2014; Zerin et al., 2016).

Kinematic approaches for first-order shear deformation theory (FSDT) are an extension of the classical plate theory by including linear transverse shear deformation occurred through the plate thickness. However, the classical elasticity theory represents that transverse shear stress is distributed parabolically through the plate thickness. Because of that, FSDT requires a shear correction factor (K) to modify this parabolic shear stress distribution. Higher-order shear deformation theories (HSDTs) contain higher order variations of the displacement through the thickness and perform the equilibrium conditions obtained from elasticity theory on the top and bottom surface of the plate without using any shear correction factors.

Materials are generally considered as homogeneous and isotropic in classical elasticity theory because of simplicity in calculation. On the contrary, material anisotropic properties should be included to be able to obtain more accurate and sensitive analysis results. However, number of elastic constants increase in an anisotropic body. In such a body should be analysed by utilizing anisotropic elasticity theory in order to determine stress and strain (Kolpakov, 1999; Lal, 2007).

The linear elasticity theory of non-homogeneous materials is based on Hooke Law, and material elastic properties differ functionally through the thickness of the plate. This is more realistic in terms of mathematical and physical modeling. In this case, the physical characteristic of the material changes point to point continually and it becomes the continuous function of the point coordinates (Beena and Parvathy, 2014; Fares and Zenkour, 1999; He et al., 2013; Kolpakov, 1999; Leknitskii and Fern, 1963; Schmitz and Horst, 2014; Sofiyev and

* *Corresponding author*. Tel.: +90-362-3121919 ; E-mail address: ferruh.turan@omu.edu.tr (F. Turan)
ISSN: 2149-8024 / DOI: https://doi.org/10.20528/cjsmec.2017.02.001

Kuruoglu, 2014; Sofiyev et al., 2008; Stürzenbecher and Hofstetter, 2011; Zenkour and Fares, 1999).

A new simple first order shear deformation theory almost the same as CLPT was derived in terms of parameters such as equation of motion and boundary conditions (Thai and Choi, 2013a). Lots of theories acceptable for homogeneous laminated plates were modified into the behaviours of buckling and free vibration of non-homogeneous rectangle plates. The effects of non-homogeneity and thickness ratio on natural vibration and critical buckling load were determined. In this study, it is expressed that CLPT is not convenient method to investigate the structural behaviours of non-homogeneous plates (Fares and Zenkour, 1999). The non-homogeneity effects on free vibration of non-homogeneous isotropic circular plates of non-linear thickness were analysed. The non-homogeneity was related to variation of Young's modulus and density of plate material (Gupta et al., 2006). The non-homogeneity behaviours of non-homogeneous rectangle plates were pointed out by means of small parameter method, and the effects of non-homogeneity and material anisotropy on deflection and stress values were evaluated (Zenkour and Fares, 1999).

Zenkour (2011) investigated bending of exponentially graded sandwich plate by using HSDT and Sinusoidal Shear Deformation Theory (SSDT) and Zenkour et al. (2007) presented an exact solution for linear bending analysis of non-homogeneous variable thickness orthotropic plates. Librescu and Khdeir (1988) analysed stresses and displacements of symmetric cross-ply laminated elastic plates using HSDT. Gupta et al. (2007) presented variations of vibration based on thermal effects at non-homogeneous orthotropic rectangular plate having parabolically varying thickness. Kim et al. (2009) suggested a two variable refined plate theory without using shear correction factor for laminated composite plates. Fares and Zenkour (1999) analysed the buckling and free vibration response of non-homogeneous plates with various plate theories, and they deduced that non-homogeneity effect on the plate stability is significant. Neves and Ferreira (2016) examined the free vibration and buckling problem of composite plate using by global meshless method. Vescovini and Dozio (2016) developed an approximate method to analyse the vibration and buckling problem of plates. The method based on Ritz solution and a variable kinematic approach. Yu et al. (2016) investigated the thermal buckling for functionally graded plates (FGPs) with internal cracks using a new numerical method based on the first-order shear deformation theory. They assumed that the mechanical properties of FGPs varied through the thickness as a power function. Mojahedin et al. (2016) analysed the stability problem of functionally graded circular plate consisted of porous materials using higher-order plate theory. They assumed that the porosity varies as a function through the thickness. Saheb and Aruna (2015) developed a coupled displacement field method to investigate the buckling response of moderately thick plates. Komur and Sonmez (2015) analysed the effect of cut-outs or openings on the plate stability. They assumed that perforated plates may lose their stability under axial compression. So, they considered perforated square and rectangular plates to study the buckling behavior of plates using finite element method. Sreehari and Maiti (2015) developed a finite element formulation for buckling and post-buckling response of laminated composite plates. This formulation based on inverse hyperbolic shear deformation theory and satisfied that non-linear shear stress distributions and zero shear stress on the top and bottom surfaces of the plate. Papkov and Banerjee (2015) presented a new method to analyse the free vibration and buckling problems of rectangular orthotropic plates. They simplified the boundary value problem by developing the superposition principle. So, the exact results for free vibration and buckling of orthotropic plates can be practically obtained by using this method. Kulkarni et al. (2015) investigated bending and buckling behavior of FGPs by using inverse trigonometric shear deformation theory. The material properties of plates considered as an exponential variation through the thickness. Reddy et al. (2015) studied the buckling analysis of FGPs had variable material properties through the thickness. They investigated the thickness stretching effect on the buckling of plates and the study considered non-zero shear stress on the top and bottom surfaces of plates.

2. Mathematical Model

Consider a fiber – reinforced rectangular laminated plate with aspect ratio a/b and total thickness h and, consisted of N orthotropic non-homogeneous layers with orientation angles $\theta_1, \theta_2, \ldots, \theta_N$ as shown in Fig. 1. The coordinate system is assumed that the middle plane of the plate coincides with xy plane, and z axis is perpendicular to the middle plane.

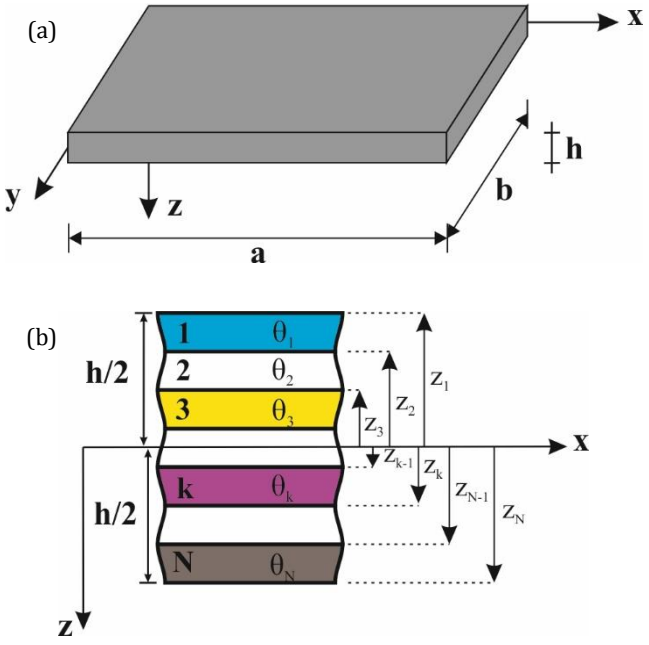

Fig. 1. Coordinate system (a) and lamination scheme (b) used for a typical laminate.

The first- and simplified higher-order theories used in the present study is based on the following displacement field (Reddy, 2004; Senthilnathan et al., 1988);

$$u(x,y,z) = u_0(x,y) - z\left[\alpha\frac{\partial w^b}{\partial x} - \beta\varphi_x + \gamma\frac{4z^2}{3h^2}\frac{\partial w^s}{\partial x}\right],$$

$$v(x,y,z) = v_0(x,y) - z\left[\alpha\frac{\partial w^b}{\partial y} - \beta\varphi_y + \gamma\frac{4z^2}{3h^2}\frac{\partial w^s}{\partial y}\right],$$

$$w(x,y,z) = \beta\, w + \alpha\, w^b + \gamma\, w^s, \quad (1)$$

where (u_0, v_0, w) are the displacement functions of the plate's mid-plane, ϕ_x and ϕ_y are the slopes in the xz and yz planes by reason of bending only and (α, β, γ) are arbitrary coefficients defined as;

1. Higher-order shear deformation theory (HSDT):
$\alpha = 1, \beta = 0, \gamma = 1.$
2. First-order shear deformation theory (FSDT):
$\alpha = 0, \beta = 1, \gamma = 0.$

In this study, simplified Reddy's theory is considered for HSDT. This theory is assumed that the slopes in the xz and yz planes (ϕ_x and ϕ_y) remains constant through the thickness and the transverse displacement w can be divided into bending (w^b) and shear (w^s) parts (Senthilnathan et al., 1988);

$$\frac{\partial\varphi_x}{\partial y} = \frac{\partial\varphi_y}{\partial x} \quad , \quad w = w^b + w^s \quad , \quad \varphi = -\nabla w^b . \quad (2)$$

The strains for FSDT and HSDT related to the displacements (1) can be presented as (Fares and Zenkour, 1999; Mojahedin et al., 2016; Reddy et al., 2015; Senthilnathan et al., 1988; Shahbaztabar and Ranji, 2016; Zenkour, 2011; Zenkour and Fares, 1999);

$$\varepsilon_{xx} = \varepsilon_{xx}^{(0)} + z\varepsilon_{xx}^{(1)} + z^3\varepsilon_{xx}^{(3)},$$

$$\varepsilon_{yy} = \varepsilon_{yy}^{(0)} + z\varepsilon_{yy}^{(1)} + z^3\varepsilon_{yy}^{(3)},$$

$$\varepsilon_{xy} = \varepsilon_{xy}^{(0)} + z\varepsilon_{xy}^{(1)} + z^3\varepsilon_{xy}^{(3)},$$

$$\varepsilon_{yz} = \varepsilon_{yz}^{(0)} + z^2\varepsilon_{yz}^{(2)},$$

$$\varepsilon_{xz} = \varepsilon_{xz}^{(0)} + z^2\varepsilon_{xz}^{(2)}, \quad (3)$$

where

$$\varepsilon_{xx}^{(0)} = \frac{\partial u_0}{\partial x}, \quad \varepsilon_{yy}^{(0)} = \frac{\partial v_0}{\partial y}, \quad \varepsilon_{xy}^{(0)} = \frac{\partial u_0}{\partial y} + \frac{\partial v_0}{\partial x},$$

$$\varepsilon_{yz}^{(0)} = \beta\left(\varphi_y + \frac{\partial w}{\partial y}\right) + \gamma\frac{\partial w^s}{\partial y},$$

$$\varepsilon_{xz}^{(0)} = \beta\left(\varphi_x + \frac{\partial w}{\partial x}\right) + \gamma\frac{\partial w^s}{\partial x},$$

$$\varepsilon_{xx}^{(1)} = -\alpha\frac{\partial^2 w^b}{\partial x^2} + \beta\ \frac{\partial\varphi_x}{\partial x},$$

$$\varepsilon_{yy}^{(1)} = -\alpha\frac{\partial^2 w^b}{\partial y^2} + \beta\ \frac{\partial\varphi_y}{\partial y},$$

$$\varepsilon_{xy}^{(1)} = -2\alpha\frac{\partial^2 w^b}{\partial x\partial y} + \beta\left(\frac{\partial\varphi_x}{\partial y} + \frac{\partial\varphi_y}{\partial x}\right),$$

$$\varepsilon_{xz}^{(2)} = -\gamma\frac{4}{h^2}\frac{\partial w^s}{\partial x},$$

$$\varepsilon_{yz}^{(2)} = -\gamma\frac{4}{h^2}\frac{\partial w^s}{\partial y}, \ \varepsilon_{xx}^{(3)} = -\gamma\frac{4}{3h^2}\frac{\partial^2 w^s}{\partial x^2},$$

$$\varepsilon_{yy}^{(3)} = -\gamma\frac{4}{3h^2}\frac{\partial^2 w^s}{\partial y^2}, \ \varepsilon_{xy}^{(3)} = -2\gamma\frac{4}{3h^2}\frac{\partial^2 w^s}{\partial x\partial y}. \quad (4)$$

The material elastic properties of the non-homogeneous laminates can be expressed as;

$$E_{11}^{(k)}(z) = E_{01}^{(k)}\left[1 + \mu\, f^{(k)}(z)\right],$$

$$E_{22}^{(k)}(z) = E_{02}^{(k)}\left[1 + \mu\, f^{(k)}(z)\right],$$

$$G_{12}^{(k)}(z) = G_{012}^{(k)}\left[1 + \mu\, f^{(k)}(z)\right],$$

$$G_{13}^{(k)}(z) = G_{013}^{(k)}\left[1 + \mu\, f^{(k)}(z)\right],$$

$$G_{23}^{(k)}(z) = G_{023}^{(k)}\left[1 + \mu\, f^{(k)}(z)\right],$$

$$max\left|\mu f^{(k)}(z)\right| < 1 \ , \ (k = 1, 2, \ldots, N) \ , \ f^{(k)}(z) = z \ , \quad (5)$$

where $E_{01}^{(k)}$, $E_{02}^{(k)}$, $G_{012}^{(k)}$, $G_{013}^{(k)}$ and $G_{23}^{(k)}$ are the material elastic properties of homogeneous orthotropic laminates. N is total laminate number, μ is a parameter that represents the variation of elasticity modulus through the plate thickness (non-homogeneous coefficient) and $f^{(k)}(z)$ is the continuous functions which express the variation of the elastic properties (Mojahedin et al., 2016; Reddy et al., 2015; Schmitz and Horst, 2014; Sofiyev, 2016; Sofiyev and Kuruoglu, 2014; Sofiyev and Kuruoğlu, 2016; Sofiyev et al., 2008).

In the shear deformation theory (SDT), stress-strain expressions of kth non-homogeneous laminate can be given as (Gosling and Polit, 2014; Mojahedin et al., 2016; Reddy et al., 2015; Reddy, 2004; Thai and Choi, 2013a; Zenkour, 2011; Zhen and Lo, 2015);

$$\begin{Bmatrix}\sigma_{xx}\\ \sigma_{yy}\\ \sigma_{yz}\\ \sigma_{xz}\\ \sigma_{xy}\end{Bmatrix}^{(k)} = \begin{bmatrix}\overline{Q}_{11} & \overline{Q}_{12} & 0 & 0 & \overline{Q}_{16}\\ \overline{Q}_{12} & \overline{Q}_{22} & 0 & 0 & \overline{Q}_{26}\\ 0 & 0 & \overline{Q}_{44} & \overline{Q}_{45} & 0\\ 0 & 0 & \overline{Q}_{45} & \overline{Q}_{55} & 0\\ \overline{Q}_{16} & \overline{Q}_{26} & 0 & 0 & \overline{Q}_{66}\end{bmatrix}^{(k)} \begin{Bmatrix}\varepsilon_{xx}\\ \varepsilon_{yy}\\ \varepsilon_{yz}\\ \varepsilon_{xz}\\ \varepsilon_{xy}\end{Bmatrix}^{(k)}, \quad (6)$$

where $\bar{Q}_{ij}$ are the transformed material properties expressed as (Fares, 1999; Reddy, 2004; Thai and Choi, 2013b; Zenkour and Fares, 1999; Zerin et al., 2016);

$$\bar{Q}_{11} = Q_{11}\cos^4\theta + Q_{22}\sin^4\theta + 2(Q_{12} + 2Q_{66})\sin^2\theta\cos^2\theta ,$$

$$\bar{Q}_{12} = (Q_{11} + Q_{22} - 4Q_{66})\sin^2\theta cos^2\theta + Q_{12}(\sin^4\theta + \cos^4\theta),$$

$$\bar{Q}_{16} = (Q_{11} - Q_{12} - 2Q_{66})\sin\theta\cos^3\theta + (Q_{12} - Q_{22} + 2Q_{66})\sin^3\theta\cos\theta ,$$

$$\bar{Q}_{22} = Q_{11}\sin^4\theta + Q_{22}\cos^4\theta + 2(Q_{12} + 2Q_{66})\sin^2\theta\cos^2\theta \;\; ; \;\; \bar{Q}_{55} = Q_{44}\sin^2\theta + Q_{55}\cos^2\theta ,$$

$$\bar{Q}_{26} = (Q_{11} - Q_{12} - 2Q_{66})\cos\theta\sin^3\theta + (Q_{12} - Q_{22} + 2Q_{66})\cos^3\theta\sin\theta ,$$

$$\bar{Q}_{44} = Q_{44}\cos^2\theta + Q_{55}\sin^2\theta ,$$

$$\bar{Q}_{45} = (Q_{55} - Q_{44})\cos\theta\sin\theta ,$$

$$\bar{Q}_{55} = Q_{44}\sin^2\theta + Q_{55}\cos^2\theta ,$$

$$\bar{Q}_{66} = (Q_{11} + Q_{22} - 2Q_{12} - 2Q_{66})\sin^2\theta\cos^2\theta + Q_{66}(\sin^4\theta + \cos^4\theta) , \tag{7}$$

in which θ is the angle between global x-axis and local x-axis of each laminate. The material properties of the laminate $Q_{\mathrm{ij}}^{(k)}$ are given by;

$$Q_{11}^{(k)} = \frac{E_{01}^{(k)}[1+\mu f^{(k)}(z)]}{1-\nu_{12}^{(k)}\nu_{21}^{(k)}} \;\; , \;\; Q_{12}^{(k)} = \frac{\nu_{12}^{(k)}E_{02}^{(k)}[1+\mu f^{(k)}(z)]}{1-\nu_{12}^{(k)}\nu_{21}^{(k)}} \;\; , \;\; Q_{22}^{(k)} = \frac{E_{02}^{(k)}[1+\mu f^{(k)}(z)]}{1-\nu_{12}^{(k)}\nu_{21}^{(k)}} \;\; ,$$

$$Q_{66}^{(k)} = G_{012}^{(k)}[1+\mu f^{(k)}(z)] \;\; , \;\; Q_{44}^{(k)} = G_{023}^{(k)}[1+\mu f^{(k)}(z)] \;\; , \;\; Q_{55}^{(k)} = G_{013}^{(k)}[1+\mu f^{(k)}(z)] \;\; , \tag{8}$$

where $E_{01}^{(k)}$ and $E_{02}^{(k)}$ are modulus of elasticity of homogeneous case in 1 and 2 material-principal directions, respectively; $G_{012}^{(k)}$, $G_{013}^{(k)}$ and $G_{023}^{(k)}$ are shear modulus of homogeneous case in the 1-2, 1-3 and 2-3 surfaces, respectively and v_{ij} are Poisson's ratio.

3. Equations of Motion

To obtain the equation of motion, the principle of virtual work are written as;

$$0 = \int_A \left\{\int_{-h/2}^{h/2}\left[\sigma_{xx}^{(k)}\left(\delta\varepsilon_{xx}^{(0)} + z\delta\varepsilon_{xx}^{(1)} + z^3\delta\varepsilon_{xx}^{(3)}\right) + \sigma_{yy}^{(k)}\left(\delta\varepsilon_{yy}^{(0)} + z\delta\varepsilon_{yy}^{(1)} + z^3\delta\varepsilon_{yy}^{(3)}\right) + \cdots\right]dz\right\} dxdy - \int_A q\delta\,(w^b + w^s)dA , \tag{9}$$

or

$$0 = \int_A\left[N_{xx}\delta\varepsilon_{xx}^{(0)} + M_{xx}\delta\varepsilon_{xx}^{(1)} + P_{xx}\delta\varepsilon_{xx}^{(3)} + N_{yy}\delta\varepsilon_{yy}^{(0)} + M_{yy}\delta\varepsilon_{yy}^{(1)} + P_{yy}\delta\varepsilon_{yy}^{(3)} + N_{xy}\delta\varepsilon_{xy}^{(0)} + M_{xy}\delta\varepsilon_{xy}^{(1)} + P_{xy}\delta\varepsilon_{xy}^{(3)} + Q_x\delta\varepsilon_{xz}^{(0)} + R_x\delta\varepsilon_{xz}^{(2)} + Q_y\delta\varepsilon_{yz}^{(0)} + R_y\delta\varepsilon_{yz}^{(2)} - q\delta(w^b + w^s)\right] , \tag{10}$$

where N, M, Q are the stress resultants and P and R are the higher order stress resultants defined by;

$$\begin{Bmatrix} N_{\xi\eta} \\ M_{\xi\eta} \\ P_{\xi\eta} \end{Bmatrix} = \sum_{k=1}^{N}\int_{z_{k-1}}^{z_k}\sigma_{\xi\eta}^{(k)}\begin{Bmatrix} 1 \\ z \\ z^3 \end{Bmatrix}dz \quad , \quad \begin{Bmatrix} Q_\xi \\ R_\xi \end{Bmatrix} = \sum_{k=1}^{N}\int_{z_{k-1}}^{z_k}\sigma_{\xi z}^{(k)}\begin{Bmatrix} 1 \\ z^2 \end{Bmatrix}dz \; . \tag{11}$$

Note that ξ and η take the symbols x and y. Substituting Eq.(9) into Eq.(11) the stress resultants are obtained as (Phan and Reddy, 1985; Reddy, 1984; Reddy, 2004; Reissner, 1975; Thai and Choi, 2013a, 2013b; Yin et al., 2014);

$$\begin{Bmatrix} \{N_{\xi\eta}\} \\ \{M_{\xi\eta}\} \\ \{P_{\xi\eta}\} \end{Bmatrix} = \begin{bmatrix} [A] & [B] & [E] \\ [B] & [D] & [F] \\ [E] & [F] & [H] \end{bmatrix}\begin{Bmatrix} \{\varepsilon_{\xi\eta}^{(0)}\} \\ \{\varepsilon_{\xi\eta}^{(1)}\} \\ \{\varepsilon_{\xi\eta}^{(3)}\} \end{Bmatrix} \quad , \quad \begin{Bmatrix} \{Q_\xi\} \\ \{R_\xi\} \end{Bmatrix} = \begin{bmatrix} [A] & [D] \\ [D] & [F] \end{bmatrix}\begin{Bmatrix} \{\varepsilon_{\xi z}^{(0)}\} \\ \{\varepsilon_{\xi z}^{(2)}\} \end{Bmatrix} . \tag{12a}$$

where

$$\left(A_{ij}, B_{ij}, D_{ij}, E_{ij}, F_{ij}, H_{ij}\right) = \sum_{k=1}^{N}\int_{z_{k-1}}^{z_k}\bar{Q}_{ij}^{(k)}(1, z, z^2, z^3, z^4, z^6)\,dz \quad (i,j = 1,2,6) \; .$$

$$\left(A_{ij}, D_{ij}, F_{ij}\right) = \sum_{k=1}^{N}\int_{z_{k-1}}^{z_k}\bar{Q}_{ij}^{(k)}(1, z^2, z^4)\,dz \quad (i,j = 4,5) \; . \tag{12b}$$

4. Analytical Solution

The determination of transverse deflection and stresses are the fundamental process in the design of many constructional components. Non-homogeneous function and non-homogeneous coefficients are used to analyse the non-homogeneous laminated plate.

Boundary conditions of a simply supported rectangular plate are;

$$x = 0, a \quad , \; u = w = \varphi_x = 0 \; .$$

$$y = 0, b \quad , \; v = w = \varphi_y = 0 \; . \tag{13}$$

The considered transverse distribution load can be expanded in a double Fourier series

$$q(x,y) = \sum_{m=1,3,..}^{\infty} \sum_{n=1,3,..}^{\infty} Q_{mn} \sin\left(\frac{m\pi x}{a}\right) \sin\left(\frac{n\pi y}{b}\right), \tag{14}$$

and

$$Q_{mn} = \begin{cases} q_0 & \text{for sinusoidal load, } m = n = 1 \\ \frac{16q_0}{mn\pi^2} & \text{for uniform load, } m,n = 1,3,5,\ldots \end{cases}, \tag{15}$$

where q_0 represents the load at the center of the plate.

Navier approach is considered for the analytical solution of the problems. So, it can be assumed that;

$$\begin{Bmatrix} \beta w \\ \alpha w^b \\ \gamma w^s \\ \beta \varphi_x \\ \beta \varphi_y \end{Bmatrix} = \sum_{m=1}^{\infty} \sum_{n=1}^{\infty} \begin{Bmatrix} \beta \, W_{mn} \sin(\frac{m\pi x}{a}) \sin(\frac{n\pi y}{b}) \\ \alpha \, W_{mn}^b \sin(\frac{m\pi x}{a}) \sin(\frac{n\pi y}{b}) \\ \gamma \, W_{mn}^s \sin(\frac{m\pi x}{a}) \sin(\frac{n\pi y}{b}) \\ \beta \, X_{mn} \cos(\frac{m\pi x}{a}) \sin(\frac{n\pi y}{b}) \\ \beta \, Y_{mn} \sin(\frac{m\pi x}{a}) \cos(\frac{n\pi y}{b}) \end{Bmatrix}, \tag{16}$$

where $W_{mn}, X_{mn}, Y_{mn}, W_{mn}^b$ and W_{mn}^s are the arbitrary coefficients. Substituting Eqs. (4), (15a) and (16) into the Eq. (12) and substituting Eqs. (4), (12a) and (16) into the Eq. (9), we get for the bending problem;

$$[S]\{\Gamma_{mn}\} = \{F\} \, , \tag{17}$$

and for the buckling problem, we can get

$$([P] - [L])\{\Gamma_{mn}\} = \{0\} \, , \tag{18}$$

where

$$\{\Gamma_{mn}\} = \{\beta \, W_{mn} \quad \alpha \, W_{mn}^b \quad \gamma \, W_{mn}^s \quad \beta \, X_{mn} \quad \beta \, Y_{mn}\}^T \, , \tag{19}$$

is the solution vector. The elements of the coefficient matrices $[P]$, $[L]$ and $[S]$ are defined in Appendix A. For solution of Eq. (17), the following determinant should be zero and this equation gives the critical buckling loads;

$$|[P] - [L]| = 0 \, . \tag{20}$$

5. Numerical Results and Discussion

In this section, various numerical examples are analyzed and discussed to confirm the accuracy of the present study for bending and buckling analysis of non-homogeneous composite plates. For all problems a simply supported plate is considered for analysis. The transverse loading considered is sinusoidal for bending problems. Results of analysis are obtained in closed form using Navier's solution procedure for the above geometry and loading and the accuracy of the numerical results is confirmed by comparing results with their counterparts in the literature (Librescu and Khdeir, 1988; Noor, 1973; Pagano, 1970; Pagano and Hatfield, 1972; Putcha and Reddy, 1986; Reddy, 2004).

Note that Model-1, Model-2 and Model-3 represents the displacement fields of Zenkour and Fares (1999), simplified-higher order theory and first order theory, respectively, for bending analysis of plates. Displacement fields of simplified-higher order theory and first order theory is also considered for buckling analysis of the laminated plates. Also, shear correction factor is determined as $5/6$ for FSDT.

It is assumed that the thickness and the material are same for all laminates and the following sets of data and non-dimensionalizations are used to present results;

$Material\ 1\ (bending)$:

$$E_{01} = 25E_{02} \, , \;\; G_{012} = G_{013} = 0.5E_{02} \, ,$$

$$G_{023} = 0.2E_{02} \, , \;\; \nu_{12} = 0.25 \; .$$

$Material\ 2\ (buckling)$:

$$E_{01} = 40E_{02} \, , \;\; G_{012} = G_{013} = 0.6E_{02} \, ,$$

$$G_{023} = 0.5E_{02} \, , \;\; \nu_{12} = 0.25 \; . \tag{21}$$

and

$$\bar{w} = \frac{100h^3 E_{02}}{q_0 a^4} w\left(\frac{a}{2}, \frac{b}{2}\right) \, ,$$

$$\bar{\sigma}_x = \frac{h^2}{q_0 a^2} \sigma_x\left(\frac{a}{2}, \frac{b}{2}, \frac{h}{2}\right) \, ,$$

$$\bar{\sigma}_y = \frac{h^2}{q_0 a^2} \sigma_y\left(\frac{a}{2}, \frac{b}{2}, \frac{h}{4}\right) \, ,$$

$$\bar{\sigma}_{xy} = \frac{h^2}{q_0 a^2} \sigma_{xy}(0,0,-\frac{h}{2}) \, ,$$

$$\bar{\sigma}_{yz} = \frac{h}{q_0 a} \sigma_{yz}(\frac{a}{2}, 0,0) \, ,$$

$$\bar{\sigma}_{xz} = \frac{h}{q_0 a} \sigma_{xz}(0, \frac{b}{2}, 0) \, ,$$

$$\bar{N}_{cr} = \frac{N_{cr} a^2}{E_{02} h^3} \; . \tag{22}$$

5.1. Example 1

A simply supported four-layered symmetric cross-ply ($0^0/90^0/90^0/0^0$) non-homogeneous rectangular plate subjected to sinusoidal transverse load is considered. The layers have equal thickness. The numerical results of deflection and stresses are given in Table 1.

The results show that the values obtained from HSDT (present) and Zenkour and Fares (1999) present good agreement based on increasing of a/h ratios. For a/h ratio equal to 4, deflection of Model-1 by 18.63%, Model-2 by 24.78%, Model-3 by 13.42% compared to the results of elasticity solution. Fig. 8 shows the variation of transverse displacement versus a/h ratios. It demonstrates that the results obtained from Model-2 and Model-3 are in good agreement by increasing a/h ratios and shows that transverse displacement values decrease based on increase of non-homogeneous coefficients. The results show that Model-2 gives better accuracy in thin plates (a/h=100) compared to other models whereas Model-1 gives better accuracy in thick plates (a/h=4). The in-plane stress values of all models increase with the increasing a/h ratios. Fig. 9 shows the variation of transverse displacement versus a/b ratios for a/h ratio equal to 10. It shows that the transverse displacement values obtained by using Model-2 and Model-3 are in excellent agreement for a/b ratio equal to 2 and shows that transverse displacement values decrease with increasing of non-homogeneous coefficients. Fig. 10 shows the variation of $\bar{\sigma}_x$ through the thickness of symmetric cross-ply ($0^0/90^0/90^0/0^0$) square plate for a/h ratio equal to 4. Figs. 11 and 12 contain similar plots of $\bar{\sigma}_{xz}$ and $\bar{\sigma}_{yz}$ for a/b ratio of 1 and 3 and a/h ratio equal to 4. They show that the stress values obtained by using Model-2 and Model-3 decrease with the increasing of non-homogeneous coefficients.

Table 1. Non-dimensionalized deflections and stresses in four-layer cross-ply (0/90/90/0) square laminates under sinusoidal transverse loads.

a/h	Source	$\bar{w}$	$\bar{\sigma}_x$	$\bar{\sigma}_y$	$\bar{\sigma}_{xz}$	$\bar{\sigma}_{yz}$	$\bar{\sigma}_{xy}$
	Elasticity	1.9540	0.7200	0.6630	0.2910	0.2920	0.0467
	Zenkour	1.8937	0.6651	0.6322	0.2064	0.2389	0.0440
	$\mu = 0.01$	1.5899	0.6345	0.6033	0.1834	0.2106	0.0372
4	HSDT (present)	1.4858	0.7584	0.1116	0.3312	0.1325	0.0300
	$\mu = 0.01$	1.4698	0.7503	0.1110	0.3310	0.1324	0.0302
	FSDT (present)	1.7101	0.4064	0.5410	0.3495	0.0785	0.0308
	$\mu = 0.01$	1.6917	0.4020	0.5361	0.3493	0.0784	0.0311
	Elasticity	0.7430	0.5590	0.4010	0.3010	0.1960	0.0275
	Zenkour	0.7147	0.5456	0.3888	0.2640	0.1531	0.0268
	$\mu = 0.01$	0.6049	0.5242	0.3711	0.2339	0.1352	0.0228
10	HSDT (present)	0.6046	0.5752	0.1634	0.3395	0.1358	0.0227
	$\mu = 0.01$	0.5981	0.5690	0.1624	0.3393	0.1357	0.0229
	FSDT (present)	0.6632	0.4994	0.3647	0.4165	0.0517	0.0242
	$\mu = 0.01$	0.6560	0.4941	0.3614	0.4162	0.0516	0.0244
	Elasticity	0.5170	0.5430	0.3080	0.3280	0.1560	0.0230
	Zenkour	0.5060	0.5393	0.3043	0.2825	0.1234	0.0228
	$\mu = 0.01$	0.4310	0.5187	0.2918	0.2499	0.1096	0.0195
20	HSDT (present)	0.4751	0.5483	0.1710	0.3408	0.1363	0.0217
	$\mu = 0.01$	0.4700	0.5424	0.1700	0.3405	0.1362	0.0219
	FSDT (present)	0.4916	0.5279	0.3108	0.4370	0.0435	0.0221
	$\mu = 0.01$	0.4863	0.5222	0.3079	0.4366	0.0434	0.0223
	Elasticity	0.4385	0.5390	0.2760	0.3370	0.1410	0.0216
	Zenkour	0.4343	0.5387	0.2708	0.2897	0.1117	0.0213
	$\mu = 0.01$	0.3713	0.5187	0.2605	0.2561	0.0995	0.0183
100	HSDT (present)	0.4334	0.5396	0.1734	0.3412	0.1365	0.0213
	$\mu = 0.01$	0.4288	0.5338	0.1724	0.3409	0.1364	0.0215
	FSDT (present)	0.4341	0.5388	0.1741	0.4448	0.0403	0.0213
	$\mu = 0.01$	0.4295	0.5330	0.1731	0.4445	0.0403	0.0215

5.2. Example 2

A simply supported three-layered symmetric cross-ply ($0^0/90^0/0^0$) non-homogeneous rectangular plate subjected to sinusoidal transverse load is considered. The layers have equal thickness. The numerical results of transverse displacement and stresses for various side-to-thickness ratios (a/h) and aspect ratio of 3 are given in Table 2. The results show that the values obtained from HSDT (present) and Zenkour and Fares (1999) display good agreement with increasing of a/h ratios. It is understood from the results that, the deflection and stresses diminish by increasing the non-homogeneity coefficient. This results imply that the laminated composite plate become more rigid due to inclusion of non-homogeneous elastic properties. The results show that the error achieved by using the Model-3 is very large compared to other models and the error reduces with increasing of slenderness ratio (a/h). For a/h equal to 4, 10 and 20, Model-2 gives better result of in-plane stress $\bar{\sigma}_x$ whereas Model-3 gives more accurate results of in-plane shear stress than the other models for the above side-to-thickness ratios. For very thin non-homogeneous plates (a/h=100) Model-2 gives more accurate results of $\bar{\sigma}_x$ and in-plane shear stress than the other models. Fig. 2 shows the variation of transverse displacements of

non-homogeneous laminated square plate versus side-to-thickness ratio and Fig. 3 shows the variation of transverse displacement of non-homogeneous laminated plate with aspect ratio for a/h=10. It can be seen from these figures that the transverse displacement values decrease with increasing of a/h ratios and non-homogeneous coefficients for both Model-2 and Model-3, and these values increase with increasing of a/b ratios for both Model-2 and Model-3. The transverse displacement value obtained by using Model-2 and Model-3 are in excellent agreement for a/h ratio of 10. It is understood from Figs. 3, 5 and 7 that the effect of non-homogeneity is substantial for rectangular plates due to high aspect ratio, while it becomes less remarkable for symmetric and antisymmetric square plates. Fig. 4 shows that the discrepancy of in-plane stress $\bar{\sigma}_y$ between Model-2 and Model-3 diminish by increasing of a/h ratio and Fig. 5 shows that the variation of in-plane stress $\bar{\sigma}_y$ is minimum for aspect ratio of 3 for both Model-2 and Model-3. Figs. 6 and 7 shows that the discrepancy of in-plane shear stress between Model-2 and Model-3 diminish with increasing of a/h and a/b ratios for side-to-thickness ratio of 10.

Table 2. Non-dimensionalized deflections and stresses in rectangular (a=3b), three-layer cross-ply (0/90/0) laminates under sinusoidal transverse loads.

a/h	Source	$\bar{w}$	$\bar{\sigma}_x$	$\bar{\sigma}_y$	$\bar{\sigma}_{xz}$	$\bar{\sigma}_{yz}$	$\bar{\sigma}_{xy}$
	Elasticity	2.8200	1.1000	0.1190	0.3870	0.0334	0.0281
	Zenkour	2.6411	1.0356	0.1028	0.0348	0.2724	0.0263
	$\mu = 0.01$	2.2148	0.9884	0.0971	0.2414	0.0314	0.0221
4	HSDT (present)	3.1942	1.1541	0.0255	0.8522	0.1136	0.0154
	$\mu = 0.01$	3.1599	1.1417	0.0253	0.8515	0.1135	0.0155
	FSDT (present)	2.3631	0.6095	0.0054	0.4698	0.0123	0.0205
	$\mu = 0.01$	2.3378	0.6030	0.0054	0.4694	0.0123	0.0207
	Elasticity	0.9190	0.7250	0.0435	0.4200	0.0152	0.0123
	Zenkour	0.8622	0.6924	0.0398	0.0170	0.2859	0.0115
	$\mu = 0.01$	0.7309	0.6664	0.0380	0.2531	0.0155	0.0098
10	HSDT (present)	0.9560	0.7121	0.0392	0.8951	0.1193	0.0095
	$\mu = 0.01$	0.9458	0.7045	0.0389	0.8944	0.1192	0.0096
	FSDT (present)	0.8035	0.6204	0.0354	0.4735	0.0064	0.0105
	$\mu = 0.01$	0.7949	0.6138	0.0351	0.4731	0.0064	0.0106
	Elasticity	0.6100	0.6500	0.0299	0.4340	0.0119	0.0093
	Zenkour	0.5937	0.6407	0.0289	0.0139	0.2880	0.0091
	$\mu = 0.01$	0.5073	0.6180	0.0278	0.2529	0.0128	0.0078
20	HSDT (present)	0.6177	0.6453	0.0413	0.9016	0.1202	0.0086
	$\mu = 0.01$	0.6111	0.6384	0.0410	0.9008	0.1201	0.0087
	FSDT (present)	0.5789	0.6222	0.0403	0.4741	0.0054	0.0088
	$\mu = 0.01$	0.5727	0.6156	0.0400	0.4737	0.0054	0.0089
	Elasticity	0.5080	0.6240	0.0253	0.4390	0.0108	0.0083
	Zenkour	0.5077	0.6240	0.0253	0.2886	0.0129	0.0083
	$\mu = 0.01$	0.4350	0.6024	0.0244	0.2555	0.0119	0.0071
100	HSDT (present)	0.5085	0.6238	0.0420	0.9037	0.1205	0.0083
	$\mu = 0.01$	0.5030	0.6171	0.0417	0.9029	0.1204	0.0084
	FSDT (present)	0.5069	0.6228	0.0419	0.4743	0.0051	0.0083
	$\mu = 0.01$	0.5015	0.6162	0.0416	0.4739	0.0051	0.0084

5.3. Example 3

A simply supported three- and four-layered symmetric cross-ply non-homogeneous rectangular plate subjected to biaxial or uniaxial compressive load is considered. Tables 3 and 4 present the dimensionless critical buckling loads of cross-ply square plates for orthotropy ratios (E_1/E_2) and for various values of non-homogeneity coefficient μ. It can be seen that the present numerical results of critical buckling loads for the homogeneous (μ=0) plates obtained through the present HSDT are in good agreement with the corresponding results above. The discrepancy between critical buckling loads predicted by FSDT and HSDT increases with increase of non-homogeneity coefficients. The numerical results show that the critical buckling loads increase with increasing of the orthotropy ratio of individual layer and non-homogeneity coefficient. Furthermore, the number of layers has not a significant effect on critical buckling loads. Figs. 13 and 14 show that the results of critical buckling load obtained through the present theories are in good agreement for orthotropy ratio of 16, and Tables 3 and 4 confirm that HSDT gives more accurate results than FSDT compared to Three-dimensional elasticity solution and higher-order theory solution. Figs. 15-17 illustrate the variation of the dimensionless critical buckling loads versus the plate side-to-thickness ratio and the plate aspect ratio, respectively. It can be seen in corresponding figures that the non-homogeneity effect is more significant in thin (high side-to-thickness ratio) laminated plates with high aspect ratio. This means that the plate stability is strengthened with increasing these ratios. Figs. 18 and 19 display the variation of the dimensionless critical buckling loads vs. compressing ratio (k) for (0/90/0) and (0/90/90/0) square plates. These figures represent that the non-homogeneity effect on the stability process is weak for high ratios of (k) and a/h.

Table 3. Non-homogeneity effects on the biaxial critical buckling loads ($\bar{N}_{cr} = N_{cr}a^2/E_{02}h^3$) of (0/90/0) square plates (a/h=10, k=1).

E_1/E_2	Khdeir & Librescu	$\mu = 0.00$		$\mu = 0.02$		$\mu = 0.04$	
		FSDT	HSDT	FSDT	HSDT	FSDT	HSDT
2	2.3640	2.9279	2.3076	2.9913	2.3576	3.0548	2.4076
10	4.9630	5.4722	5.0925	5.5908	5.2028	5.7094	5.3131
20[a]	5.5160	7.9683	7.8343	8.1410	8.004	8.3136	8.1738
30[a]	9.0560	9.5439	9.4369	9.7507	9.6414	9.9574	9.8459
40[a]	10.2590	10.7091	10.8887	10.9411	11.1246	11.1732	11.3605

[a] The lowest critical buckling occurs at mode numbers m=1 , n=2, otherwise the critical buckling occurs at mode numbers m=1, n=1.

Table 4. The effect of the orthotropy on the uniaxial buckling load ($\bar{N}_{cr} = N_{cr}a^2/E_{02}h^3$) of cross-ply square plates (a/h=10, k=0).

Source	Lamination scheme	E_1/E_2				
		3	10	20	30	40
Putcha & Reddy	0/90/0	5.3933	9.9406	15.2980	19.6740	23.3400
Noor		5.3044	9.7621	15.0191	19.3040	22.8807
Zenkour		5.3899	9.8325	14.8896	18.8776	22.1207
$\mu = 0.05$		5.5635	10.0866	15.2113	19.2358	22.4985
HSDT (present)		5.3526	10.1849	16.2233	21.4351	25.9817
$\mu = 0.05$		5.6425	10.7366	17.1021	22.5962	27.389
FSDT (present)		6.5594	10.9445	15.9366	19.8796	23.0869
$\mu = 0.05$		6.9147	11.5373	16.7999	20.9564	24.3374
Reddy	0/90/90/0	5.1140	9.7770	15.2980	19.9570	23.3400
Noor		5.3040	9.7620	15.0190	19.3040	22.8810
HSDT (present)		5.3526	10.1849	16.2233	21.4351	25.9817
$\mu = 0.05$		5.6425	10.7366	17.1021	22.5962	27.389
FSDT (present)		6.5612	11.0325	16.2911	20.5926	24.2037
$\mu = 0.05$		6.9166	11.6301	17.1736	21.708	25.5147

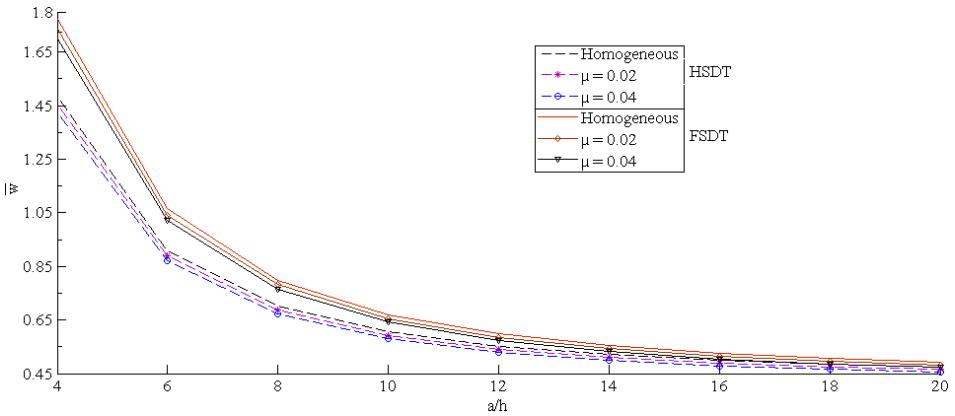

Fig. 2. Non-dimensional center deflection ($\bar{w}$) versus side-to-thickness ratio of a (0/90/0) square plate under sinusoidal load for various values of μ.

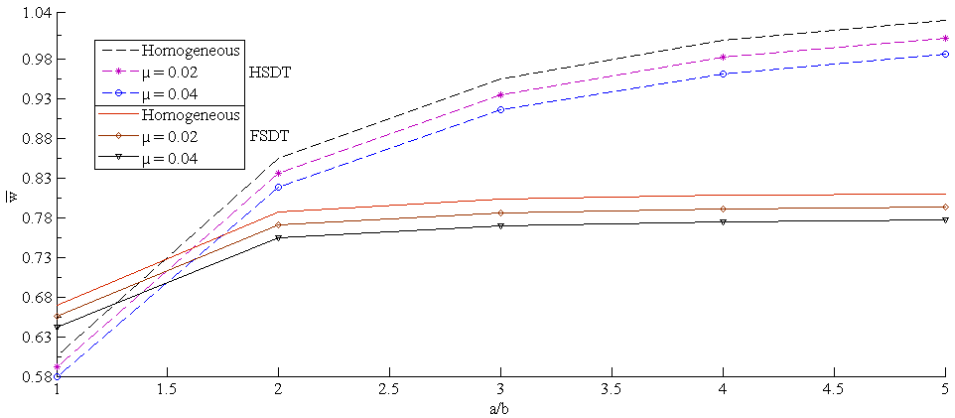

Fig. 3. Effect of the aspect ratio on the center deflection ($\bar{w}$) of a (0/90/0) plate under sinusoidal load for various values of μ ($a/h = 10$).

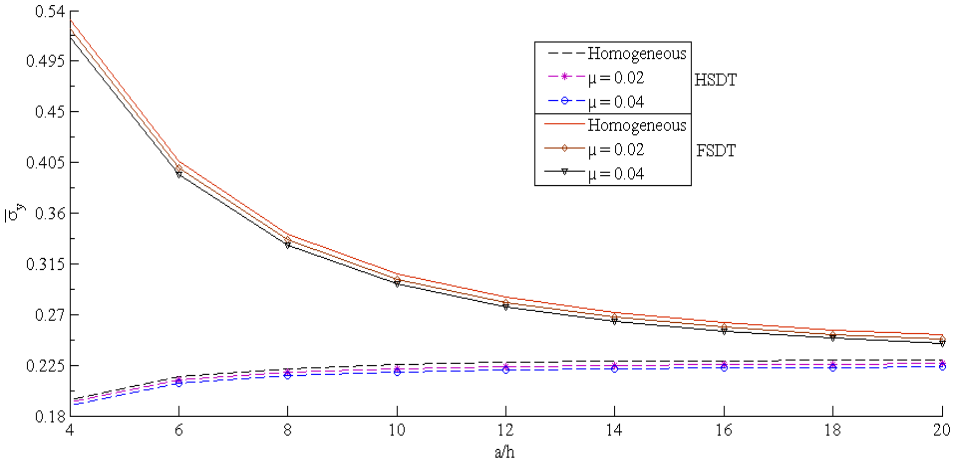

Fig. 4. Non-dimensional normal stress ($\bar{\sigma}_y$) versus side-to-thickness ratio of a (0/90/0) plate under sinusoidal load for various values of μ.

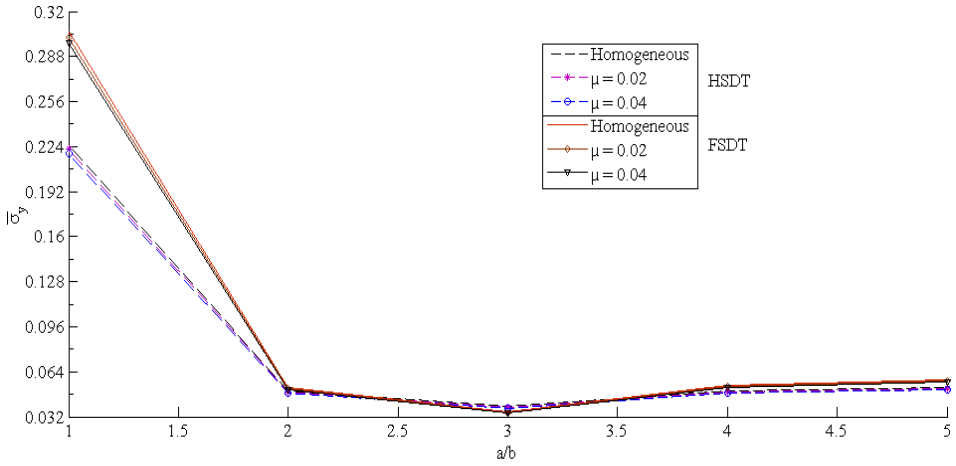

Fig. 5. Effect of the aspect ratio on the normal stress ($\bar{\sigma}_y$) of a (0/90/0) plate under sinusoidal load for various values of μ ($a/h = 10$).

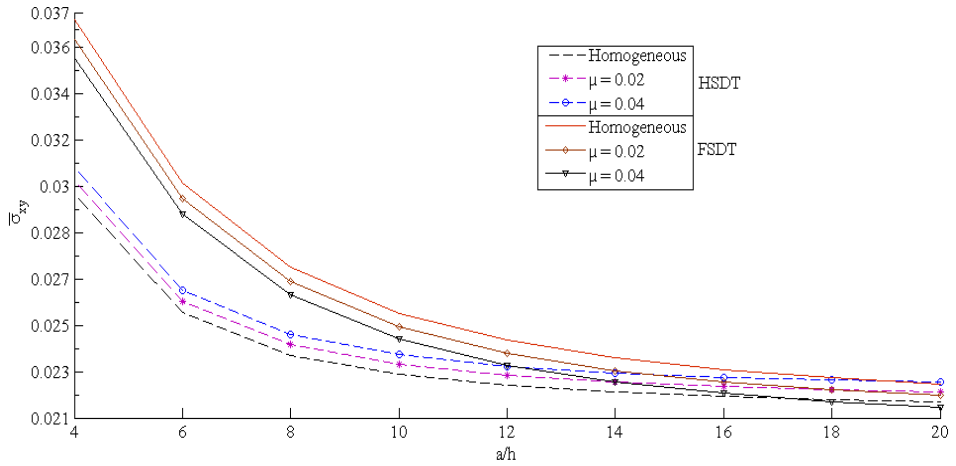

Fig. 6. Non-dimensional tangential stress ($\bar{\sigma}_{xy}$) versus side-to-thickness ratio of a (0/90/0) square plate under sinusoidal load for various values of μ.

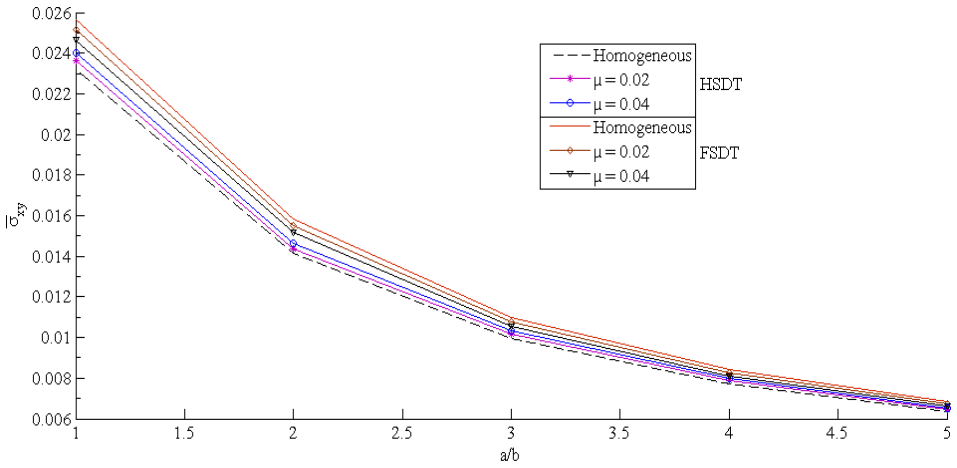

Fig. 7. Effect of the aspect ratio on the tangential stress ($\bar{\sigma}_{xy}$) of a (0/90/0) plate under sinusoidal load for various values of μ ($a/h = 10$).

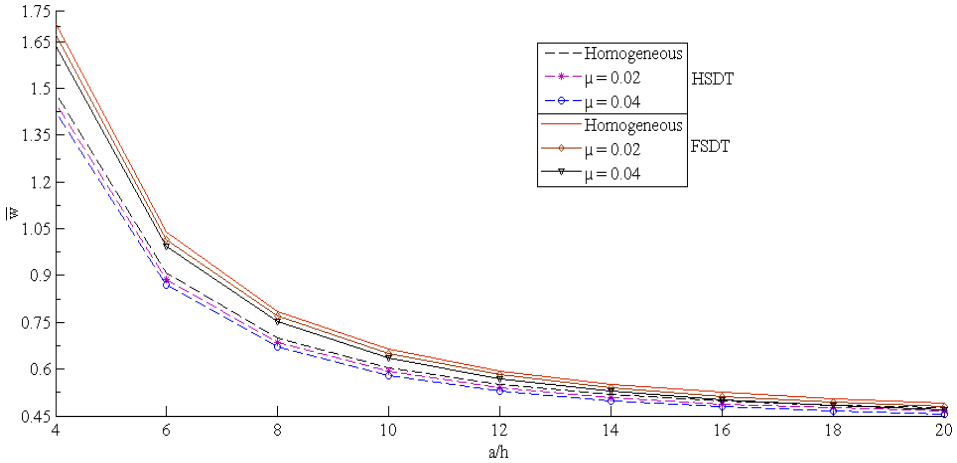

Fig. 8. Non-dimensional center deflection ($\bar{w}$) versus side-to-thickness ratio of a (0/90/90/0) square plate under sinusoidal load for various values of μ.

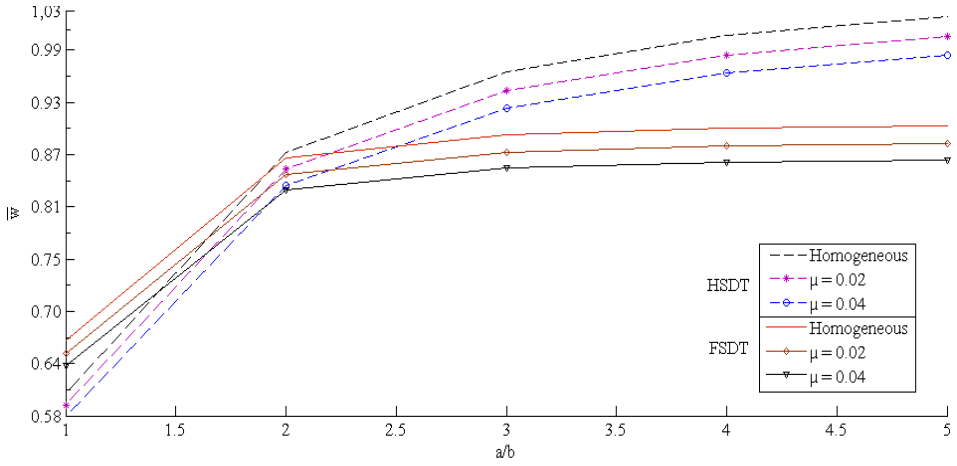

Fig. 9. Effect of the aspect ratio on the center deflection ($\bar{w}$) of a (0/90/90/0) plate under sinusoidal load for various values of μ ($a/h = 10$).

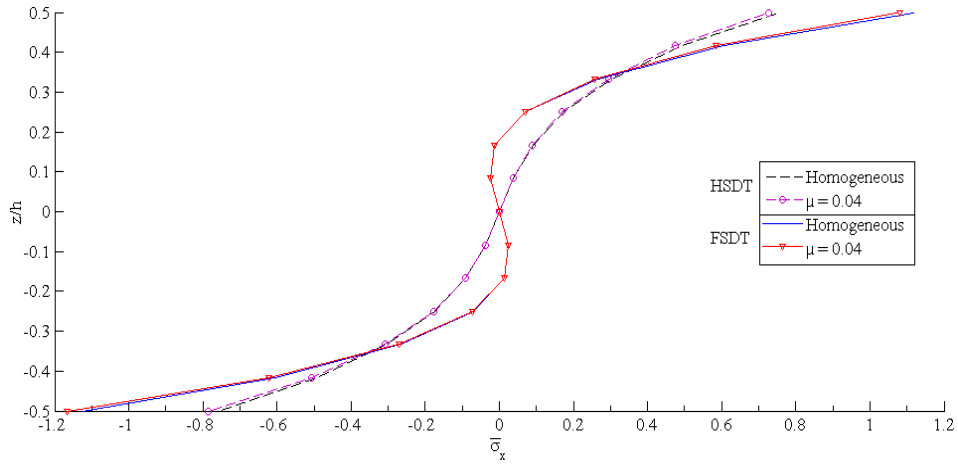

Fig. 10. Variation of non-dimensional normal stress ($\bar{\sigma}_x$) through the laminate thickness of a (0/90/90/0) square plate under sinusoidal load for various values of μ ($a/h = 4$).

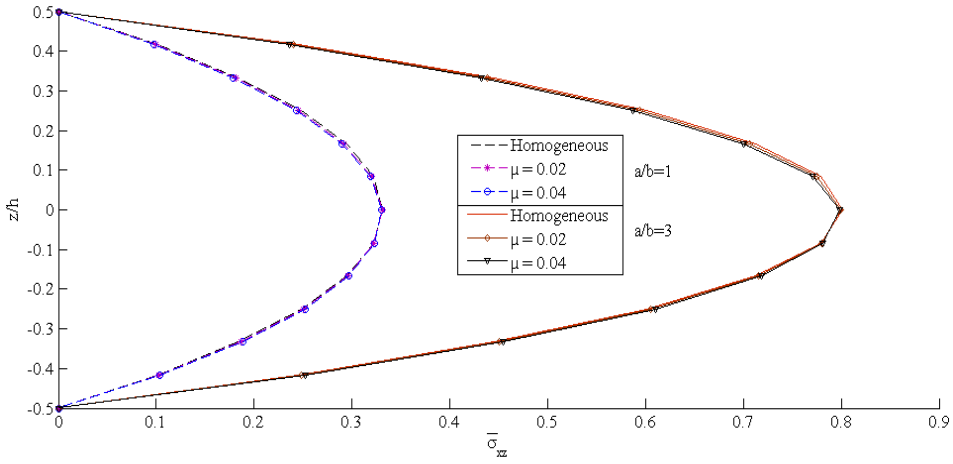

Fig. 11. Variation of non-dimensional normal stress ($\bar{\sigma}_{xz}$) through the laminate thickness of a (0/90/90/0) square plate under sinusoidal load for various values of μ ($a/h = 4$).

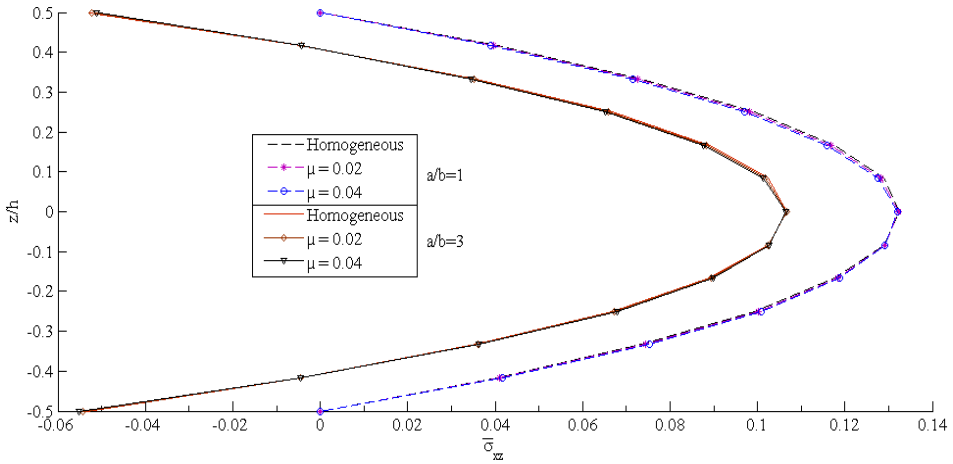

Fig. 12. Variation of non-dimensional normal stress ($\bar{\sigma}_{yz}$) through the laminate thickness of a (0/90/90/0) square plate under sinusoidal load for various values of μ ($a/h = 4$).

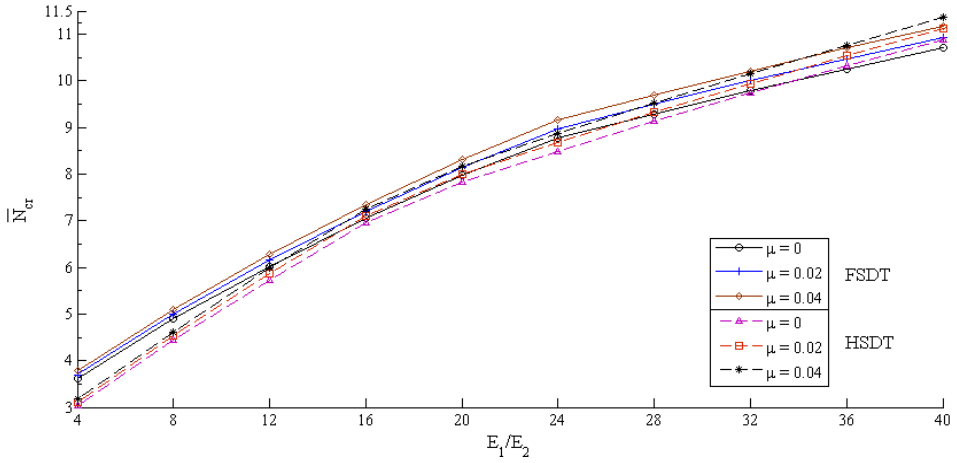

Fig. 13. Effect of the orthotropy ratio on the biaxial critical buckling load of a (0/90/0) square plate for various values of μ $(a/h = 10,\ k = 1)$.

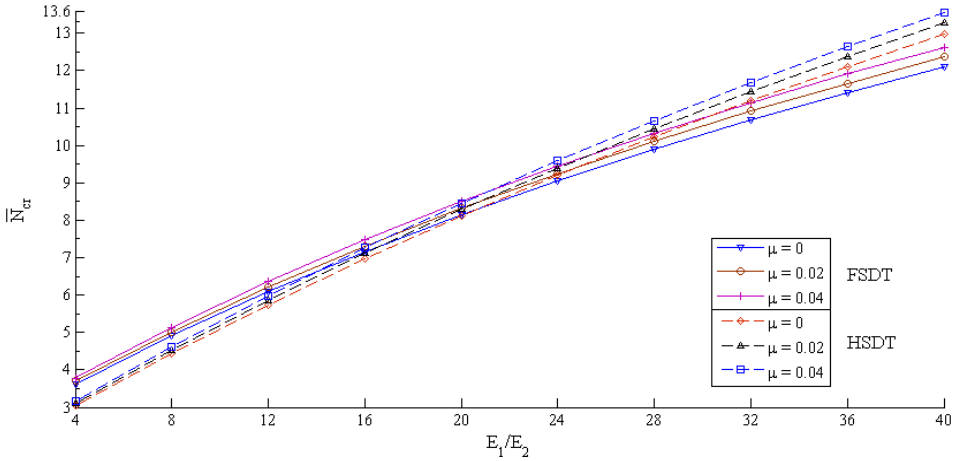

Fig. 14. Effect of the orthotropy ratio on the biaxial critical buckling load of a (0/90/90/0) square plate for various values of μ $(a/h = 10,\ k = 1)$.

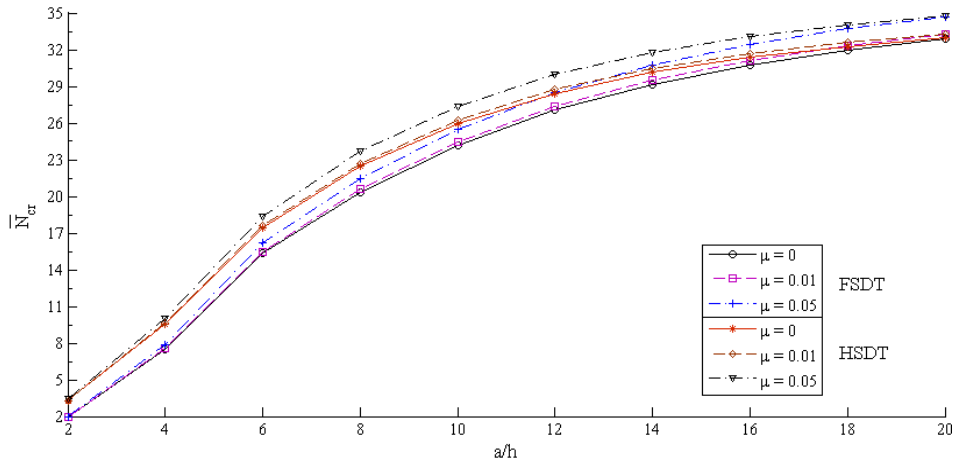

Fig. 15. Effect of the side-to-thickness ratio on the axial critical buckling load of a (0/90/90/0) square plate for various values of μ $(a/h = 10,\ k = 0)$.

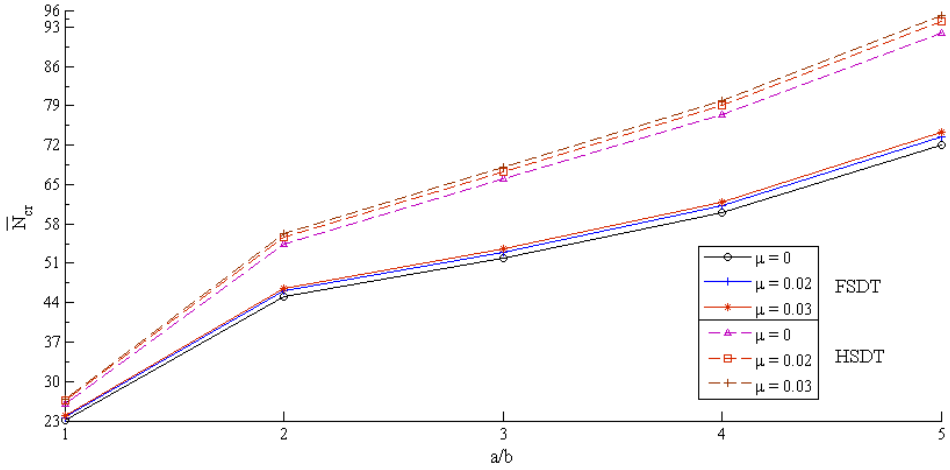

Fig. 16. Effect of the aspect ratio on the axial critical buckling load of a (0/90/0) plate for various values of μ $(a/h = 10,\ k = 0)$.

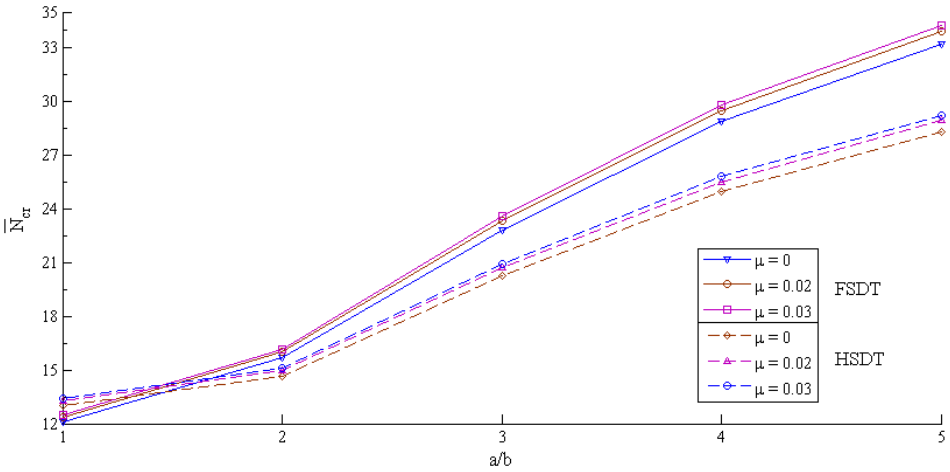

Fig. 17. Effect of the aspect ratio on the axial critical buckling load of a (0/90/90/0) plate for various values of μ $(a/h = 10,\ k = 1)$.

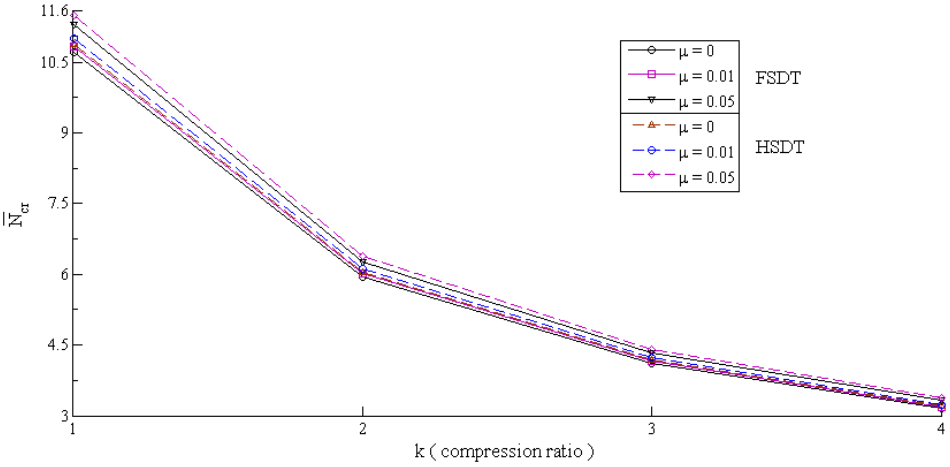

Fig. 18. Effect of the k (compression ratio) on the critical buckling load of a (0/90/0) square plate for various values of μ $(a/h = 10)$.

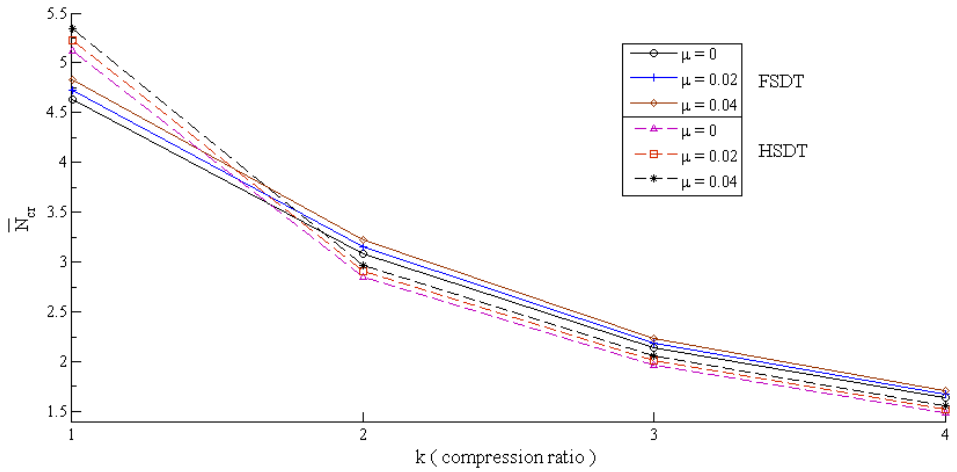

Fig. 19. Effect of the k (compression ratio) on the critical buckling load of a $(0/90/90/0)$ square plate for various values of μ $(a/h = 4)$.

6. Conclusions

Analytical solutions for the bending analysis of simply supported laminated non-homogeneous composite plates based on first and simplified-higher order theory are presented. The displacement field of simplified-higher order theory assumes that the in-plane rotation tensor is constant through the thickness. For thin and very thin non-homogeneous laminated plates the solution of the simplified-higher order theory (Model-2) is found a good agreement with the elasticity solution and percentage error with respect to elasticity solution is much less compared to other shear deformation theories used for comparison in this study. For thick non-homogeneous laminated plates the results of Model-1 is in good agreement with the elasticity solution. The main aim of this study is to reveal the accuracy of the various shear deformation theory for bending analysis of non-homogeneous laminated plates.

The buckling problems of non-homogeneous rectangular plates are investigated. Numerical results for the critical buckling loads of symmetric cross-ply laminates are predicted by both of first- and higher-order theories. The effects of non-homogeneity, aspect ratio, side-to-thickness ratio, compressing ratio and in-plane orthotropy ratio on critical buckling loads are illustrated. The numerical results are compared with corresponding results similar studies. The study concludes that the present first- and higher-order theories predict reasonable accuracy the buckling response of non-homogeneous plates. Furthermore, the non-homogeneity, aspect ratio and in-plane orthotropy ratio have a significant effect on the stability process and buckling response of laminates.

Appendix A.

The elements $S_{ij} = S_{ji}$ of the coefficient matrix $[S]$:

$$S_{11} = K(A_{55}\lambda^2\beta^2 + A_{44}\mu^2\beta^2) \quad , \quad S_{12} = 0 \quad , \quad S_{13} = K(A_{55}\lambda^2\beta\gamma + A_{44}\mu^2\beta\gamma) - c_2\,(D_{55}\lambda^2\beta\gamma + D_{44}\mu^2\beta\gamma) \ ,$$

$$S_{14} = K\lambda\beta^2 A_{55} \quad , \quad S_{15} = K\mu\beta^2 A_{44} \quad , \quad S_{22} = \lambda^4\alpha^2 D_{11} + 2\lambda^2\mu^2\alpha^2(D_{12} + 2D_{66}) + \mu^4\alpha^2 D_{22} \ ,$$

$$S_{23} = c_1\lambda^4\alpha\gamma F_{11} + 2c_1\lambda^2\mu^2\alpha\gamma(F_{12} + 2F_{66}) + c_1\mu^4\alpha\gamma F_{22} \quad , \quad S_{24} = -\lambda^3\alpha\beta D_{11} - \lambda\mu^2\alpha\beta(D_{12} + 2D_{66}) \ ,$$

$$S_{25} = -\lambda^2\mu\alpha\beta(D_{12} + 2D_{66}) - \mu^3\alpha\beta D_{22} \ ,$$

$$S_{33} = c_1^2\lambda^4\gamma^2 H_{11} + 2c_1^2\lambda^2\mu^2\gamma^2(H_{12} + 2H_{66}) + c_1^2\mu^4\gamma^2 H_{22} + c_2^2(\lambda^2\gamma^2 F_{55} + \mu^2\gamma^2 F_{44}) - 2c_2(\lambda^2\gamma^2 D_{55} + \mu^2\gamma^2 D_{44}) + \lambda^2\gamma^2 A_{55} + \mu^2\gamma^2 A_{44} \ ,$$

$$S_{34} = -c_1(\lambda^3\beta\gamma F_{11} + \lambda\mu^2\beta\gamma(F_{12} + 2F_{66}) - c_2\lambda\beta\gamma D_{55} + K\lambda\beta\gamma A_{55} \ ,$$

$$S_{35} = -c_1(\lambda^2\mu\beta\gamma(F_{12} + 2F_{66}) + \mu^3\beta\gamma F_{22}) - c_2\mu\beta\gamma D_{44} + K\mu\beta\gamma A_{44} \ ,$$

$$S_{44} = \lambda^2\beta^2 D_{11} + \mu^2\beta^2 D_{66} + K\beta^2 A_{55} \ ,$$

$$S_{45} = \lambda\mu\beta^2(D_{12} + D_{66}), S_{55} = \mu^2\beta^2 D_{22} + \lambda^2\beta^2 D_{66} + K\beta^2 A_{44} \ ,$$

and the elements $P_{ij} = P_{ji}$ of the coefficient matrix $[P]$:

$$P_{11} = S_{11} + L_{11} \quad , \quad P_{12} = S_{12} + L_{12} \quad , \quad P_{13} = S_{13} + L_{13} \quad , \quad P_{14} = S_{14} \quad , \quad P_{15} = S_{15}, P_{22} = S_{22} + L_{22},$$

$$P_{23} = S_{23} + L_{23} \quad , \quad P_{24} = S_{24} \quad , \quad P_{25} = S_{25} \quad , \quad P_{33} = S_{33} + L_{33} \quad , \quad P_{34} = S_{34} \quad , \quad P_{35} = S_{35} \quad , \quad P_{44} = S_{44},$$

$$P_{45} = S_{45} \quad , \quad P_{55} = S_{55} \ .$$

where

$$L_{11} = N_0\lambda^2\beta^2 + kN_0\mu^2\beta^2 \quad , \quad L_{12} = N_0\lambda^2\alpha\beta + kN_0\mu^2\alpha\beta \quad , \quad L_{13} = N_0\lambda^2\beta\gamma + kN_0\mu^2\beta\gamma \ ,$$

$$L_{22} = N_0\lambda^2\alpha^2 + kN_0\mu^2\alpha^2 \quad , \quad L_{23} = N_0\lambda^2\alpha\gamma + kN_0\mu^2\alpha\gamma \quad , \quad L_{33} = N_0\lambda^2\gamma^2 + kN_0\mu^2\gamma^2 \ ,$$

$$\lambda = \frac{m\pi x}{a} \quad , \quad \mu = \frac{n\pi y}{b} \quad , \quad c_1 = \frac{4}{3h^2} \quad , \quad c_2 = -\frac{4}{h^2} \ ,$$

and K is shear correction factor and it is determined as $5/6$ for FSDT.

REFERENCES

Beena K, Parvathy U (2014). Linear static analysis of functionally graded plate using spline finite strip method. *Composite Structures,* 117, 309-315.

Fares M (1999). Non-linear bending analysis of composite laminated plates using a refined first-order theory. *Composite Structures,* 46(3), 257-266.

Fares M, Zenkour A (1999). Buckling and free vibration of non-homogeneous composite cross-ply laminated plates with various plate theories. *Composite Structures,* 44(4), 279-287.

Gosling P, Polit O (2014). A high-fidelity first-order reliability analysis for shear deformable laminated composite plates. *Composite Structures, 115*, 12-28.

Gupta A, Johri T, Vats R (2007). Thermal effect on vibration of non-homogeneous orthotropic rectangular plate having bi-directional parabolically varying thickness. *Proceeding of International Conference in World Congress on Engineering and Computer Science*.

Gupta U, Lal R, Sharma S (2006). Vibration analysis of non-homogeneous circular plate of nonlinear thickness variation by differential quadrature method. *Journal of Sound and Vibration,* 298(4), 892-906.

He WM, Chen WQ, Qiao H (2013). In-plane vibration of rectangular plates with periodic inhomogeneity: Natural frequencies and their adjustment. *Composite Structures,* 105, 134-140.

Kim S-E, Thai H-T, Lee J (2009). A two variable refined plate theory for laminated composite plates. *Composite Structures,* 89(2), 197-205.

Kolpakov A (1999). Variational principles for stiffnesses of a non-homogeneous plate. *Journal of the Mechanics and Physics of Solids,* 47(10), 2075-2092.

Komur MA, Sonmez M (2015). Elastic buckling behavior of rectangular plates with holes subjected to partial edge loading. *Journal of Constructional Steel Research,* 112, 54-60.

Kulkarni K, Singh B, Maiti D (2015). Analytical solution for bending and buckling analysis of functionally graded plates using inverse trigonometric shear deformation theory. *Composite Structures,* 134, 147-157.

Lal R (2007). Transverse vibrations of non-homogeneous orthotropic rectangular plates of variable thickness: A spline technique. *Journal of Sound and Vibration,* 306(1), 203-214.

Leknitskii SG, Fern P (1963). Theory of elasticity of an anisotropic elastic body. Holden-Day.

Librescu L, Khdeir A (1988). Analysis of symmetric cross-ply laminated elastic plates using a higher-order theory: Part I—Stress and displacement. *Composite Structures,* 9(3), 189-213.

Mojahedin A, Jabbari M, Khorshidvand A, Eslami M (2016). Buckling analysis of functionally graded circular plates made of saturated porous materials based on higher order shear deformation theory. *Thin-Walled Structures,* 99, 83-90.

Neves A, Ferreira A (2016). Free vibrations and buckling analysis of laminated plates by oscillatory radial basis functions. *Curved and Layered Structures, 3*(1), 17-21.

Noor AK (1973). Free vibrations of multilayered composite plates. *AIAA Journal,* 11(7), 1038-1039.

Pagano N (1970). Exact solutions for rectangular bidirectional composites and sandwich plates. *Journal of Composite Materials, 4*(1), 20-34.

Pagano N, Hatfield HJ (1972). Elastic behavior of multilayered bidirectional composites. *AIAA Journal,* 10(7), 931-933.

Papkov S, Banerjee J (2015). A new method for free vibration and buckling analysis of rectangular orthotropic plates. *Journal of Sound and Vibration,* 339, 342-358.

Patel SN (2014). Nonlinear bending analysis of laminated composite stiffened plates. *Steel and Composite Structures,* 17(6), 867-890.

Phan N, Reddy J (1985). Analysis of laminated composite plates using a higher-order shear deformation theory. *International Journal for Numerical Methods in Engineering,* 21(12), 2201-2219.

Putcha N, Reddy J (1986). Stability and natural vibration analysis of laminated plates by using a mixed element based on a refined plate theory. *Journal of Sound and Vibration,* 104(2), 285-300.

Reddy BS, Kumar JS, Reddy C, Reddy KVK (2015). Buckling analysis of functionally graded plates using higher order shear deformation theory with thickness stretching effect. *International Journal of Applied Science and Engineering* 13 (1*)*, 19-36.

Reddy JN (1984). A simple higher-order theory for laminated composite plates. *Journal of Applied Mechanics,* 51(4), 745-752.

Reddy JN (2004). Mechanics of laminated composite plates and shells: theory and analysis. CRC press.

Reissner E (1975). On transverse bending of plates, including the effect of transverse shear deformation. *International Journal of Solids and Structures,* 11(5), 569-573.

Sadoune M, Tounsi A, Houari MSA, Bedia ELAA (2014). A novel first-order shear deformation theory for laminated composite plates. *Steel and Composite Structures,* 17(3), 321-338.

Saheb KM, Aruna K (2015). Buckling analysis of moderately thick rectangular plates using coupled displacement field method. Journal of Physics: Conference Series.

Schmitz A, Horst P (2014). A finite element unit-cell method for homogenised mechanical properties of heterogeneous plates. *Composites Part A: Applied Science and Manufacturing,* 61, 23-32.

Senthilnathan N, Lim S, Lee K, Chow S (1988). Vibration of laminated orthotropic plates using a simplified higher-order deformation theory. *Composite Structures,* 10(3), 211-229.

Shahbaztabar A, Ranji AR (2016). Effects of in-plane loads on free vibration of symmetrically cross-ply laminated plates resting on Pasternak foundation and coupled with fluid. *Ocean Engineering,* 115, 196-209.

Sofiyev A (2016). Buckling of heterogeneous orthotropic composite conical shells under external pressures within the shear deformation theory. *Composites Part B: Engineering,* 84, 175-187.

Sofiyev A, Kuruoglu N (2014). Combined influences of shear deformation, rotary inertia and heterogeneity on the frequencies of cross-ply laminated orthotropic cylindrical shells. *Composites Part B: Engineering,* 66, 500-510.

Sofiyev A, Kuruoğlu N (2016). The stability of FGM truncated conical shells under combined axial and external mechanical loads in the framework of the shear deformation theory. *Composites Part B: Engineering,* 92, 463-476.

Sofiyev A, Zerin Z, Korkmaz A (2008). The stability of a thin three-layered composite truncated conical shell containing an FGM layer subjected to non-uniform lateral pressure. *Composite Structures,* 85(2), 105-115.

Sreehari V, Maiti D (2015). Buckling and post buckling analysis of laminated composite plates in hygrothermal environment using an Inverse Hyperbolic Shear Deformation Theory. *Composite Structures,* 129, 250-255.

Stürzenbecher R, Hofstetter K (2011). Bending of cross-ply laminated composites: An accurate and efficient plate theory based upon models of Lekhnitskii and Ren. *Composite Structures,* 93(3), 1078-1088.

Thai HT, Choi DH (2013a). A simple first-order shear deformation theory for laminated composite plates. *Composite Structures,* 106, 754-763.

Thai HT, Choi DH (2013b). A simple first-order shear deformation theory for the bending and free vibration analysis of functionally graded plates. *Composite Structures,* 101, 332-340.

Vescovini R, Dozio L (2016). A variable-kinematic model for variable stiffness plates: Vibration and buckling analysis. *Composite Structures,* 142, 15-26.

Yin S, Hale JS, Yu T, Bui TQ, Bordas SP (2014). Isogeometric locking-free plate element: a simple first order shear deformation theory for functionally graded plates. *Composite Structures,* 118, 121-138.

Yu T, Bui TQ, Yin S, Doan DH, Wu C, Van Do T, Tanaka S (2016). On the thermal buckling analysis of functionally graded plates with internal defects using extended isogeometric analysis. *Composite Structures,* 136, 684-695.

Zenkour A (2011). Bending responses of an exponentially graded simply-supported elastic/viscoelastic/elastic sandwich plate. *Acta Mechanica Solida Sinica,* 24(3), 250-261.

Zenkour A, Fares M (1999). Non-homogeneous response of cross-ply laminated elastic plates using a higher-order theory. *Composite Structures,* 44(4), 297-305.

Zenkour AM, Allam M, Mashat D (2007). Linear bending analysis of inhomogeneous variable-thickness orthotropic plates under various boundary conditions. *International Journal of Computational Methods,* 4(03), 417-438.

Zerin Z, Turan F, Basoglu MF (2016). Examination of non-homogeneity and lamination scheme effects on deflections and stresses of laminated composite plates. *Structural Engineering and Mechanics,* 57(4), 603-616.

Zhen W, Lo S (2015). Hygrothermomechanical effects on laminated composite plates in terms of a higher-order global-local model. *Journal of Thermal Stresses,* 38(5), 543-568.

Challenge Journal of Structural Mechanics

Research on relation between natural frequency and axial stress of round bar with intermediate-supported ends

Tsutomu Yoshida *, Takeshi Watanabe, Kunihiko Sakurada

Department of Mechanical Systems Engineering, Takushoku University, Bunkyo-ku, Tokyo 112-8585, Japan

ABSTRACT

In order to make a method be useful to measure an axial stress of a member by a natural frequency, we investigated a relation between a natural frequency and an axial stress of a round bar with intermediate-supported ends, the boundary condition of which was one between a fix-supported end and a simply-supported end. To define an intermediate-supported end condition, we adopted a parameter, a ratio of a moment of a force to a deflection angle at the end. It was shown theoretically that the parameter of an intermediate-supported end could be evaluated by one at a support on a continuous beam consisted of 3 spans. The 3-spanned beam has same vibration characteristics of a beam with intermediate-supported ends. We manufactured a test device of a 3-spanned beam by which we could simulate a vibration under various intermediate-supported end conditions. The theoretical relation and experimental results between a natural frequency and an axial stress agreed for the most part.

ARTICLE INFO

Article history:
Received 18 November 2016
Accepted 24 February 2017

Keywords:
Natural frequency
Axial stress
Intermediate support
Three-spanned beam

1. Introduction

From a view point of energy-saving, economic merits and environmental friendliness, development of health assessment methods for an existing structure or a machine is one of urgent problems. Fair evaluation of their integrity enables us to use them extending over an established design life.

Strain gauges have been used to measure strains in a structure or a machine. The method is simple and reliable. New kinds of strain gauges like a semiconductor or a piezoelectric element have been developed. Fiber Bragg Grating sensor was employed for health monitoring for a structure or a composite material (Moreira et al., 2012). In order to apply the method to a structure or a machine, we need many gauges. The measurement by strain gauges takes a lot of labour and accompanies troublesome works, and is unsuitable to measure working stress over a long period.

On the one hand, methods to measure strain at one point have been developed, on the other hand, methods to estimate strain distribution in an area have been developed. They are a digital image correlation method (Leplay et al., 2011) or an acoustic-elastic method (Kudryavtsev, 2008). These methods need to compare a picture or a property before and after the deformation of a structure or a specimen. The procedure is still complicated and is not easily employed on site.

Bars or rods play an important role in current structures as shown in Fig. 1. Being fabricated into a structure, they are expected to cooperate to suspend heavy burden. In order to arrange stresses in bars or rods within allowable level during construction or in operation, it is necessary to be able to measure their axial stress easily, reliably and promptly.

We have investigated a relation between a natural frequency and an axial stress of a round bar with fix-supported ends or with simply-supported ends. Theoretical relations and experimental results agreed (Yoshida et al., 2010). The agreement enabled us to measure an axial stress of a bar under these ends by a natural frequency. But, when we measured an axial stress of bars in an experimental truss device (Yoshida et al., 2013), experimental results agreed neither with a theoretical relation under fixed ends nor with one under simply-supported ends. The truss bar vibrated under the ends between

* *Corresponding author*. Tel.: +81-42-665-8449 ; Fax: +81-42-665-1519 ; E-mail address: t-yosida@ms.takushoku-u.ac.jp (T. Yoshida)
ISSN: 2149-8024 / DOI: https://doi.org/10.20528/cjsmec.2017.02.002

simply-supported ends and fix-supported ends. This is not only true of the experimental truss bar, but also of any member in existing structures or machines.

Fig. 1. Current structure.

In this research, a relation between a natural frequency and an axial stress was investigated for the beam with the ends between fixed supported ends and simply-supported ends. We refer such the end as an intermediate-supported end. To characterize the end condition, we adopted a parameter, a ratio of a moment of a force to a deflection angle at the end. To assess an intermediate-supported end condition, we employed a continuous beam consisted of 3 spans. Employing the 3-spanned beam, we compared theoretical relations and experimental results between a natural frequency and an axial stress under various intermediate-supported end conditions.

2. Theory and Numerical Calculation

2.1. Single beam with intermediate-supported ends

To explain a boundary condition of an intermediate-supported end, we illustrated a beam with the ends in Fig. 2 (Jinbo and Furukawa, 1971). The beam is supported by rigid sharp edges and is able to incline at the end. The beam extends into a resilient material. If the material were hard, the vibration of the beam would be one with fix-supported ends. If the material were soft, the vibration would be one with simply-supported ends. An intermediate hardness of a resilient material makes the beam vibrate with ends between simply-supported ends and fix-supported ends.

Boundary conditions at the ends are given by the following expressions.

$$(w)_{x=0} = 0\,,\quad (w)_{x=L} = 0\,, \tag{1}$$

$$-EI\left(\frac{\partial^2 w}{\partial x^2}\right)_{x=0} = k\left(\frac{\partial w}{\partial x}\right)_{x=0}\,,$$

$$-EI\left(\frac{\partial^2 w}{\partial x^2}\right)_{x=L} = -k\left(\frac{\partial w}{\partial x}\right)_{x=L}\,. \tag{2}$$

Here, w is a deflection of a beam and EI is a flexural rigidity. k is the ratio between a moment of a force and a deflection angle at the end. We refer k as a resilient parameter and a beam with intermediate-supported ends as an intermediate beam.

If k were zero, the moment of a force at the end, the left hand side of the Eqs. (2), should be zero. Then the boundary condition of the end corresponds to that of a simply-supported end. If k were quite large and there occurred a finite quantity of moment of a force at the end, the deflection angle of the beam at the end should be small. The boundary condition corresponds to that of a fix-supported end. The value of k between zero and quite a large value defines a boundary condition of an intermediate-supported end.

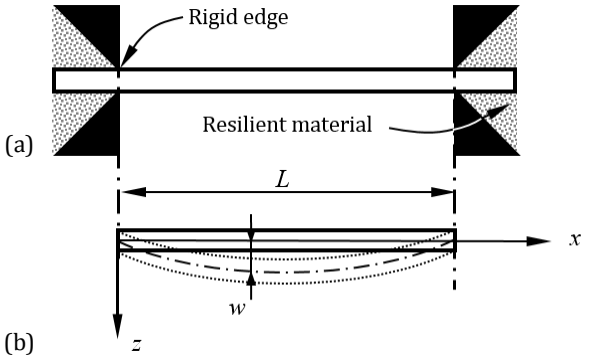

Fig. 2. Intermediate-supported ends: (a) Concrete instance; (b) Coordinate and deflection.

Following a conventional procedure to obtain a natural frequency of a beam, the frequency equation of the beam with intermediate-supported ends is given by the next formulae in the form of a determinant. The conventional procedure to obtain a natural frequency is explained in detail elsewhere (Timoshenko, 1954). Here ω is an angular frequency, ρ is a density and A is a sectional area.

$$\begin{vmatrix} 1 & 0 & 1 & 0 \\ \lambda & \Lambda & -\lambda & \Lambda \\ \cos(\chi) & \sin(\chi) & \cosh(\chi) & \sinh(\chi) \\ \lambda\cos(\chi) + \Lambda\sin(\chi) & \lambda\sin(\chi) - \Lambda\cos(\chi) & -\lambda\cosh(\chi) - \Lambda\sinh(\chi) & -\lambda\sinh(\chi) - \Lambda\cosh(\chi) \end{vmatrix} = 0\,, \tag{3}$$

where $\Lambda = k/EI$, $\chi = \lambda \cdot L$, $\lambda^2 = \omega/\eta$ and $\eta^2 = EI/\rho A$.

2.2. Three-spanned beam

To illustrate an intermediate-supported end, we assumed a resilient material. But, it is difficult to find out such material and achieve the end practically. We took up a continuous beam shown in Fig. 3(a). The beam is fixed at both ends and is simply-supported at two inner supports. The beam consists of 3 members: side members and a center member. A natural frequency of the beam varies depending on the length of the side members. We refer the beam as a 3-spanned beam. We show later that the 3-spanned beam has same vibration characteristics with an intermediate beam.

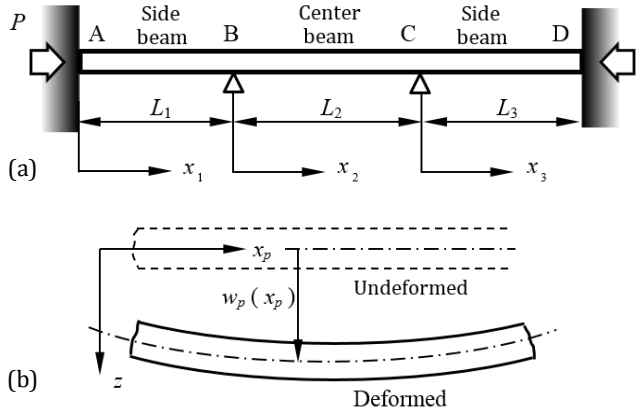

Fig. 3. Three-spanned beam with axial load: (a) Coordinate; (b) Deflection.

In order to investigate the relation between a natural frequency and an axial stress of the beam, we analysed the beam applying an axial load. A differential equation of a motion of each member of a 3-spanned beam applied with an axial load, P is given by the following equation for a transverse vibration of a uniform section and density.

$$\frac{\partial^2 w_p}{\partial t^2} + \frac{EI}{\rho A}\frac{\partial^4 w_p}{\partial x_p^4} + \frac{P}{\rho A}\frac{\partial^2 w_p}{\partial x_p^2} = 0\,. \tag{4}$$

A subscript, p (p=1,2,3) was employed to distinguish each member of the beam. Here, x_p and t are coordinate and time variables respectively. w_p is a deflection of each beam shown in Fig. 3(b). A solution of Eq. (4) was assumed to be given by the following form as the product of a modal shape function and time variation.

$$w_p(x_p, t) = W_p(x_p)\cdot e^{j\omega t}\,, \tag{5}$$

where j is an imaginary unit.

The mode shape may be written by the next form,

$$W_p(x_p) = C_{p1}\cdot\cos(\lambda_1 x_p) + C_{p2}\cdot\sin(\lambda_1 x_p) + C_{p3}\cdot\cosh(\lambda_2 x_p) + C_{p4}\cdot\sinh(\lambda_2 x_p)\,, \tag{6}$$

where,

$$\lambda_1 = \sqrt{\frac{\sqrt{\pi^4\cdot\beta^2+4\omega^2/\eta^2}+\pi^2\cdot\beta}{2}},$$

$$\lambda_2 = \sqrt{\frac{\sqrt{\pi^4\cdot\beta^2+4\omega^2/\eta^2}-\pi^2\cdot\beta}{2}} \quad \text{and} \quad \beta = \frac{P}{EI\pi^2}\,. \tag{7}$$

Twelve boundary conditions are provided for a 3-spanned beam. For example, the deflection at the left ends of each member is zero, which is expressed by Eq. (8a). The angle of a deflection or the moment of a force on either side of inner supports are to be same. The conditions are given by Eq. (8b).

$$W_p(0) = 0\,, \tag{8a}$$

$$W_p'(L_p) = W_{p+1}'(0)\,,\ W_p''(L_p) = W_{p+1}''(0)\,,\ p = 1,2 \tag{8b}$$

Applying these boundary conditions to Eq. (6), the following simultaneous equation, unknown variables of which are C_{pk} (k=1,2,3,4), is obtained. Here $\{C_{pk}\}$ stands for a row vector with 12 elements and **[K]** is a 12x12 matrix of coefficients of the simultaneous equation.

$$[\mathbf{K}]\{C_{pk}\} = \{\mathbf{0}\}\,. \tag{9}$$

The eigenvalue problem, Eq. (9), has a nontrivial solution only if the determinant of the matrix **K** vanishes.

$$|\mathbf{K}| = 0\,. \tag{10}$$

Eq. (10) gives the frequency equation of a 3-spanned beam.

A resilient parameter at the support, B in Fig. 3(a) is given by the following expression according to the definition.

$$k = \frac{M}{\theta} = -\frac{EI\cdot W_2''(0)}{W_2'(0)} = EI\cdot\frac{C_{21}\cdot(\lambda_1^2+\lambda_2^2)}{\lambda_1\cdot C_{22}+\lambda_2\cdot C_{24}}\,. \tag{11}$$

2.3. Numerical result

We used, in common, an 8 mm diameter round bar and material properties of a steel, such as E=206 GPa and ρ=7.89 g/cm^3 through this research. A simple analysis teaches that a round bar made out of a steel with 8 mm diameter and 200 mm span length vibrates with 401.3 Hz under simply-supported ends and with 909.7 Hz under fix-supported ends as shown in Table 1.

Table 1. Parameters of various ends.

Supported ends	f [Hz]	k [N·mm]	Ls [mm]
Simply-supported ends	401.3	$<10^6$	250
Intermediate-supported ends	↕	↕	↕
Fix-supported ends	909.7	$>10^{12}$	0

2.3.1. Relation between resilient parameter and natural frequency of intermediate beam

Employing Eq. (3), we calculated a relation between a resilient parameter and a natural frequency of the beam with intermediate-supported ends shown in Fig. 2. The beam taken up for the calculation is a round bar with steel properties, 8 mm diameter and 200 mm span length. Fig. 4(a) shows the result. A horizontal axis is a resilient parameter, k by a logarithmic scale and a vertical axis is a natural frequency.

When k becomes smaller than 10^6, the beam vibrates with the natural frequency, 401.3 Hz. The figure is same with that of the natural frequency under simply-supported ends in Table 1. When k becomes larger than 10^{12}, the beam vibrates with the natural frequency, 909.6 Hz. The figure is almost same with the natural frequency under fix-supported ends in Table 1. When the beam is supported by the ends with a resilient parameter between 10^6 and 10^{12}, the beam vibrates with a natural frequency between 401.3 to 909.6 Hz. The vibration is neither one under simply-supported ends nor one under fix-supported ends, but one under intermediate-supported ends. We can define an intermediate-supported end condition by its corresponding resilient parameter as shown in Table 1. A resilient parameter defines a condition of an end from a simply-supported end to a fix-supported end.

2.3.2. Relation between side span length and natural frequency of 3-spanned beam

Employing Eq. (10), we calculated a relation between a length of the side members and the first mode natural frequency of the 3-spanned beam with no axial stress and showed it by the solid line in Fig. 4(b). The beam taken up for the calculation is a round bar with steel properties, 8 mm diameter and, a length of a center member was set to be 200 mm. A horizontal axis is a length of the side members and a vertical axis is a natural frequency.

When the length of the side members approaches to 250 mm, a natural frequency of the beam approaches to 401.3 Hz. The figure is same with that of the natural frequency under simply-supported ends in Table 1. The length approaches to zero, the natural frequency approaches to 909.7 Hz. The figure is same with the above natural frequency under fix-supported ends. When the length of the side members is one between 0 and 250 mm, the beam vibrates with its corresponding natural frequency between 401.3 and 909.7 Hz as shown in Table 1. The 3-spanned beam has the same natural frequency range of an intermediate beam.

2.3.3. Equivalence of supported end on intermediate beam and 3-spanned beam

The natural frequency range as well as the vertical axis length of Figs. 4(a, b) were adjusted to be same. Fig. 4(a) refers to an intermediate beam and Fig. 4(b) to a 3-spanned beam. The material and the diameter of the two beams are same. The span length of the intermediate beam in Fig. 4(a) and the length of the center member of the 3-spanned beam in Fig. 4(b) are same 200 mm. Following the arrows extending over Fig. 4(a) to Fig. 4(b), we can correlate a resilient parameter to the side member length as like k_x to L_{sx} through the common natural frequency f_x. The reverse is also true. The arrows are connecting the vibration characteristics of the two beams.

In the calculation of the 3-spanned beam, we evaluated a resilient parameter, k at the support B in Fig. 4(b) defined by Eq. (11). Onto Fig. 4(a), we put the obtained values by square marks. Resilient parameters at the support on a 3-spanned beam agreed with those at the end on an intermediate beam theoretically. Equivalence of an intermediate-supported end on two beams was demonstrated.

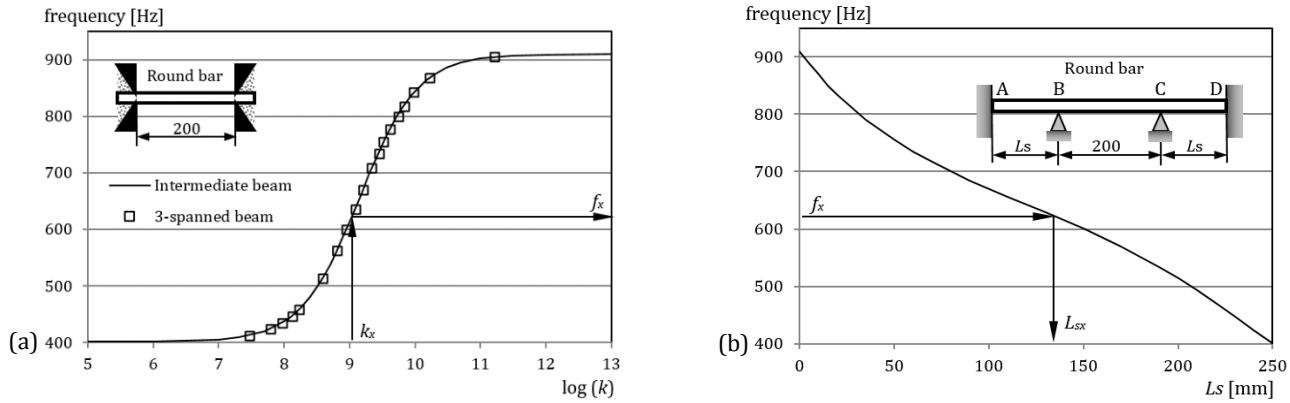

Fig. 4. Relation between resilient parameter, length of side members and natural frequency: (a) Intermediate beam; (b) 3-spanned beam.

3. Experiment

3.1. Experimental device

We manufactured a test device of a 3-spanned beam shown in Fig. 5. A round bar with 8 mm diameter made out of a steel was used as a specimen. Both ends of the specimen were fixed. Two inner supports, the condition of which was that of a simply-supported end, were placed between the fixed ends. The supports make the specimen be partitioned into side members and a center member. The length of the center member between

the inner supports was set to be 200 mm. The length of both side members, *Ls* is alterable to be 25, 75, 125, 175 and 252.2 mm. Frequencies of the specimen vibration vary according to the length, *Ls*. An axial stress can be loaded to the specimen by rotating a nut at its end. After an axial stress was loaded, setups for fix-supported ends and inner supports were made by clamping their bolts.

Fig. 5 also shows the measurement system. The system consists of a microphone, an amplifier, a filter, a fast fourie transformation (FFT) analyser and the 3-spanned beam device. In the experiment, striking the center member by a wooden bar, we generated a sound. Measuring the sound by a microphone, we analysed the sound through the FFT analyser and obtained natural frequencies of the 3-spanned beam.

3.2. Relation between axial stress and natural frequency under intermediate-supported ends

Theoretical relations and experimental results between an axial stress and a natural frequency under intermediate-supported end conditions were compared. The results are shown in Fig. 6. Horizontal axis is an axial stress. Vertical axis is a natural frequency. Lines show the theoretical relations obtained by Eq. (10). The experiment was conducted by the device shown in Fig. 5. Experimental data were shown by symbols.

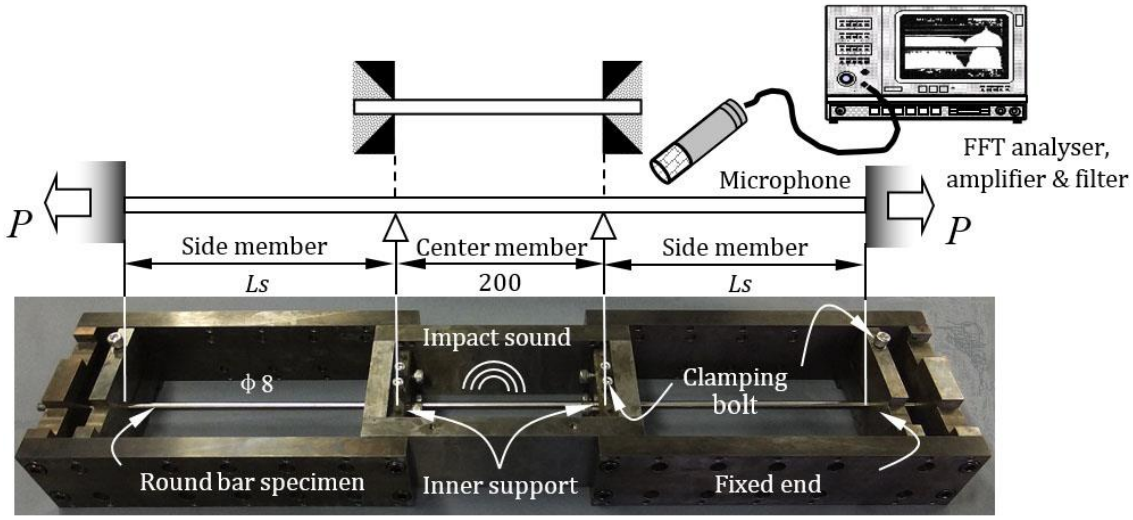

Fig. 5. Experimental device of 3-spanned beam with measurement system.

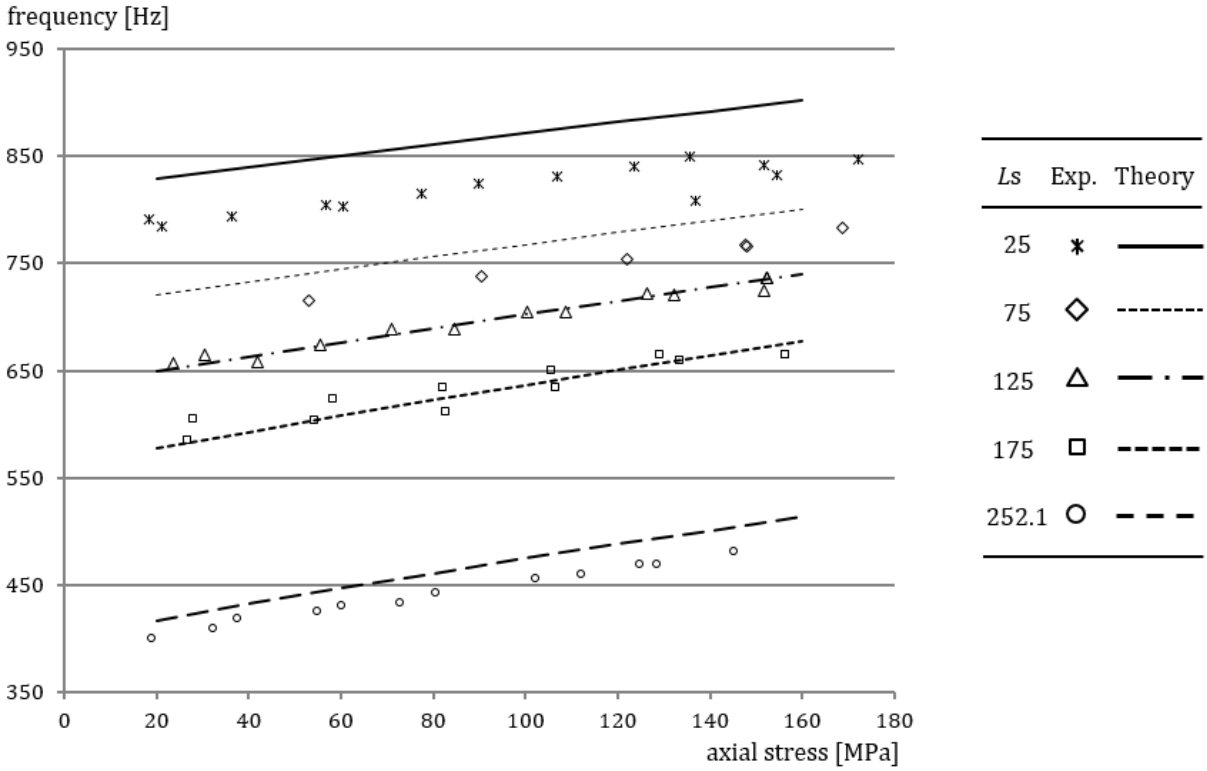

Fig. 6. Relation between axial stress and natural frequency for various side lengths.

The theoretical relations and experimental data agreed except one for Ls=20. Higher machining accuracy is needed for the experiment with shorter Ls. The accordance between the theory and the experiment enables us to estimate an axial stress by a natural frequency under intermediate-supported ends.

Ls is related to k as explained in the previous section. A practical application of the method to measure an axial stress of a beam with intermediate-supported ends by a natural frequency demands to evaluate a resilient parameter value at the end of the beam experimentally. We are now trying to evaluate a resilient parameter at the simply-supported end of the 3-spanned beam measuring deflections and strains. We left the development for the evaluation as future work.

4. Conclusions

A beam used in a structure or a machine is supported neither by a simply-supported end nor by a fix-supported end, but one between them. The support condition has a great influence on a natural frequency of the beam. We have been developing a method to measure an axial stress of a beam by its natural frequency. It is necessary to make it clear the relation between a natural frequency and a support-end condition. To define a support-end condition, we adopted a parameter, a ratio between a moment of a force and a deflection angle at an end.

- We developed a theory of a continuous beam with three spans and a beam with intermediate-supported ends.
- It was shown theoretically that an intermediate-supported end condition could be simulated by one at a support on a three-spanned beam.
- Applying an axial stress to a three-spanned beam, a relation between natural frequencies and axial stresses was investigated under various intermediate-supported end conditions experimentally and theoretically. They agreed for the most part. It implies that we can measure an axial stress by a natural frequency under intermediated-supported ends.

We left as future work an experimental procedure to measure a parameter value which would define an intermediate-supported end condition.

References

Jinbo Y, Furukawa E (1971). Exercise of Vibration Engineering. Gakukensha. 126-128 (in Japanese).

Kudryavsev YF, Residual Stress (2008). Springer Handbook on Experimental Solid Mechanics. Springer -SEM. 371-387.

Leplay P, Rethore J, Meille J, Baietto MC (2011). Identification of damage and cracking behaviors based on energy dissipation mode analysis in a quasi-brittle material using digital image correlation. *International Journal of Fracture*, 171(1), 35-50.

Moreira PMGP, Lucas FM, Silva, Loureiro ALD (2012). Determination of the strain distribution in adhesive joints using fiber gragg grating sensors. *Proceedings of the 15th International Conference on Experimental Mechanics*, Porto, Portugal, 581-582.

Timoshenko SP (1954). Vibration Problems in Engineering. D.Van Nostrad Company Inc., Toronto, Canada.

Yoshida T, Sakurada K, Hoshino M (2010). Development on measurement technology of axial load in truss structure member by impact sound. *Proceedings of the 14th International Conference on Experimental Mechanics*, Poitier, France.

Yoshida T, Ismail MZB, Watanabe T (2013). Measurement of static stress in round bar by impact sound. *Proceedings of the 4th International Conference on Integrity, Reliability & Failure*, Funchal, Portugal, 63-64.

Challenge Journal of Structural Mechanics

Metaheuristic approaches for optimum design of cantilever reinforced concrete retaining walls

Gebrail Bekdaş *, Rasim Temür

Department of Civil Engineering, İstanbul University, 34320 İstanbul, Turkey

ABSTRACT

An approach is presented for optimum design of cantilever reinforced concrete (RC) retaining wall via teaching-learning based optimization (TLBO) algorithm. The objective function of the optimization is to minimize total material cost including concrete and reinforcing steel bars of the cantilever retaining wall by considering overturning, sliding and bearing stabilities, bending moment and shear capacities and requirements for design and construction of reinforced concrete structures (TS 500/2000). TLBO algorithm is a simple algorithm without any special algorithm parameters. This innovative approach is providing an advantage to TLBO in terms of easily applying to the problem. The proposed method has been performed on numerical examples and the results are compared with previous approaches. Results show that, the methodology is feasible for obtaining the optimum design of RC cantilever retaining walls.

ARTICLE INFO

Article history:
Received 29 September 2016
Accepted 18 November 2016

Keywords:
Optimization
Teaching-learning based optimization
Cantilever
Reinforced concrete
Retaining wall

1. Introduction

The design process of the reinforced concrete (RC) structures involves some decisions, i.e. dimensions of the structural members, material properties (compressive strength of concrete, yield strength of steel), diameter and spacing of bars, etc. done by designer. The security and total cost of the design are closely related with these decisions. Thus, the experience of the designer has an important role in the economy and structural safety. But, it may not enough to find the best design in mean of total cost considering the whole design process of the RC structures containing many design variables and using two materials with extremely different mechanical behavior and unit material cost. For that reason, it must be used or developed methods that are independent of the user experiences in order to ensure best (or optimum) design.

Until recently, the optimum design methods are developed for frames (Balling and Yao, 1997; Guerra and Kiousis, 2006), beams (Barros et al., 2005; Barros et al., 2012; Ferreira et al., 2003), pre-stressed concrete bridges (Sirca and Adeli, 2005), columns (Gil-Martin et al., 2010) and slabs (Ahmadkhanlou and Adeli, 2005).

Despite having successfully applied under specific conditions, the mathematical methods may not present a general methodology for engineering design problems due to the complex (or nonlinear) relationship between design variables. For example, geometry dimension and shape of the cross section of the structural member effects internal forces, displacements and amount (size and spacing) of the bars. Thus, it is not easy to determine whole this relationship with a suitable formulation in order to apply a conventional method and to find optimum results. For that reason, the metaheuristic algorithms are widely used for optimum design of such problems. In the documented methods, the most popular algorithms in the optimum design of RC member are genetic algorithm (Coello et al., 1997; Govindaraj and Ramasamy, 2005; Fedghouche and Tiliouine, 2012; Rafiq and Southcombe, 1998; Rajeev and Krishnamoorthy, 1998; Camp et al., 2003; Lee and Ahn, 2003; Govindaraj and Ramasamy, 2007) and simulated annealing (Paya et al., 2008; Paya-Zaforteza et al., 2009; Ceranic et al., 2001; Yepes et al., 2008; Perea et al., 2008; Rama Mohan Rao and Shyju, 2010). In these studies, several structural members including beams, columns, frames, bridges and plates are handled as design problems.

* *Corresponding author*. Tel.: +90-212-4737070 ; Fax: +90-212-4737180 ; E-mail address: bekdas@istanbul.edu.tr (G. Bekdaş)
ISSN: 2149-8024 / DOI: https://doi.org/10.20528/cjsmec.2016.11.031

In addition to these algorithms, particle swarm optimization (Ahmadi-Nedushan and Varaee, 2009) big bang big crunch algorithm (Camp and Akin, 2012; Camp and Huq, 2013; Kaveh and Sabzi, 2012), harmony search algorithm (Kaveh and Abadi, 2011; Akin and Saka, 2010; Akin and Saka, 2012; Bekdaş and Nigdeli, 2012; 2014; Nigdeli et al., 2015), bat algorithm (Bekdaş and Nigdeli, 2016) and teaching-learning based optimization algorithm (Temür and Bekdaş, 2016) are also employed for optimum design of RC members.

In this paper, a methodology employing teaching-learning based optimization developed by Rao et al. (2011) is presented for optimum design of cantilever retaining RC walls. Turkish Standard Requirements for design and construction of reinforced concrete structures (TS500/2000) regulation are considered in RC design. In order to see the efficiency of the proposed method, the analyses results are compared with the state-of-art algorithms like particle swarm optimization (PSO) and big bang big crunch (BB-BC).

2. Methodology

In 2011, Rao et al. proposed a metaheuristic algorithm called teaching-learning based optimization (TLBO) from the inspiration of teaching and learning process in a classroom. Compared with other metaheuristics, one of the innovative parts of the TLBO algorithm is to not use specific algorithm parameters. The optimization process of TLBO algorithm can be summarized in four steps.

Step I: In the first step, population number (*pn*), ranges of the design variables and stopping criterion (maximum iteration number) are defined.

Step II: Then, the initial solution matrix is constructed by using *pn* number of the solution vectors. Each solution vector contains *vn* number of randomly generated design variables (X_i) which are shown in Fig. 1 and Table 1.

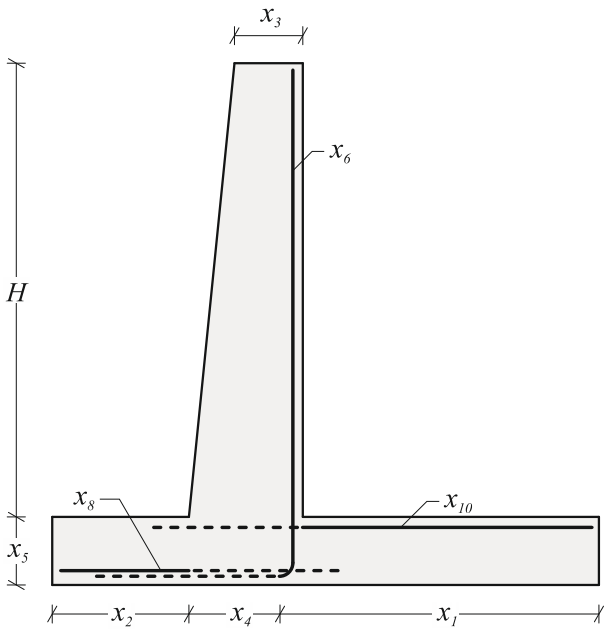

Fig. 1. Design variables for cantilever retaining wall.

Table 1. Design variables.

	Description	Design variable
Variables related to Cross-section dimension	Heel projection	X_1
	Toe projection	X_2
	Stem thickness at the top of the wall	X_3
	Stem thickness at the bottom of the wall	X_4
	Base slab thickness	X_5
Variables related to RC design	Diameter of reinforcing bars of stem, ϕ_s	X_6
	Distance between reinforcing bars of stem, S_s	X_7
	Diameter of reinforcing bars of the toe, ϕ_t	X_8
	Distance between reinforcing bars of the toe, S_t	X_9
	Diameter of reinforcing bars of the heel, ϕ_h	X_{10}
	Distance between reinforcing bars of the heel, S_h	X_{11}

These variables (possible design solutions) are randomized (Eq. (1)) within a defined range using upper (X_i^{max}) and lower limits (X_i^{min}).

$$X_i^{min} \le X_i \le X_i^{max} . \quad (1)$$

By positioning each solution vector to a row, general form of the solution matrix can written as

$$CL = \begin{bmatrix} X_{1,1} & X_{1,2} & \cdots & X_{1,vn} \\ X_{2,1} & X_{2,2} & \cdots & X_{2,vn} \\ \vdots & \vdots & & \vdots \\ X_{pn-1,1} & X_{pn-1,2} & \cdots & X_{pn-1,vn} \\ X_{pn,1} & X_{pn,2} & & X_{pn,vn} \end{bmatrix}. \quad (2)$$

Then, strength capacity and safety for stability of each retaining walls are checked by using constrains given in Table 2. The requirements of TS500/2000 regulation are considered for calculation strength capacity of sections and extremum limits.

Before the next step, the objective functions (total costs) for each retaining walls are calculated (Eq. 3) and stored in a vector for future comparisons.

$$min\, f(X) = C_C \cdot V_c + C_s \cdot W_s\,. \quad (3)$$

In Eq. (3), C_c is unit cost of concrete C_s unit cost of steel, V_c is volume of concrete and W_s is weight of steel per unit length.

Step III: According to TLBO rules, in the third step, teacher and learner phases are respectively applied in order to improve solutions. Mathematically, teacher (tp) and learner (lp) phases can be written as

$$X_{new,i}^{ip} = X_{old,i} + rnd\,(0,1) \cdot (X_{teacher} - T_F \cdot X_{mean})\,, \quad (4)$$

$$X_{new,i}^{lp} = \begin{cases} X_{old,i} + rnd \cdot (X_i - X_j);\ f(X_i) > f(X_j) \\ X_{old,i} + rnd \cdot (X_j - X_i);\ f(X_i) < f(X_j) \end{cases}, \quad (5)$$

respectively. In the Eqs. (3) and (4), $X_{teacher}$ is the vector with best (minimum total cost) objective function in the solution matrix and it is defined as

$$X_{teacher} = x_{minf(X)}\,. \quad (6)$$

X_{mean} is the mean value of the design variables formulated as

$$X_{mean} = \frac{\sum_{i=1}^{pn} X_i}{pn}. \quad (7)$$

T_F is an integer number called teaching factor written as

$$T_F = round\,[1 + rnd(0.1)] \rightarrow \{1 - 2\}\,, \quad (8)$$

and it can be 1 or 2 according to the *rnd* (random reel number between 0 and 1) value. $X_{old,i}$ and $X_{new,i}$ represent old and new values of the variables, respectively. After updating the design variables at each phase, the objective function of the new vector is calculated and compared with the values of the old vector.

Step IV: In this step, the stopping criterion is checked. The iterative process continue from the Step III, until the stopping criterion is satisfied.

Table 2. Constraints on strength and dimensions of wall.

Description	Constraints
Safety for overturning stability	$g_1(X)$: $SF_{O,design} \geq SF_O$
Safety for sliding stability	$g_2(X)$: $SF_{S,design} \geq SF_S$
Safety for bearing capacity	$g_3(X)$: $SF_{B,design} \geq SF_B$
Minimum bearing stress, q_{min}	$g_4(X)$: $q_{min} \geq 0$
Flexural strength capacities of critical sections, M_d	$g_{5\text{-}7}(X)$: $M_d \geq M_u$
Shear strength capacities of critical sections, V_d	$g_{8\text{-}10}(X)$: $V_d \geq V_u$
Minimum reinforcement areas of critical sections, A_{smin}	$g_{11\text{-}13}(X)$: $A_s \geq A_{smin}$
Maximum reinforcement areas of critical sections, A_{smax}	$g_{14\text{-}16}(X)$: $A_s \leq A_{smax}$
Maximum steel bars spacing of critical sections, S_{max}	$g_{17\text{-}19}(X)$: $S \leq S_{max}$
Minimum steel bars spacing of critical sections, S_{min}	$g_{20\text{-}22}(X)$: $S \geq S_{min}$
Minimum concrete cover, c_c	$g_{23}(X)$: $c_c \geq 70$ mm
Sectional limits	$g_{24}(X)$: $(X_2 + X_3) \geq X_1$
	$g_{25}(X)$: $(X_6 + X_7) \geq X_1$
Reinforcement development lengths, l_{db} and hook lengths, l_{dh}	$g_{26}(X)$: $l_{db,stem} \geq (X_5\text{-}c_c)$ or $l_{dh,stem} \geq (X_5\text{-}c_c)$
	$g_{27}(X)$: $l_{db,toe} \geq (X_1\text{-}X_2\text{-}c_c)$ or $12d_{b,toe} \geq (X_5\text{-}c_c)$
	$g_{28}(X)$: $l_{db,heel} \geq (X_2\text{+}X_3\text{-}c_c)$ or $12d_{b,heel} \geq (X_5\text{-}c_c)$
	$g_{29}(X)$: $l_{db,key} \geq (X_5\text{-}c_c)$ or $l_{dh,key} \geq (X_5\text{-}c_c)$

3. Numerical Example

The proposed methodology is applied to a cantilever retaining wall benchmark problem that described in Saribaş and Erbatur (1996). Design constraints and ranges of design variables for the problem can be seen in Table 3. The optimum costs were investigated under three different cases related with backfill slope angle, surcharge load and compressive strength of concrete. In order to compare the effectiveness of the presented approach, two other metaheuristic methods; PSO (Ahmadi-Nedushan and Varaee, 2009) and BBBC (Camp and Akin, 2012) were also adapted to the numerical example.

The convergence to the optimum cost value of the methods can be seen in Fig. 1. As seen from the plot, although all methods are achieved to find the optimum result, the TLBO is better than the other methods. As a result, the TLBO is the best method in point of computational effort (for obtaining the optimum results more quickly).

In order to investigate statistical treatment of results in comparisons, averages and standard deviations of methods were calculated for different values of backfill slope angle. For each value of the backfill slope angle 100 independent runs were performed. The averages and standard deviations can be seen in Figs. 2 and 3.

Table 3. Design constants and ranges of design variables.

Definition	Symbol	Unit	Value
Height of stem	H	m	3.0
Yield strength of steel	f_y	MPa	420
Compressive strength of concrete	f'_c	MPa	30
Concrete cover	c_c	mm	70
Max. aggregate diameter	D_{max}	mm	16
Elasticity modulus of steel	E_s	GPa	200
Specific gravity of steel	γ_s	t/m³	7.85
Specific gravity of concrete	γ_c	kN/m³	23.5
Cost of concrete per m³	C_c	₺	119
Cost of steel per ton	C_s	₺	1751
Design load factor		LF	1.7
Surcharge load	q	kPa	20
Backfill slope angle	β	°	10
Internal friction angle of retained soil	ϕ_R	°	30
Internal friction angle of base soil	ϕ_B	°	0
Unit weight of retained soil	γ_R	kN/m³	17.5
Unit weight of base soil	γ_B	kN/m³	18.5
Cohesion of retained soil	c_R	kPa	0
Cohesion of base soil	c_B	kPa	125
Depth of the soil in front of wall	D	m	0.5
Safety for overturning stability	$SF_{O,design}$	-	1.5
Safety for sliding stability	$SF_{S,design}$	-	1.5
Safety for bearing capacity	$SF_{B,design}$	-	3.0
Range of stem thickness at top	h_{stemt}	m	0.2-3
Range of heel projection	h_{basew}	m	0.2-10
Range of toe projection	h_{toepro}	m	0.2-10
Range of stem thickness at the bottom of wall	h_{stemb}	m	0.2-3
Range of base slab thickness	$h_{baseslab}$	m	0.2-3
Range of diameter of reinforcing bars of stem	ϕ_s	mm	16-50
Range of diameter of reinforcing bars of toe,	ϕ_t	mm	16-50
Range of diameter of reinforcing bars of heel	ϕ_h	mm	16-50

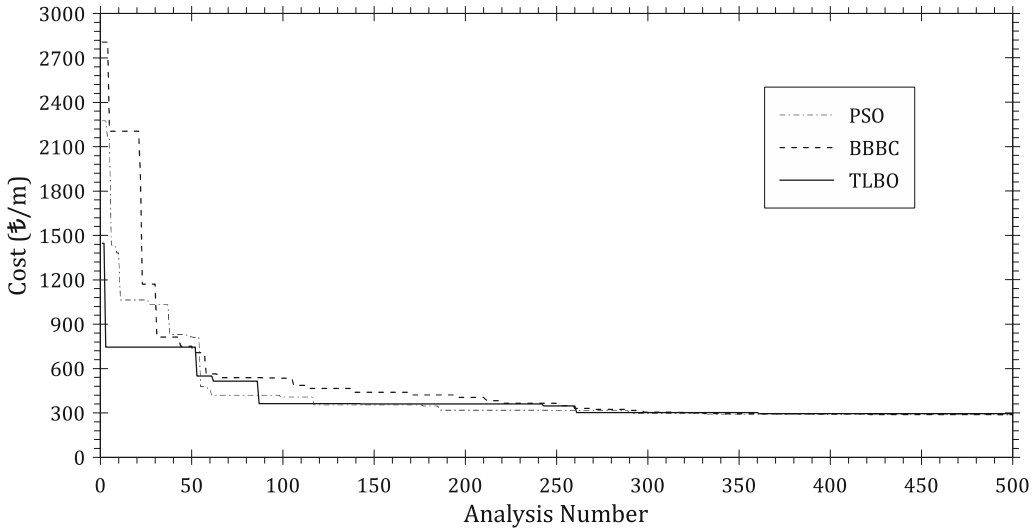

Fig. 1. Convergence to optimum results of methods.

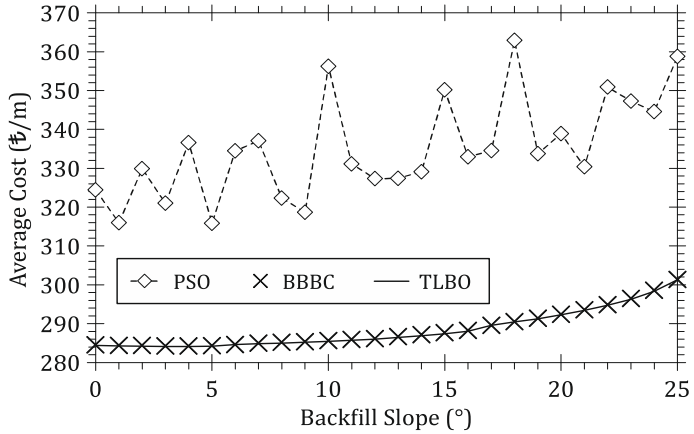

Fig. 2. Average cost values of the methods for different values of backfill slope angle.

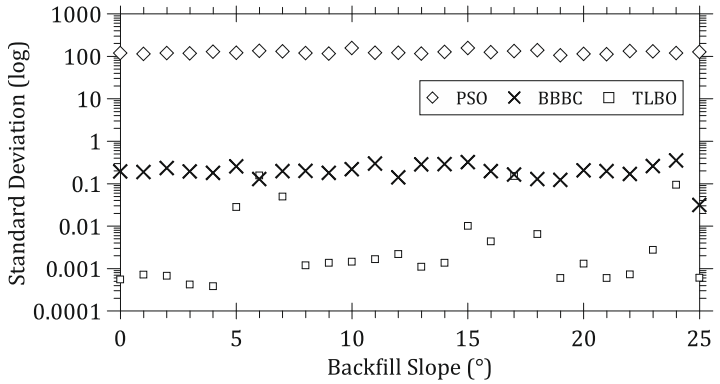

Fig. 3. Standard deviation values of 100 independent runs for different values of backfill slope angle.

100 independent runs were also conducted with different random numbers for investigation of the optimum results sensitivity of the methods. As seen from the Fig. 4, although the optimum results are obtained approximately 3 times bigger than true optimum value for some analyses of PSO and BBBC approaches, true optimums in all cases of TLBO method are found. According to the results, the algorithms can be sorted as TLBO, BBBC and PSO from the best to worst one.

In Figs. 5 and 6, effects of surcharge load and compressive strength of concrete to optimum cost can be seen. Minimum cost value is changed between 145₺-170₺ and 270₺-310₺ for different surcharge loads and compressive strengths respectively. Also, an approximate linear relationship is observed for both cases.

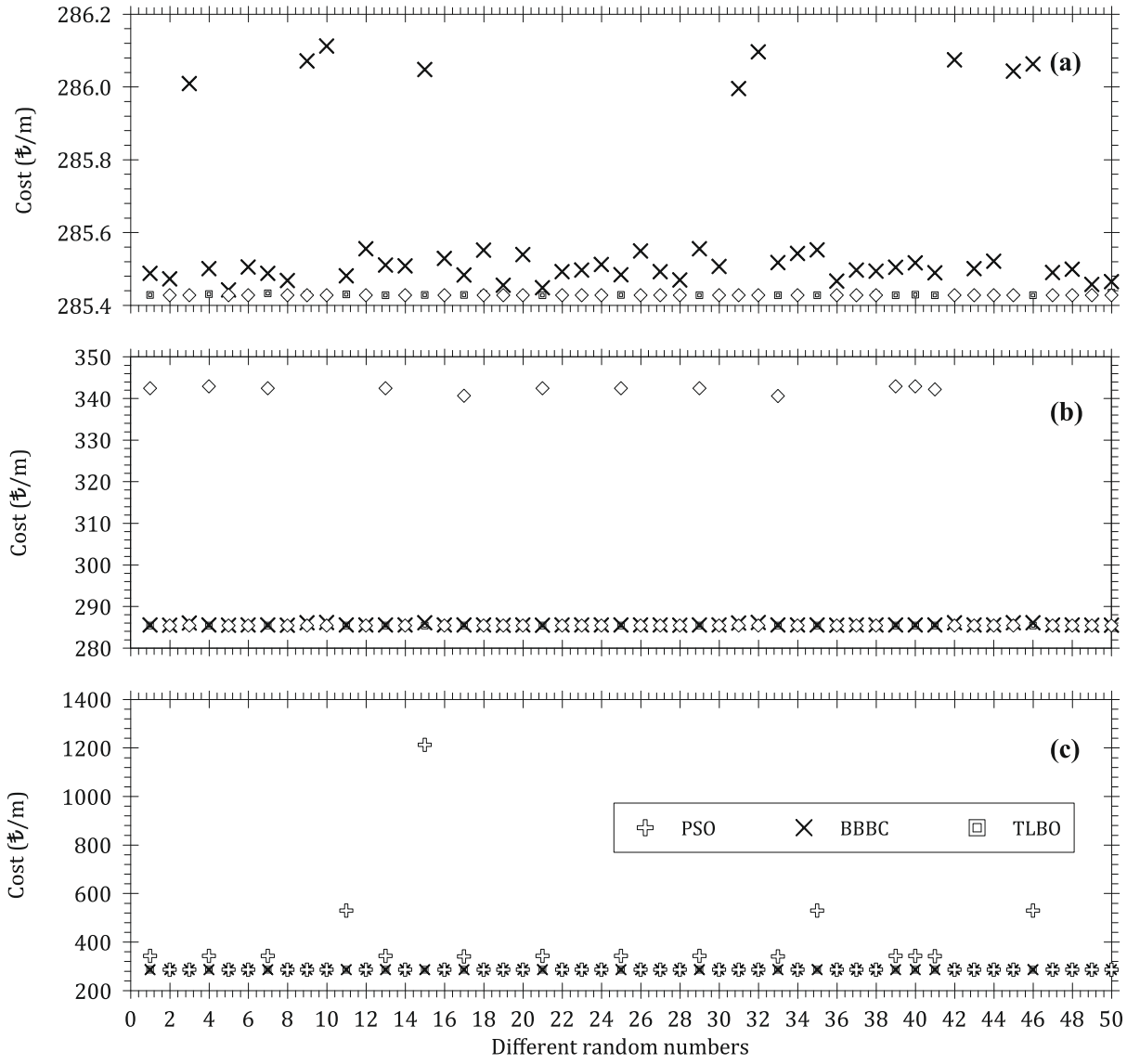

Fig. 4. Optimum cost distribution plot for 100 independent designs: (a) A more detailed graph of the 285.4₺-286.2₺ cost range; (b) A more detailed graph of the 280₺-350₺ cost range; (c) All solutions.

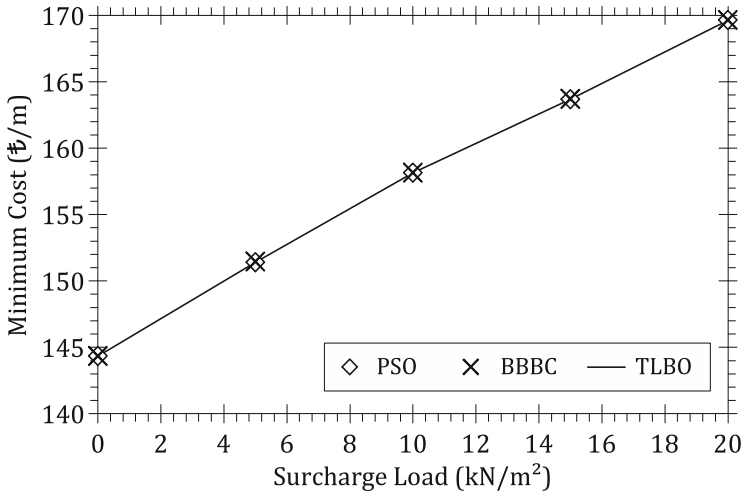

Fig. 5. Minimum cost vs. surcharge load plot.

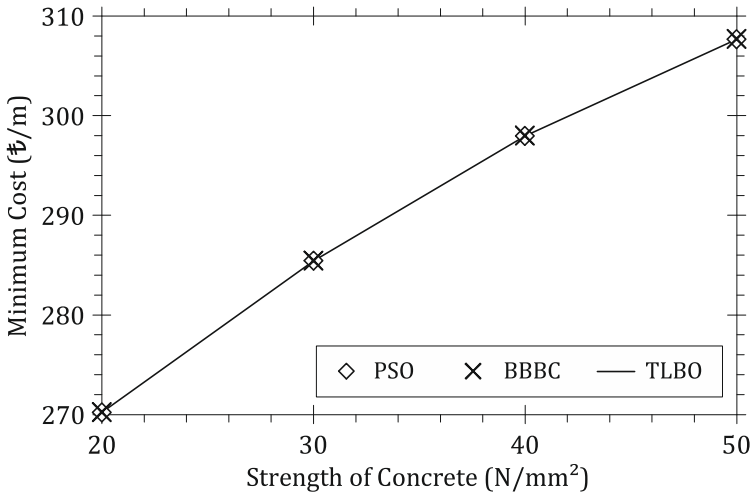

Fig. 6. Minimum cost vs. strength of concrete plot.

4. Conclusions

The optimum cost for cantilever retaining RC walls were investigated for different conditions such as, backfill slope angle, surcharge loads and compressive strength of concrete. In addition to proposed method with TLBO metaheuristic approach, optimization process were also conducted PSO and BBBS algorithms to show effectiveness of the presented approach. By conducting 100 independent run, statistical treatment of results were observed for all algorithms. According to the analyses results, all algorithms are successful in finding optimum design of the wall for all cases. But, the best computational time for optimum results is obtained for TLBO algorithm. Additionally, sensitivity of the TLBO is better than PSO and BBBC algorithm. As conclusion, TLBO is effective and suitable approach for optimum design of cantilever retaining RC walls considering TS 500/2000 regulation.

References

Ahmadi-Nedushan B, Varaee H (2009). Optimal design of reinforced concrete retaining walls using a swarm ıntelligence technique. *In The first International Conference on Soft Computing Technology in Civil, Structural and Environmental Engineering*, UK.

Ahmadkhanlou F, Adeli H (2005). Optimum cost design of reinforced concrete slabs using neural dynamics model. *Engineering Applications of Artificial Intelligence*, 18(1), 65-72.

Akin A, Saka MP (2010). Optimum detailed design of reinforced concrete continuous beams using the harmony search algorithm, In: Topping BHV, Adam JM, Pallarés FJ, Bru R, Romero ML, eds. *Proceedings of the Tenth International Conference on Computational Structures Technology*, Paper 131, Civil-Comp Press, Stirlingshire, UK.

Akin A, Saka MP (2012). Optimum detailing design of reinforced concrete plane frames to ACI 318-05 using the harmony search algorithm. In: Topping BHV, ed. *Proceedings of the Eleventh International Conference on Computational Structures Technology*, Paper 72, Civil-Comp Press, Stirlingshire, UK.

Balling R, Yao X (1997). Optimization of reinforced concrete frames. *Journal of Structural Engineering-ASCE*, 123, 193-202

Barros MHFM, Martins RAF, Barros AFM (2005). Cost optimization of singly and doubly reinforced concrete beams with EC2-2001. *Structural and Multidisciplinary Optimization*, 30, 236-242.

Barros AFM, Barros MHFM, Ferreira CC (2012). Optimal design of rectangular RC sections for ultimate bending strength. *Structural and Multidisciplinary Optimization*, 45, 845-860.

Bekdaş G, Nigdeli SM (2012). Cost optimization of T-shaped reinforced concrete beams under flexural effect according to ACI 318. *3rd European Conference of Civil Engineering*, December 2-4, Paris, France.

Bekdaş G, Nigdeli SM (2016). Bat algorithm for optimization of reinforced concrete columns. Joint Annual Meeting of GAMM and DMV, March 7-11, Braunschweig, Germany.

Bekdaş G, Nigdeli SM (2014). Optimization of slender reinforced concrete columns. *85th Annual Meeting of the International Association of Applied Mathematics and Mechanics*, March 10-14, Erlangen, Germany.

Camp CV, Pezeshk S, Hansson H (2003). Flexural design of reinforced concrete frames using a genetic algorithm. *Journal of Structural Engineering-ASCE*, 129, 105-11.

Camp CV, Akin A (2012). Design of retaining walls using big bang–big crunch optimization. *Journal of Structural Engineering-ASCE*, 138(3), 438-448.

Camp CV, Huq F (2013). CO_2 and cost optimization of reinforced concrete frames using a big bang-big crunch algorithm. *Engineering Structures*, 48, 363-372.

Ceranic B, Freyer C, Baines RW (2001). An application of simulated annealing to the optimum design reinforced concrete retaining structure. *Computers Structures*, 79(17), 1569-1581.

Coello CC, Hernandez FS, Farrera FA (1997). Optimal design of reinforced concrete beams using genetic algorithms. *Expert Systems with Applications*, 12, 101-108.

Coello CC, Christiansen AD, Hernández FS (1997). A simple genetic algorithm for the design of reinforced concrete beams. *Engineering with Computers*, 13(4), 185-196.

Fedghouche F, Tiliouine B (2012). Minimum cost design of reinforced concrete T-beams at ultimate loads using Eurocode2. *Engineering Structures,* 42, 43-50.

Ferreira CC, Barros MHFM, Barros AFM (2003). Optimal design of reinforced concrete T-sections in bending. *Engineering Structures,* 25(7), 951-964.

Gil-Martin LM, Hernandez-Montes E, Aschheim M (2010). Optimal reinforcement of RC columns for biaxial bending. *Materials and Structures*, 43, 1245-1256.

Govindaraj V, Ramasamy JV (2005). Optimum detailed design of reinforced concrete continuous beams using genetic algorithms. *Computers and Structures*, 84, 34-48.

Govindaraj V, Ramasamy JV (2007). Optimum detailed design of reinforced concrete frames using genetic algorithms. *Engineering Optimization*, 39(4), 471-494.

Guerra A, Kiousis PD (2006). Design optimization of reinforced concrete structures. *Computers and Concrete*, 3, 313–334.

Kaveh A, Abadi ASM (2011). Harmony search based algorithms for the optimum cost design of reinforced concrete cantilever retaining walls. *International Journal of Civil Engineering*, 9(1), 1-8.

Kaveh A, Sabzi O (2012). Optimal design of reinforced concrete frames using big bang-big crunch algorithm. *International Journal of Civil Engineering*, 10(3), 189-200.

Lee C, Ahn J (2003). Flexural design of reinforced concrete frames by genetic algorithm. *Journal of Structural Engineering-ASCE*, 129(6), 762-774.

Nigdeli SM, Bekdaş G, Kim S, Geem ZW (2015). A Novel Harmony Search Based Optimization of reinforced concrete biaxially loaded columns. *Structural Engineering and Mechanics*, 54(6), 1097-1109

Paya I, Yepes V, Gonzalez-Vidosa F, Hospitaler A (2008). Multi objective optimization of concrete frames by simulated annealing. *Computer-Aided Civil and Infrastructure Engineering*, 23, 596-610.

Paya-Zaforteza I, Yepes V, Hospitaler A, Gonzalez-Vidosa F (2009). CO_2-optimization of reinforced concrete frames by simulated annealing. *Engineering Structures*, 31, 1501-1508.

Perea C, Alcala J, Yepes V, Gonzalez-Vidosa F, Hospitaler A (2008). Design of reinforced concrete bridge frames by heuristic optimization. *Advances in Engineering Software*, 39, 676-688.

Rafiq MY, Southcombe C (1998). Genetic algorithms in optimal design and detailing of reinforced concrete biaxial columns supported by a declarative approach for capacity checking. *Computers and Structures*, 69, 443-457.

Rajeev S, Krishnamoorthy CS (1998). Genetic algorithm–based methodology for design optimization of reinforced concrete frames. *Computer-Aided Civil and Infrastructure Engineering*, 13, 63-74.

Rama Mohan Rao AR, Shyju PP (2010). A meta-heuristic algorithm for multi-objective optimal design of Hybrid Laminate Composite Structures. *Computer-Aided Civil and Infrastructure Engineering*, 25(3), 149-170.

Rao RV, Savsani VJ, Vakharia DP (2011). Teaching-learning-based optimization: a novel method for constrained mechanical design optimization problems. *Computer-Aided Design*, 43(3), 303-315.

Saribas A, Erbatur F (1996). Optimization and sensitivity of retaining structures. *Journal of Geotechnical Engineering*, 122(8), 649-656.

Sirca Jr G, Adeli H (2005). Cost optimization of prestressed concrete bridges. *Journal of Structural Engineering-ASCE*, 131(3), 380-388.

Temur R, Bekdas G (2016). Teaching learning-based optimization for design of cantilever retaining walls. *Structural Engineering and Mechanics*, 57(4), 763-783.

Yepes V, Alcala J, Perea C, Gonzalez-Vidosa F (2008). A parametric study of optimum earth-retaining walls by simulated annealing. *Engineering Structures*, 30, 821-830.

Challenge Journal of Structural Mechanics

Influence of blast-induced ground motion on dynamic response of masonry minaret of Yörgüç Paşa Mosque

Olgun Köksal [a], Kemal Hacıefendioğlu [b,*], Emre Alpaslan [b], Fahri Birinci [b]

[a] *Kavak Vocational School, Ondokuz Mayıs University, 55850 Samsun, Turkey*
[b] *Department of Civil Engineering, Ondokuz Mayıs University, 55139 Samsun, Turkey*

ABSTRACT

This paper focuses on the dynamic response analysis of masonry minaret of Yörgüç Paşa Mosque subjected to artificially generated surface blast-induced ground motion by using a three-dimensional finite element model. The mosque is located in the town of Kavak of Samsun, in Turkey. This study intended to determine the ground motion acceleration values due to blast-induced ground motions (air-induced and direct-induced) calculated by a random method. In order to model blast-induced ground motion, firstly, peak acceleration and the time envelope curve function of ground motion acceleration were obtained from the distance of the explosion center and the explosion charge weight and then blast-induced acceleration time history were established by using these factors. Non-stationary random process is presented as an appropriate method to be produced by the blast-induced ground motion model. As a representative of blast-induced ground motion, the software named BlastGM (Artificial Generation of Blast-induced Ground Motion) was developed by authors to predict ground motion acceleration values. Artificial acceleration values generated from the software depend on the charge weight and distance from the center of the explosion. According to the examination of synthetically generated acceleration values, it can be concluded that the explosions cause significant effective ground movements. In the paper, three-dimensional finite element model of the minaret was designed by ANSYS. Moreover, the maximum stresses and displacements of the minaret were investigated. The results of this study indicate that the masonry minaret has been affected substantially by effects of blast-induced ground motion.

ARTICLE INFO

Article history:
Received 20 October 2016
Accepted 9 December 2016

Keywords:
Masonry minaret
Blast induced ground motion
Dynamic response
Random process

1. Introduction

Blasting is used in jobs such as construction, mining, oil and agriculture and forestry in our country and in the world. Blast technology is commonly applied to most civil engineering applications such as housing, railways, roads, dams, airports. However, while blasting is advantageous, it is also disadvantageous. Negative effects are occurred such as ground motion and air shock during blasting operations. This paper examines the effects of blast-induced ground motion on dynamic response of historical masonry minarets.

Once an explosion originates at approximate the ground surface, ground shock results from the energy given to the ground due to the explosion. Some of this energy is transmitted through the air in the form of air-induced ground shock and some is transmitted through the ground as direct-induced ground shock. Air-induced ground shock results when the air-blast shock wave compresses the ground surface and sends a stress pulse into the underlying media. The magnitude and duration of the stress pulse in the ground depend on the character of the air-blast pulse and the ground media. Generally, the air-induced ground motions are downward. They are

* *Corresponding author*. Tel.: +90-362-3121919 ; E-mail address: hckemal@omu.edu.tr (K. Hacıefendioğlu)
ISSN: 2149-8024 / DOI: https://doi.org/10.20528/cjsmec.2016.12.036

maximum at the ground surface and attenuate with depth. However, the presence of a shallow water table, a shallow soil-rock interface, or other discontinuities can alter the normal attenuation process (UFC, 2008).

Direct-induced ground shock results from the explosive energy being transmitted directly through the ground. This motion includes both the true direct-induced motions and cratering-induced motions. The latter generally have longer durations and are generated by the crater formation process in cratering explosions. The induced ground motion resulting from both types have a longer duration than air-blast-induced ground shock and the wave forms tend to be sinusoidal (UFC, 2008).

2. Modelling of Blast-Induced Ground Motion

Blast-induced ground motions are high frequency and very short-term. This ground motions are effected by many parameters such as TNT charge weight, the distance between the explosion center and structure, depth of charge center, geotechnical properties of soil and rock. Seismic analysis is often done for all structures. Similarly, dynamic analysis even must be done for structures subjected to blast-induced ground motion. Therefore, this study is very important. Moreover, both in our country and in the world, researchers are interested in blast-induced ground motion (Wu and Hao, 2004, 2007; Ma et al., 2004; Hao and Wu, 2005; Lu and Wang, 2006; Wu et al., 2005; Singh and Roy, 2010; Hacıefendioğlu et al., 2012, 2014). Fig. 1 shows a structure at distance of R from charge center.

Peak particle acceleration and time envelope function of explosion pressure are used in blast-induced ground motion modelling. Peak particle acceleration (*PPA*) depends on TNT charge weight and the distance between the explosion center and structure. Non-stationary random process method is used for the modeling of blast-induced ground motions (Ruiz and Penzien, 1969). In this study, time histories of ground shocks are simulated by BlastGM (Artificial Generation of Blast-induced Ground Motion) software (Köksal, 2013). Thanks to this software, it is generated that artificial acceleration values depend on TNT charge weight and the distance between the explosion center and structure. Moreover, velocity, displacement and explosion pressure is generated with this software.

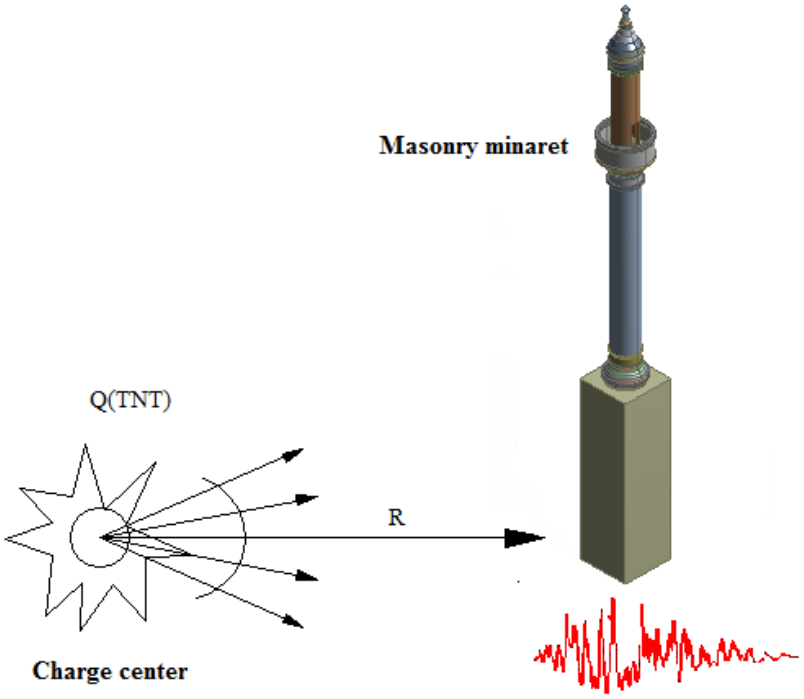

Fig. 1. Masonry minaret at distance of R from charge center.

3. Direct-induced ground motion

For the granite site, the *PPA* of acceleration time history was predicted as a function of charge weight and distance by

$$PPA = 3.979R^{-1.45}Q^{1.07}\,, \tag{1}$$

in which, *PPA* (g) is peak particle acceleration, R (m) is the distance between the explosion center and structure, and Q (kg) is TNT charge weight (Wu ve Hao, 2005).

Non-stationary random process method is used for the modeling of blast-induced ground motions in this study. In this method, the shape function ($p(t)$) and stationary process ($w(t)$) are used to characterize seismic ground vibration nonstationarity in the time domain (Bolotin, 1960; Jennings et al., 1969; Ruiz and Penzien, 1969). Acceleration time history can be expressed with two equations (Amin and Ang, 1968).

$$a_b(t) = p(t)\,w(t)\,. \tag{2}$$

The shape function is obtained by the Hilbert transform (Kanasewich, 1981). This function is used to blast induced ground motion as follows (Wu and Hao, 2005).

$$p(t) = \begin{cases} 0, & t \le 0, \\ mte^{-nt^2} & t > 0, \end{cases} . \quad (3)$$

In this equation, m and n are parameters depend on non-stationary characteristics of ground motion. e is the base of natural logarithm. m and n parameters depend on t_p that is the duration for ground shock to reach its peak value from t_a (Wu and Hao, 2005).

$$t_P = \sqrt{1/2n}\,, \quad (4)$$

$$m = \sqrt{2ne}\,. \quad (5)$$

From the experimental data, the arrival time at a point on ground surface with a distance R from charge center can be determined by Eq. (6).

$$t_a = 0.91R^{1.03}Q^{-0.02}/c_s\,, \quad (6)$$

where c_s is the P wave velocity of the granite site type. The empirical equation of the time instant t_p is estimated by Eq. (7).

$$t_p = 5.1 \times 10^{-4} Q^{0.27} (R/Q^{1/3})^{0.81} = 5.1 \times 10^{-4} R^{0.81}\,, \quad (7)$$

where t_p (s) only depends on R distance. In this study, ground shock wave duration t_d is expressed as in Eq. (8).

$$t_d = t - t_a\,. \quad (8)$$

Fig. 2 shows the envelope function for simulated acceleration time histories on granite site at 20 m from the charge center with a charge weight of 100 kg. BlastGM is used to plot envelope function of blast-induced ground motion.

The wave forms of the bedrock acceleration are derived from second order differential equation as shown in Eqs. (9a, 9b).

$$z + 2\xi\omega_0 z + \omega_0 z = -a_b(t)\,, \quad (9a)$$

$$a_g(t) = -2\xi\omega_0 z + \omega_0^2 z\,. \quad (9b)$$

The solution of Eq. (9) can be obtained by using step-by-step procedure (Ruiz and Penzien, 1969). Fig. 3 shows acceleration time histories on granite site at 20m from the charge center with charge weights of 100 kg, 500 kg and 1000 kg.

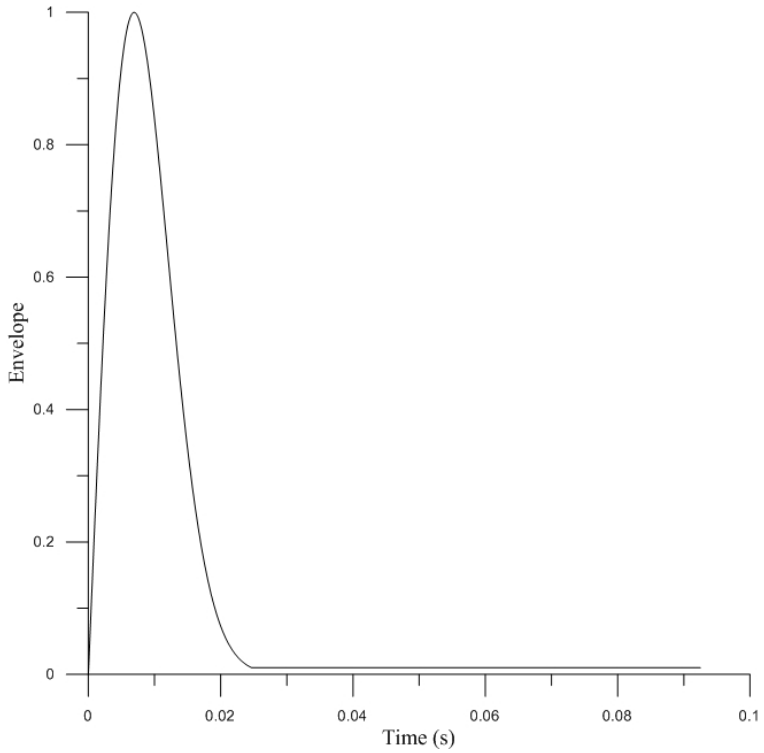

Fig. 2. Time intensity envelope function of blast-induced ground motion.

4. Finite Element Modelling of Yörgüç Paşa Mosque's Masonry Minaret

The mosque is located in the town Kavak of Samsun, in Turkey. It was built by Pasha Yörgüç in the Ottoman period. The first mosque made of wood. This mosque was collapsed. It was made of stone by Haji Yusuf in 1911. Its minaret complies with the Ottoman and the Seljuk architecture. In this study, masonry minaret of Yörgüç Paşa Mosque was selected for numerical modelling and dynamic analyses. Masonry structures can be subjected to ground motions due to the surface explosions.

Therefore, influence of blast-induced ground motion on dynamic response of masonry minaret of Yörgüç Paşa Mosque is examined by this study. Fig. 4 shows photograph, geometrical properties and finite element model of Yörgüç Paşa Mosque's minaret.

Masonry minaret of Yörgüç Paşa Mosque is modelled by using ANSYS (2014) that computes the dynamic response of the masonry minaret. The maximum height of the minaret is 25.55 meters. Three-dimensional (3D) SOLID45 elements are exhibited a quadratic displacement behavior, model the minaret body, the internal helical stair and the foundation. Table 1 shows material properties of the minaret taken from literature (Hacıefendioğlu, 2010).

Table 1. Material properties of the minaret.

Material	Elasticity Modulus (N/m^2)	Poisson's Ratio	Mass Density (kg/m^3)
Masonry minaret	$2x10^9$	0.2	1600

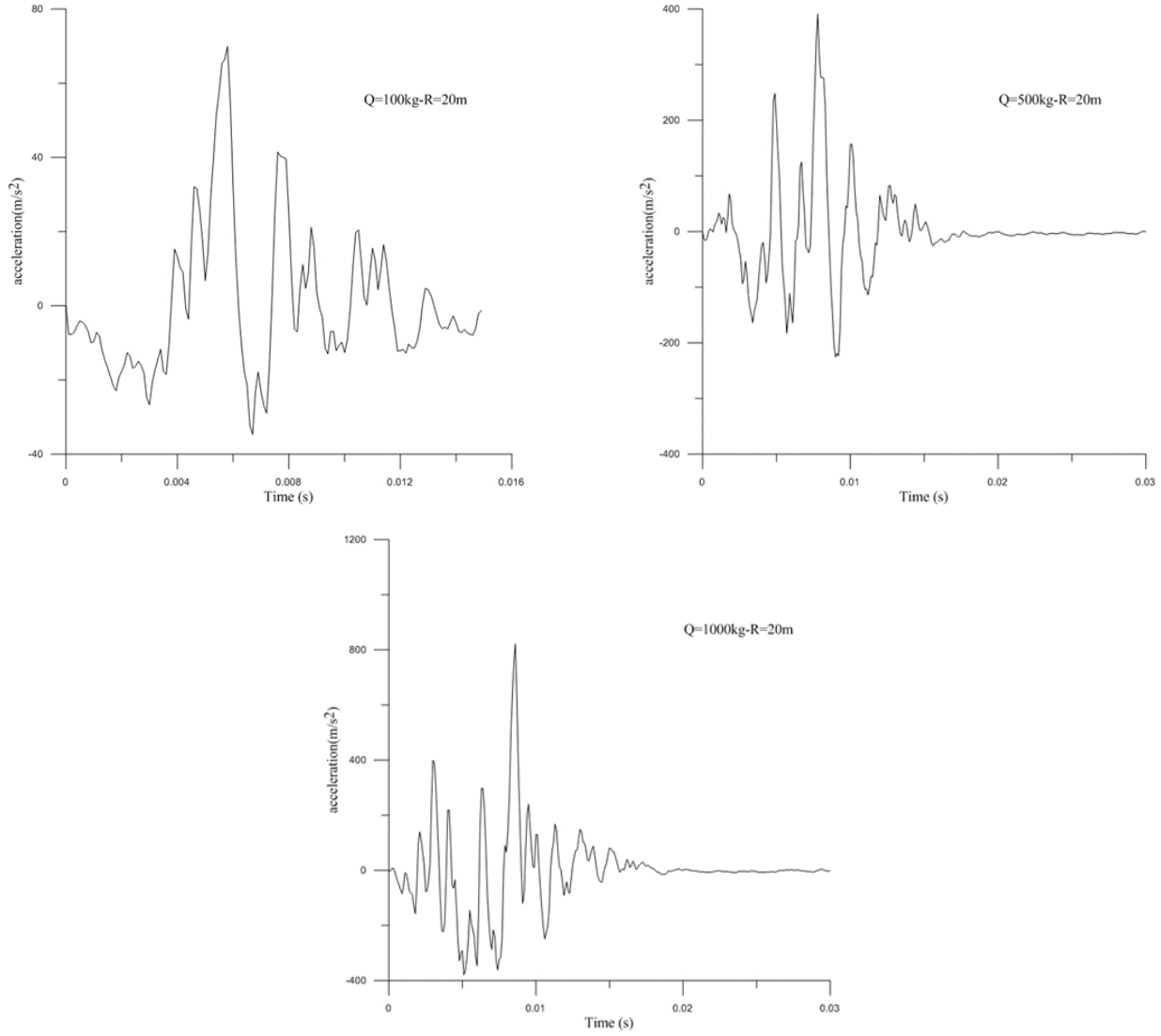

Fig. 3. Acceleration time histories of blast-induced ground motion.

5. Formulation of Equation of Motion

The matrix equation of motion with nonlinear stiffness under blast-induced excitation for multi-degree of freedom system can be written as

$$[\mathrm{M}]\{\ddot{U}\} + [\mathrm{C}]\{\dot{U}\} + [\mathrm{K}]\{U\} = \{F\}, \tag{10}$$

in which M, C and K are the mass, damping and stiffness matrices, respectively $\ddot{U}$, $\dot{U}$ and U are the vectors of the acceleration, velocity and displacement, respectively. Newmark-β method is used for blast-induced ground motion. In this method

$$\begin{bmatrix} U_{k+1} \\ \dot{U}_{k+1} \\ \ddot{U}_{k+1} \end{bmatrix} = F_N \begin{bmatrix} U_k \\ \dot{U}_k \\ \ddot{U}_k \end{bmatrix} + H_N F_{k+1}, \tag{11}$$

$$F_N = \frac{1}{\beta}\begin{bmatrix} \beta - \omega_n^2\alpha(\Delta t)^2 & \beta\Delta t - 2\zeta\omega_n\alpha(\Delta t)^2 - \omega_n^2\alpha(\Delta t)^3 & \frac{1}{2}\beta(\Delta t)^2 - \alpha(\beta+\gamma)(\Delta t)^2 \\ -\omega_n^2\delta\Delta t & \beta - 2\zeta\omega_n\delta\Delta t - \omega_n^2\delta(\Delta t)^2 & \beta\Delta t - \delta(\beta+\gamma)\Delta t \\ -\omega_n^2 & -2\zeta\omega_n - \omega_n^2\Delta t & -\gamma \end{bmatrix}, \quad (12)$$

$$H_N = \left(\frac{1}{m\beta}\right)\begin{bmatrix} a(\Delta t)^2 \\ \delta\Delta t \\ 1 \end{bmatrix}, \quad (13)$$

$$q_k = \begin{bmatrix} U_k \\ \dot{U}_k \\ \ddot{U}_k \end{bmatrix}, \quad (14)$$

$$q_{k+1} = F_N q_k + H_N F_{k+1}\,. \quad (15)$$

Numerical analysis is done using Eqs. (11), (12), (13), (14) and (15) (Hart and Wong, 1999).

6. Numerical Application

Three different charge weights with single charge center were simulated to analyze the dynamic response of blast-induced ground motion. According to these ground motions, the maximum displacements and von Mises stresses (VMS) through the height of the minaret were evaluated. Fig. 5 shows displacement values at t=0.0059, 0.0079, 0.0087 sec in x-direction of ground motions occurred at 20m from the charge center with charge weights of 100 kg, 500 kg and 1000 kg. Fig. 6 shows von Mises stresses (VMS) at t=0.0059, 0.0079 and 0.0087 sec of ground motions occurred at 20 m from the charge center with charge weights of 100kg, 500kg and 1000kg.

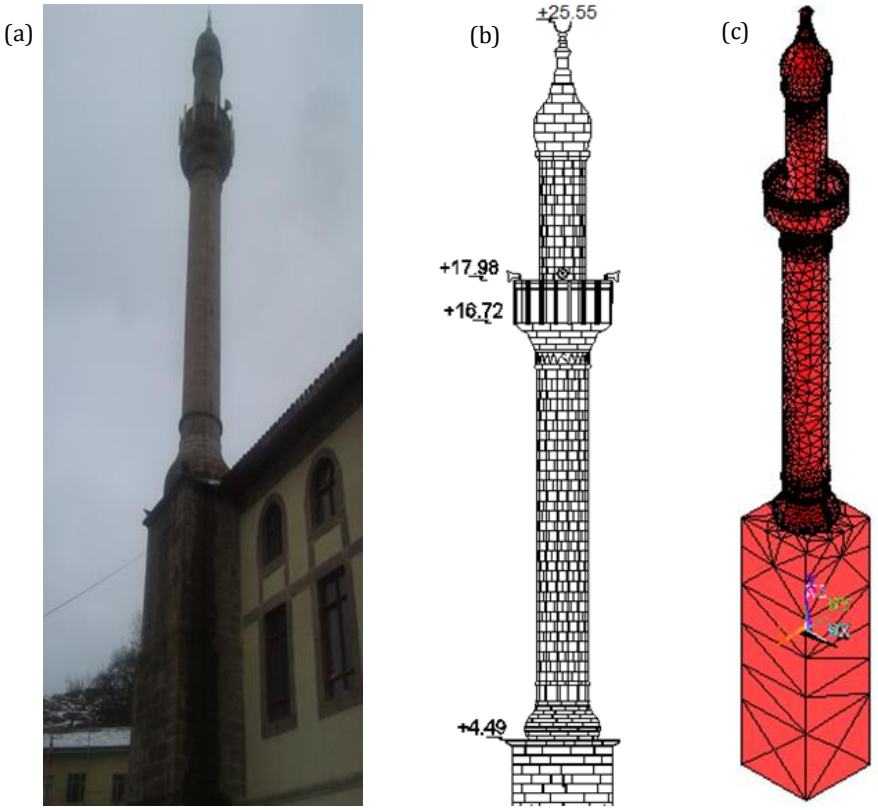

Fig. 4. (a) Photograph, (b) drawing and (c) finite element model of Yörgüç Paşa Mosque's minaret.

7. Conclusions

The main aim of this paper is to investigate the effect of blast-induced ground motions on dynamic response of masonry minaret structures. For this purpose, a minaret was chosen and modeled by the finite element method in ANSYS software program. Blast-induced ground accelerations is obtained in the BlastGM software that developed by authors. The dynamic response analysis is carried out for the masonry minaret of Yörgüç Paşa Mosque in Samsun, Turkey.

As a conclusion, while charge weight increases (constant charge center), displacements and von Mises stresses also increase. Therefore, it can be observed that blast-induced ground motions have a significant effect on dynamic behaviour of masonry minarets.

Acknowledgements

The authors are grateful to The Prime Ministry of Turkey, General Directorate of Foundations, Samsun Regional Directorate for technique information of Yörgüç Paşa Mosque.

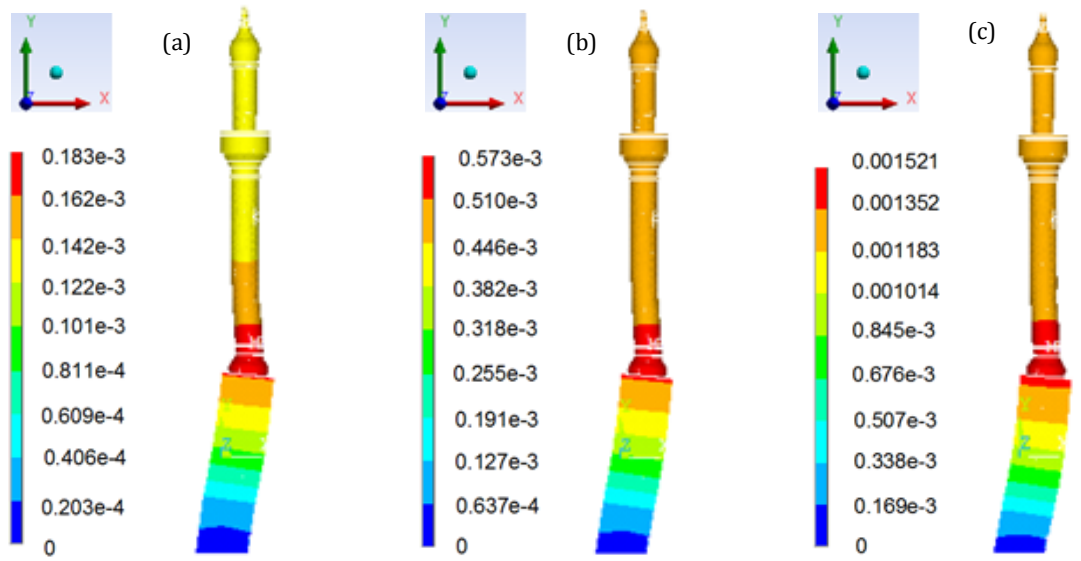

Fig. 5. Displacements obtained by blast-induced ground motion for:
(a) 100 kg TNT-20m; (b)500 kg TNT-20m; (c)1000 kg TNT-20m.

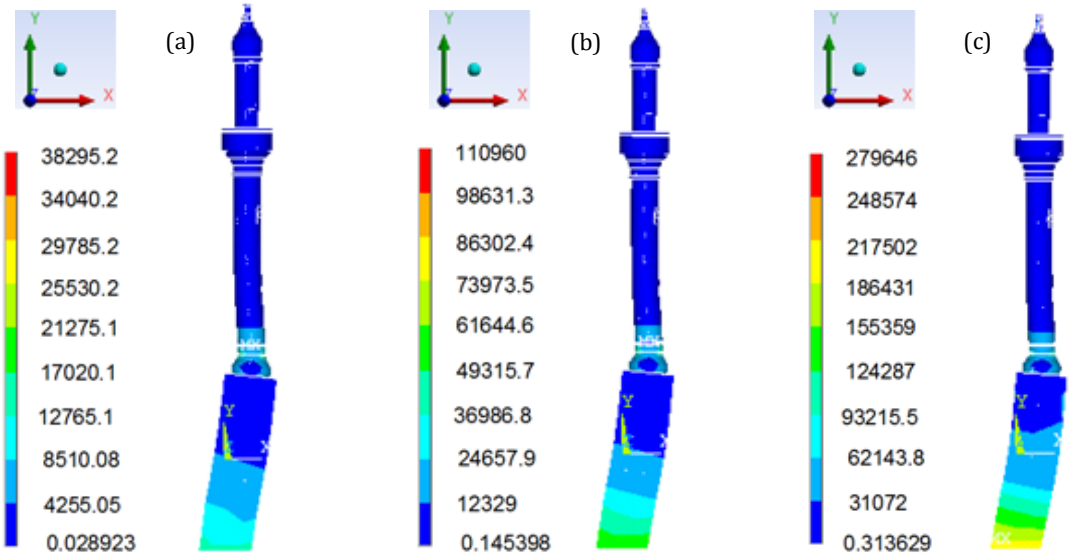

Fig. 6. von Mises stress contours obtained by blast-induced ground motion for:
(a) 100kg TNT-20m; (b)500kg TNT-20m; (c)1000kg TNT-20m.

REFERENCES

ANSYS 14 (2014). Swanson Analysis System, USA.

Amin M, Ang AHS (1968). A non-stationary stochastic model of earthquake motion. *Journal of Engineering Mechanics Division-ASCE*, 94(2), 559-583.

Bolotin VV (1960). Statistical theory of the aseismic design of structures. *Proceedings of the 2nd World Conference on Earthquake Engineering*, Tokyo, 2, 1365-1374.

Hacıefendioğlu K (2010). Seasonally frozen soil's effect on stochastic response of masonry minaret–soil interaction systems to random seismic excitation. *Cold Regions Science and Technology*, 60, 66–74.

Hacıefendioğlu K, Soyluk K, Birinci F (2012). Numerical investigation of stochastic response of an elevated water tank to random underground blast loading. *Stochastic Environmental Research and Risk Assessment,* 26(4), 599–607.

Hacıefendioğlu K, Alpaslan E (2014). Stochastically simulated blast-induced ground motion effects on nonlinear response of an industrial masonry chimney. *Stochastic Environmental Research and Risk Assessment*, 28, 415–427.

Hart CG, Wong K (1999). Structural Dynamics for Structural Engineers. John Wiley and Sons, Inc., Toronto,

Kanasewich ER (1981). Time sequence analysis in geophysics. The University of Alberta Press, Edmonton, Alberta, Canada.

Köksal O (2013). Dynamic Analysis of Elevated Steel Water Tank Subjected to Blast Induced Ground Motion. *M.Sc. Thesis*, Ondokuz Mayıs University, Samsun, Turkey.

Lu Y, Wang Z (2006). Characterization of structural effects from above-ground explosion using coupled numerical simulation. *Computers and Structures*, 84(28), 1729-1742.

Ruiz P, Penzien J (1969). PSEQN: Artificial generation of earthquake accelerograms. Earthquake Engineering Research Center, Report No EERC 69-3, University of California, Berkeley, USA.

Singh PK, Roy MP (2010). Damage to surface structures due to blast vibration. *International Journal of Rock Mechanics and Mining Sciences*, 47(6), 949-961.

UFC (Unified Facilities Criteria) (2008). Structures to Resist the Effects of Accidental Explosions. UFC 3-340-02, Department of Defense, US Army Corps of Engineers, Naval Facilities Engineering Command, Air Force Civil Engineer Support Agency, USA.

Wu C, Hao H (2004). Modeling of simultaneous ground shock and airblast pressure on nearby structures from surface explosions. *International Journal of Impact Engineering*, 31, 699–717.

Wu C, Hao H (2007). Numerical simulation of structural response and damage to simultaneous ground shock and airblast loads. *International Journal of Impact Engineering*, 556–572.

Wu C, Hao H, Lu Y (2005). Dynamic response and damage analysis of masonry structures and masonry infilled RC frames to blast ground motion. *Engineering Structures*, 27, 323–333.

Challenge Journal of Structural Mechanics

HVAC systems: measurements of airflows in small duct length

Clito Félix Alves Afonso *

Department of Mechanical Engineering, Engineering Faculty, Porto University, 4200-465 Porto, Portugal

ABSTRACT

One of the most feasible ways to measure duct airflows is by tracer gas techniques, especially for complex situations when the duct lengths are short as well as their access, which makes extremely difficult or impossible other methods to be implemented. One problem associated with the implementation of tracer gas technique when the ducts lengths are short is due to the impossibility of achieving complete mixing of the tracer with airflow and its sampling. In this work, the development of a new device for the injection of tracer gas in ducts is discussed as well as a new tracer-sampling device. The developed injection device has a compact tubular shape, with magnetic fixation to be easy to apply in duct walls. An array of sonic micro jets in counter current direction, with the possibility of angular movement according to its main axle ensures a complete mixing of the tracer in very short distances. The tracer-sampling device, with a very effective integration function, feeds the sampling system for analysis. Both devices were tested in a wind tunnel of approximately 21m total length. The tests distances between injection and integration device considered were: $X/Dh = 22$; $X/Dh = 4$; $X/Dh = 2$; and $X/Dh = 1$. For very short distances of $X/Dh = 2$ and $X/Dh = 1$, semi empirical expressions were needed. A good reproducibility of airflow rate values was obtained. These preliminary tests showed that the practical implementation of tracer gas techniques in HVAC systems for measuring airflow rates with a very short mixing distance is possible with the devices developed.

ARTICLE INFO

Article history:
Received 9 September 2016
Accepted 6 November 2016

Keywords:
Tracer gas
Airflow
Constant emission
Injection device
Sampling device
Sonic micro jet

1. Introduction

Tracer gas techniques in the measurement of airflows have innumerable advantages when compared with other more conventional methods, as explained by Rifat (1990), namely its high precision, independence of the flow complexity, almost no flow disturbance, and good flow asymmetry tolerance. Airflows can be calculated with a very high precision in a range from very small airflows to high airflows. Important research work has been done by Cheong and Rifat (1992), Cheong (1994, 1996, 2001), Cheong and Chong (2000), Rifat and Lee (1990), Rifat and Cheong (1993) with the aim of application of tracer gas measurement in ducts, using 8mm tubular injection probe with a row of 3mm holes. Results were presented until a minimum distance between the tracer injection and sampling of $X/Dh = 7$. In countries like Sweden the method of duct airflow calculation by tracer gases is wide spread as per Dantec (2001), and has been implemented with simple multi tube tracer injection, for distances between de injection and sampling point great than $X/Dh = 10$. Carter (1998) obtained an important conclusion in his work: short period time sampling can give reliable airflow measurement.

Nomenclature

Dh	hydraulic diameter [m]
X	distance [m]
s	mean distance between jets orifices [m]
Q_{xDh}	airflow for distance $X/Dh =$ x [m^3/s]
$Corr_{xDh}$	airflow correction for distance $X/Dh =$ x [m^3/s]
$Q_{xDhcorr}$	corrected airflow for distance $X/Dh =$ x [m^3/s]

* *Corresponding author*. Tel.: +35-196-7619530 ; Fax: +35-122-5081440 ; E-mail address: clito@fe.up.pt (C. F. A. Afonso)
ISSN: 2149-8024 / DOI: https://doi.org/10.20528/cjsmec.2016.11.027

So to say in almost all work carried out in duct airflow measurements by tracer gas technique the plans of injection and sampling are located far way, ISO 4053/I (2003) and Grieve (1989). However, in situations of real application, the distances between those plans can be very close. Therefore, it is of great importance the development of new techniques studying the dispersion of tracer gas for short distances, even though values of $X/Dh = 1$.

The tracer gas technique had not been much spread, mainly because of the complexity and price of the equipment, mainly the analyzer. This fact restricts this technique to some research work in laboratory, and is not so practical for field measurements. However, in the last years, with the evolution of microelectronics, it become possible to construct portable equipment, with very high sensitivity, been light, compact and at relatively low price. Manly for the above reasons, and in the opinion of others authors CEDR (2003), this technique has the potential to become the standard method of duct airflow measurements, in a next future. This global context gives the motivation for the present work.

2. Injection Device Development

2.1. Initial conditions

The main objective of the present work is the development of a practical field deployable device, for tracer gas airflow measurement. This fact puts some initial conditions regarding the type and shape of the devices. The injection and sampling devices need to be simple to be implemented in ducts. The simplest way of carrying out this desiderate is making appeal to tubular configurations. So, with only two duct orifices with the same diameter, the injection and sampling probes can be easily applied to duct walls. For commodity, the present devices have the possibility of magnetic fixation to common steel ducts. Concluding, the injection must be carried out through only one inlet and not in a series of inlets, to have success in its practical application.

2.2. Injection device design

The present work tries to solve the major difficulty for tracer gas injection devices for duct airflow measurements: the capacity of gas dispersion in extremely short distances $(X/Dh = 1)$. This need, and the initial condition of a unique tracer gas inlet, poses a great design challenge. The present solution consists of a 300mm nominal length probe, Fig. 1, with an array of 200-micron diameter micro sonic jets feed by four distribution chambers.

The probe diameter is 12.5 mm. Four miniaturized hydraulic equilibrated circuits, with only one common inlet, feed these chambers. This number four comes from analyses of the geometry of all the circuit. Fig. 2 represents the ratio of velocities versus the number of distribution chambers. One immediate conclusion from this figure is the benefice of the distribution chambers, to minimize velocities gradients, and consequently minimized pressures gradients. The array of sonic jets (15 in each chamber) is then feed by near equal pressures. The injection orifices are all equal in diameter, made by high precision technique, and operating in sonic regime. So, the tracer gas flow obtained with this arrangement is almost equal for all the jets of the array and the tracer gas injection along the body of the probe is well balanced. The sampling device works exactly same principle but in vacuum.

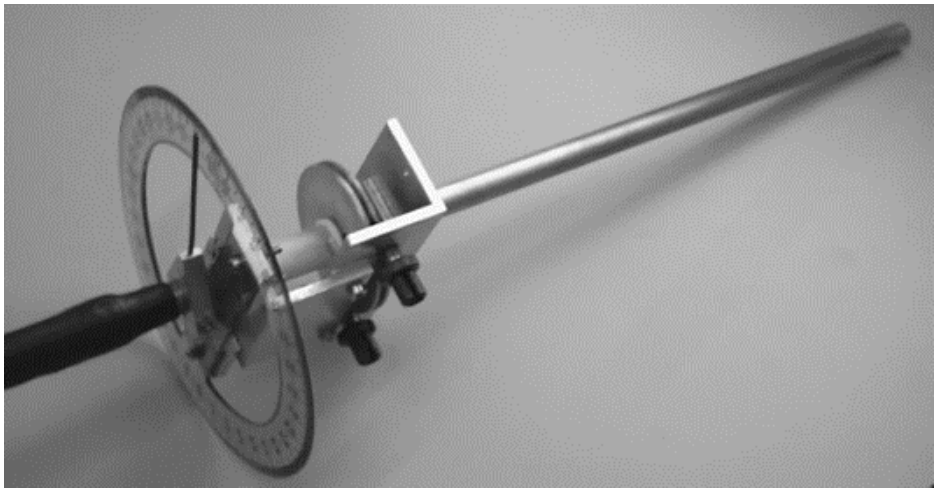

Fig. 1. Prototype of the tracer gas injection device.

The array of sampling points along the device collects the sample, carrying out in this way a very effective integration of the tracer gas concentration. Fig. 3 shows the relative position of the two developed probes in the duct, rotated ninety degrees relative to each other for more effective integration. Additionally, the injection probe has the possibility of scanning angular movement. In this system the adjustment of the scanning angle has a maximum regulation of 45º for each one of the sides (left/right). In this probe it was adopted a system with a regulated alternative movement. The cope for this feature is an improvement in the tracer gas dispersion for low duct air velocities. A sensor was installed for the measurement of the scanning frequency. For better adjustment of the scanning angle a goniometer with a pointer, was also installed.

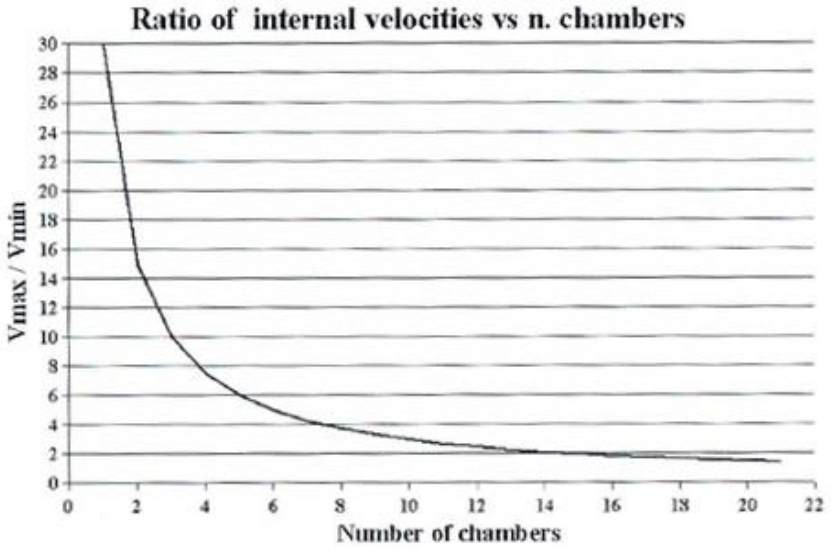

Fig. 2. Ratio of velocities versus the number of distribution chambers.

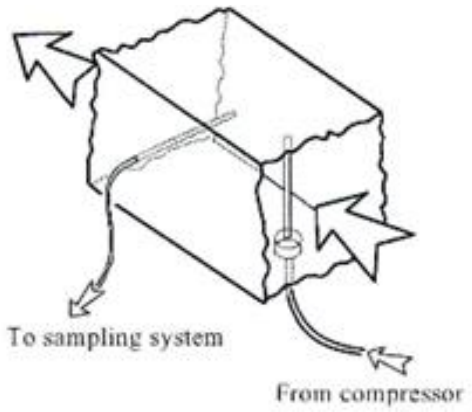

Fig. 3. Relative position of the two developed probes in the duct.

2.3. Experimental setup

The test facility consists basically in a calibrated wind tunnel allowing different airflow rates. The air movement is obtained with an axial fan with ten composite blades of adjustable pitch. The total length of the wind tunnel is 21m with a working section of 0.3m x 0.3m and a length work of 15m. The injection device was placed at the center of the 15m length work section. The calibration of the wind tunnel was carried out with a Pitot tube, scanning the working section area with a six by six matrix for various flow rate values and using the log Tchebycheff method ISO (2000) ANSI/ASHRAE Standard 111-118 (1998). Fig. 4 represents the wind tunnel layout with its main dimensions. The tracer gas concentration was measured by using a photoacoustic multi-gas analyzer, model 1312, manufactured by INNOVA (Grieve PW, 1998). Fig. 5 shows the complete injection circuit. Tracer gas flows from the pressurized bottle to the tracer dozer trough a very sensitive low pressure regulator. One metering valve controls the mixture of the tracer with exterior carrier air. This mixture flows to the inlet of a compressor, which pressurizes the mixture to the injection probe. Sulphur hexafluoride, SF6, was the only tracer gas used in the tests. The sampling integration device was placed in different locations, from $X/Dh = 22$ to $X/Dh = 1$, in a horizontal position (90º relatively to the injection device).

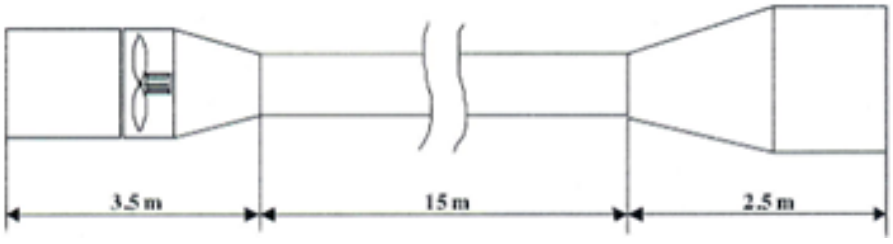

Fig. 4. Wind tunnel layout with its main dimensions.

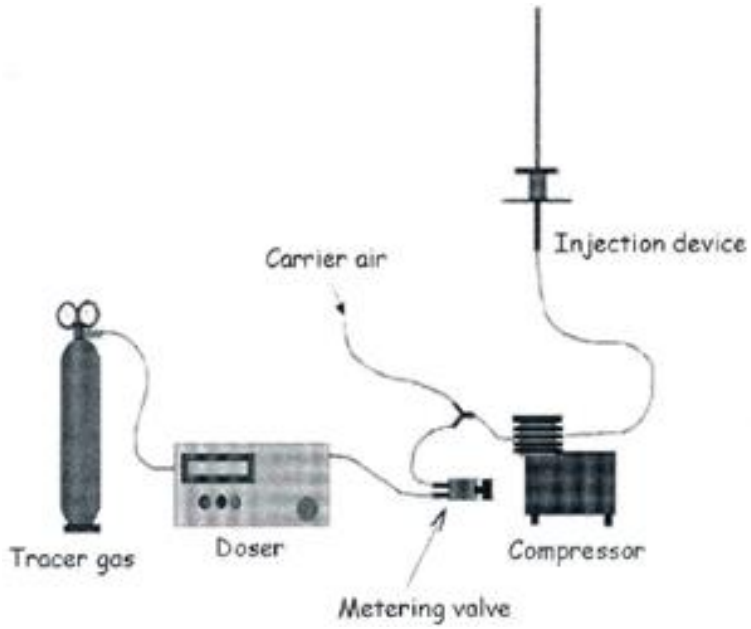

Fig. 5. Complete injection circuit.

3. Initial Tests and Results

For the evaluation of the effectiveness of the prototypes developed, some initial tests and experiments were performed by Silva (2002). The tests can be classified in three categories: measurement of airflow for different distances between in injection and sampling probes; evaluation of tracer gas concentration gradients in the wind tunnel and tests for effective contribution of the angular movement of the injection probe.

3.1. Measurement of airflow rates for different duct distances

The injection probe was placed half way of the working length of the wind tunnel (15 m as already mentioned). The objective of this initial duct length is to guarantee that the airflow is not yet completely developed (the worst conditions).

The sampling probe was placed in different positions downstream, remaining the injection probe in the central position for all the tests. Only for easy access the injection probe was mounted in vertical position and the sampling device in horizontal position for all the tests carried out. In real applications the relative position between the sampling and injection devices of ninety degrees is the unique condition. The sampling time was of 18s for all the tests and was imposed by the characteristics of the tracer gas analyzer. The multiplexed sampling system did not impose any restriction in these times and was synchronized by computer control. The test duration has the typical value of 30min. For numerical processing of the results a real time analysis of the data was carried out in order to verify the necessary conditions of permanent regime (sampling gas concentration with stabilized values).

Initially, the distance between the sampling and injection devices was of $X/Dh = 22$ following $X/Dh = 4$, $X/Dh = 2$ and $X/Dh = 1$. For each X/Dh several tests were carried out with different airflow rates. For the duct length tests of $X/Dh = 22$, a total of five tests were done for rotation speeds between 300 and 1200rpm, corresponding respectively to airflows of 0.288 m^3/s up to 1.308 m^3/s and average air velocities of 3.20m/s up to 14.53 m/s. The results are shown in Table 1 and in Fig. 6.

Table 1. Table for device at distance $X/Dh = 22$.

Airflow w/Pitot Tube	Device $X/Dh = 22$	Difference (%)
0.288	0.300	4.10
0.399	0.421	6.98
0.508	0.538	5.92
0.619	0.634	2.44
1.308	1.288	1.53

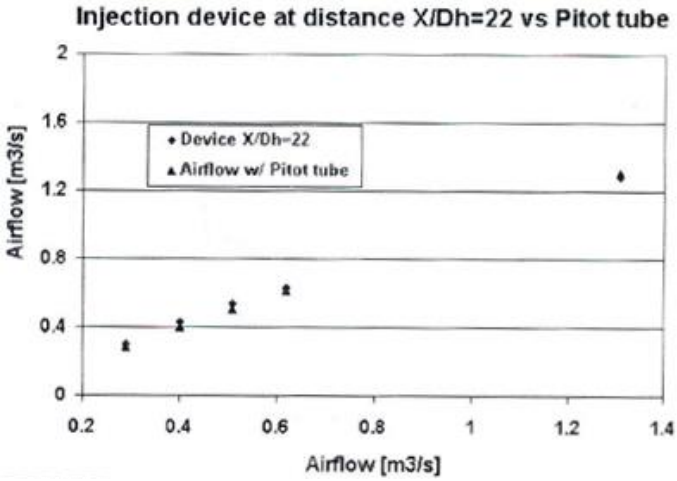

Fig. 6. Device at distance $X/Dh = 22$.

For the duct length of $X/Dh = 4$ and $X/Dh = 2$, a total of ten tests for each one were done again in the same range of fun rotation speeds of the previous tests. The results are shown in Table 2 and Fig. 7 for the first situation and in Table 3 and Fig. 8 for the second situation.

Table 2. Table for device at distance $X/Dh = 4$.

Airflow w/Pitot Tube	Device $X/Dh = 4$	Difference (%)
0.288	0.378	31.17
0.399	0.470	17.75
0.508	0.546	7.50
0.619	0.650	5.03
0.733	0.755	3.04
0.849	0.856	0.85
0.962	0.940	2.32
1.080	1.072	0.76
1.195	1.185	0.80
1.308	1.310	0.15

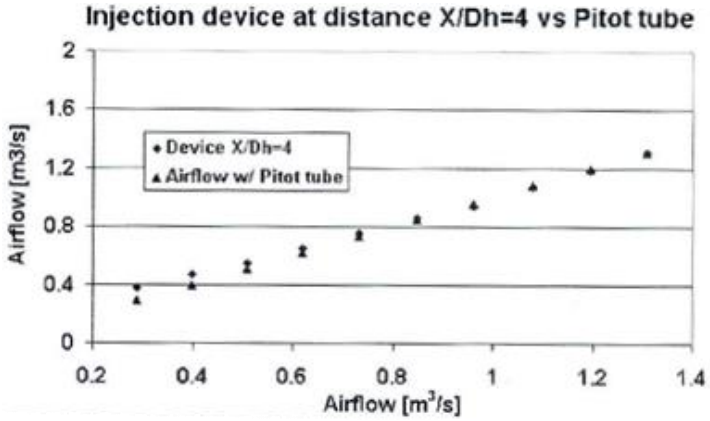

Fig. 7. Device at distance $X/Dh = 4$.

Table 3. Table for device at distance $X/Dh = 2$.

Airflow w/Pitot Tube	Device $X/Dh = 2$	Device $X/Dh = 2$ correction	Prevision	Difference (%)
0.288	0.342	0.288	0.281	0.15
0.399	0.465	0.391	0.391	1.98
0.508	0.581	0.488	0.510	3.86
0.619	0.727	0.615	0.623	0.57
0.733	0.879	0.748	0.738	2.06
0.849	t.026	0.876	0.851	3.20
0.962	1. 145	0.976	0.964	1.42
1.080	1.289	1.101	1.080	1.88
1.195	1.367	1.160	1.192	2.93
1.308	1.526	1.300	1.305	0.64

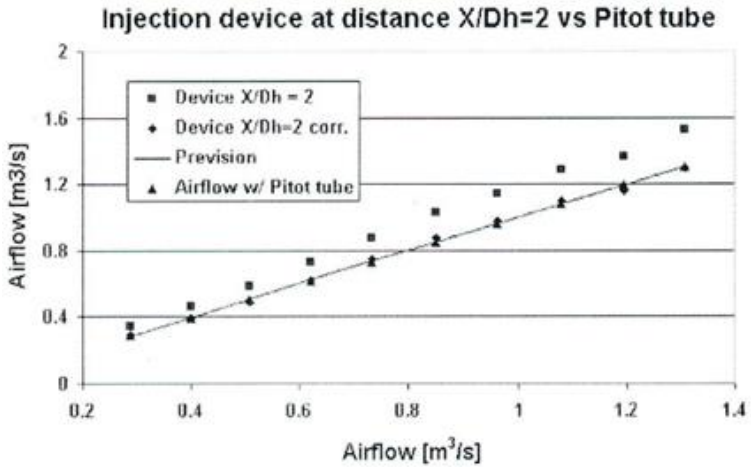

Fig. 8. Device at distance $X/Dh = 2$.

The third column of Table 3 represents the airflow rates calculated with the tracer gas technique and corrected through the expression presented by Eq. (1).

$$Q_{xDhcorr} = Q_{xDh} - Corr_{xDh} \,. \quad (1)$$

Finally, the $X/Dh = 1$ tests have been carried through a total of ten tests, for the same range of fan rotation speeds. The results are shown in Table 4 and in Fig. 9. As in Table 3, the third column of Table 4 represents the airflow rates calculated with the tracer gas technique and corrected through the expression presented by Eq. (1).

The tracer gas duct dispersion for very short distances is particularly difficult. The tests for distances $X/Dh = 2$ and $X/Dh = 1$ had the aim to evaluate the behavior of the injector device in this extreme conditions. In real practical situations of airflow measurement in HVAC systems, with much frequency, these short distances are the only hypothesis to measure. So, it is of great interest to have correlations or semi-empiric relations to apply to the measured values for this particular measurement situation. For these shortest distances, an effect of bypass is clear patent in the results. As can be seen mainly in Figs. 8 and 9 the airflow calculated with the tracer gas technique and with the Pitot tube (the reference) diverges with the airflow increase. This effect is due to the incomplete mixture of the tracer gas with the airflow for very small distances. Despite this, the obtained airflow rates with this new injection device are smooth, representing a potential for posterior use of some form of correlation.

It is now necessary to carry out more tests and deep statistical analyses in order to obtain a semi-empirical expression that can correlate the measured values with the real ones. To overcome the effect of bypass due to the incomplete tracer dilution, it was considered in the present work a simplified method of correction, for duct distances of $X/Dh = 1$ and $X/Dh = 2$. These corrections had been done taking as reference the airflow rates measured with Pitot tube. The expression proposed for calculation of the correction, has the form of a function of the airflow, with the generic form already shown in Eq. (1).

Table 4. Table for device at distance $X/Dh = 1$.

Airflow w/Pitot Tube	Device $X/Dh = 1$	Device $X/Dh = 1$ correction	Prevision	Difference (%)
0.288	0.311	0.303	0.281	5.00
0.399	0.471	0.413	0.397	3.52
0.508	0.592	0.486	0.510	4.26
0.619	0.735	0.581	0.623	6.07
0.733	0.945	0.742	0.739	1.25
0.849	1.104	0.853	0.851	0.49
0.962	1.286	0.987	0.964	2.57
1.080	1.441	1.093	1.080	1.16
1.195	1.574	1.178	1.192	1.41
1.308	1.752	1.308	1.305	0.01

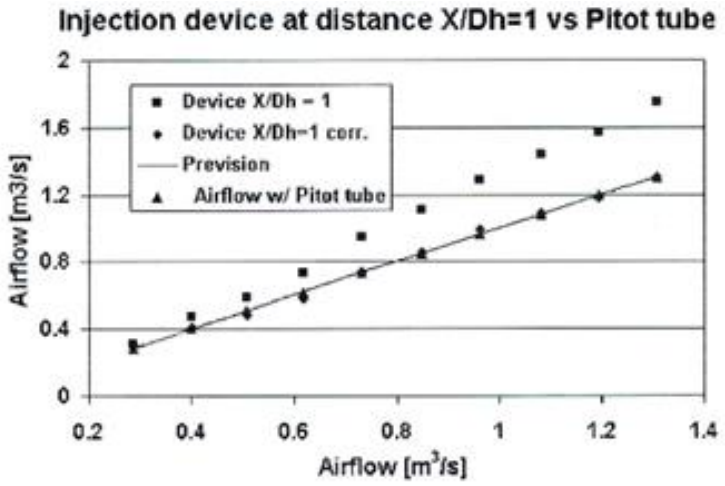

Fig. 9. Device at distance $X/Dh = 1$.

The correction for *X/Dh=Z*, $Corr_{2Dh}$, have the following form, Eq. (2):

$$Corr_{2Dh} = 1.44^{-1} \cdot Q_{2Dh} + 5.93^{-3} \,. \quad (2)$$

For the duct length of $X/Dh = 1$, $Corr_{1Dh}$ can be expressed as, Eq. (3):

$$Corr_{1Dh} = 2.998^{-1} \cdot Q_{1Dh} + 7.82^{-2} \,. \quad (3)$$

The standard deviation for the corrected airflow values, are 1.8% for $X/Dh = 2$, and 2.57% for $X/Dh = 1$. These standard deviations are acceptable, taking in account the difficulty in tracer gas dispersion for so short duct distances. For $X/Dh = 4$ tests it can be seen that there is a good agreement between the Pitot tube and tracer measurements except for low airflow rates. This may be due to the fact that at low airflow rates the turbulence is not still high enough which turns difficult the tracer mixing process. The turbulence phenomenon is characterized by transversal air a movement that enables the dispersion of the tracer gas. So, the observed deviation of the experimental curve is due to a lower turbulence in lower speeds and consequently a more difficult mixing process. Comparing these results with the work of other authors, it was reported that the minimum distance obtained for a good tracer mixture is of $X/Dh = 7$ (Cheong, 1994). This distance is almost double of the distance $X/Dh = 4$ obtained with this new injection device being able to conclude that the results for $X/Dh = 4$ are acceptable in spite of the standard deviation of 6.94% for all the airflow range studied. In the tests for distance $X/Dh = 22$ the standard deviation found for all the range of airflows was 4.19%. This value is similar to the one found for $X/Dh = 4$ being then possible to conclude then that are not significant improvements in tracer gas dispersion for $X/Dh > 4$. This distance in measurements of HVAC systems have a great importance. Usually in real systems the available duct lengths for measurement are very short.

3.2. Tests for evaluation of the injector angular movement

The evaluation tests of gradients of concentration and the effect of the rotation of the injection probe (movement of angular scanning) had been carried through the distance $X/Dh = 3$. This distance was selected because it was intended to evaluate the gradients in the initial tracer gas dispersion phase concluding then on the potential of tracer gas dispersion in very short duct lengths. The existence of orifices in the duct wall for measured distances of $X/Dh = 4$ and $X/Dh = 2$ used in the previous tests for the measurements of airflow explains the choice of the distance $X/Dh = 3$. The aim was to measure the profiles of concentration and the effect of the rotation of the injection device (scanning movement), simultaneously. Three very narrow aperture sampling probes had been installed in the upper face of the duct with similar vertical position of the injector device. These special probes have a similar Pitot tube shape, with 4 mm diameter, working in depression (air sample).

One of the sampling probes was installed in the axle of the duct, another one 50 mm away of the wall duct, and the remaining one at half these two distances. The depth of the three probes was exactly the mean section of the duct. To be able to evaluate the effect of the rotation of the injection device (movement of angular scanning) two different airflows had been compared. For high airflows, the penetration of the sonic jets is less effective. Consequently, the movement of angular scanning is not so effective too. So, this is the worst condition and then the necessity to study this condition. Conditioned by the total monitoring time of the tracer gas analyzer, only one half of the duct was monitored in the tests. In Figs. 10 and 11 that represents respectively the concentration profiles for an airflow of 0.619 m³/s and of 0.962m³/s, the remaining section is represented by symmetry for better understanding. The scanning frequency has a value of 10Hz (10 scanning/s) and was constant for the tests. The graph compares two distinct situations: the injector device with an angular scanning movement of approximately 90º aperture (45º for the left and 45º for the right against the flow) and a static injection in counter current (0º).

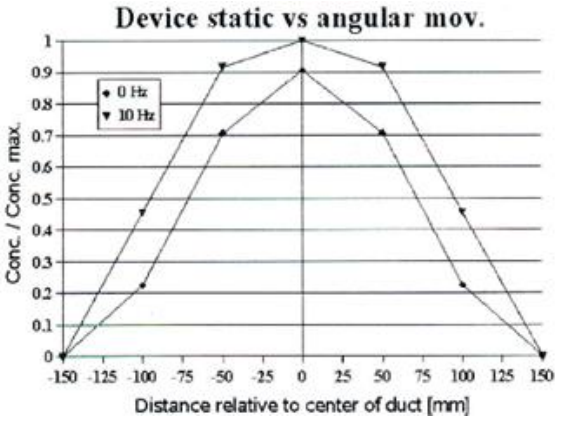

Fig. 10. Concentration profiles for an airflow 0.619 m³/s.

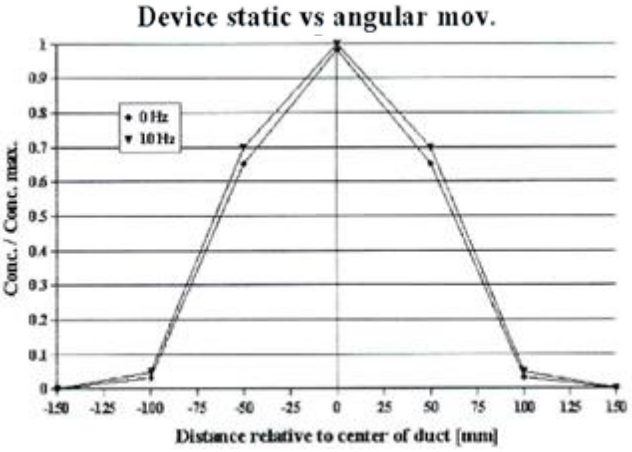

Fig. 11. Concentration profiles for an airflow 0.962 m³/s.

Each value represented in the graphs is the average of a series of values obtained from the tracer gas concentration monitoring. The number of measurements varies slightly with the duration of each test but was never lower than twenty measurements. One conclusion that can be withdrawn from these graphs is that the effect of the rotation movement is less noticed for higher airflows as already mentioned. Regarding these results, it is than possible to conclude, that there is no advantage in the movement of scanning for higher airflows. In the situation of application of this technique to the measurement of airflows in HVAC systems where the air speed usually does not exceed the 10m/s, the possibility of scanning movement has some future potential interest.

4. Smoke Tests

The smoke tests were carried out through a transparent section of the wind tunnel. A smoke generator made by Günther Schaidt Safex Chemie, model FlowMarker (2001) was used. The smoke used has a density close to the air, Fig. 12 represents a photograph of a group of parallel free jets, produced by this new injection device (12.5 mm diameter). The outlet of the smoke generator is behind the body of the injection device. The smoke is sucked by the low pressure created near the base of the jets (zone of strong depression), and the smoke is accelerated by the high speed of the jets. The diffuse aspect of the smoke is due to high velocity of it. The special flash used with the camera, with a high illumination speed, was not capable of freezing the smoke movement.

Fig. 13 represent the flow visualization at a main flow velocity of 3.2 m/s seen from an upper position. The dispersion effect of the counter current jets is patent in this figure. Viegas (1981), studied the parallel air jets interaction and concluded that for $X/s > 50$ there is an interaction of the jets and they behave like they were emitted from only a single source. In the present work $s = 2.5$ mm resulting in a distance of $X = 125$ mm, for the above condition. This distance is lower than $X/Dh = 1$ (300 mm), condition that in theory satisfies the main objective of tracer gas dispersion in very short distances.

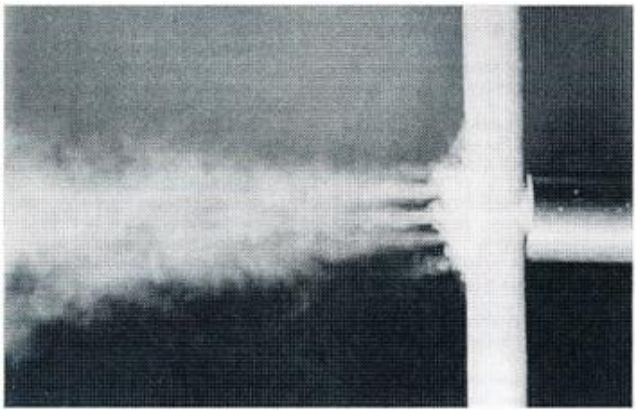

Fig. 12. Photograph of a group of parallel free jets.

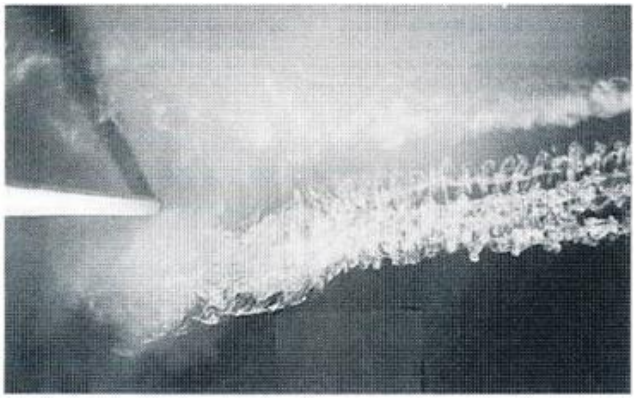

Fig. 13. Flow visualization - main flow velocity of 3.2 m/s seen from an upper position.

5. Conclusions

In this work, it is presented a new prototype device for injection and sampling of tracer gas for measurement of duct airflows. The devices after tests carried out in a wind tunnel showed that they are able to measure accurately airflows for very small distances between the injection and sampling of tracer gas. In this study, four different distances were considered with practical interest in applications of HVAC systems. The airflows measured with the tracer gas technique using those new devices showed a good correlation with the ones obtained with a reference Pitot tube. For very short distances of $X/Dh = 1$ and $X/Dh = 2$, simplified correction expressions are necessary. These devices are easy to apply in field measurements, producing accurate airflow values.

References

ANSY/ASHRAE Standard 111-118 (1988). Practices for measurement, testing, adjusting and ba1ancing of building heating, ventilation, air conditioning and refrigeration systems, American Society of Heating, Refrigerating and Air Conditioning Engineers, Atlanta.

Carter G (1998). Tracer Gas Air Flow Rate Measurement as an Alternative to Pitot Tube Traverse in Commercial Building Ventilation Systems, *M.Sc. thesis*, UC Berkeley, Berkeley.

Center for Environmental Design Research (2003). College of Environmental Design, UC Berkeley, Berkeley.

Cheong K (1994). The Application of Tracer-Gas Techniques for Measuring Airflow in HVAC Systems. *PhD thesis*, School of the Built Environment, University of Nottingham, Nottingham, UK.

Cheong KW (1996). Tracer gas technology for airflow measurements in HVAC systems. *International Journal of Energy Research,* 20(12), 1081-1094.

Cheong KW (2001). Airflow measurements for balancing of air distribution system-tracer-gas technique as an alternative. *Building and Environment*, 36.

Cheong KW, Chong KY (2000). Development and application of an indoor air quality audit to air-conditioned building in Singapore. *Building and Environment*.

Cheong KW, Rifat SB (1992). Application of tracer-gas techniques for measurement of friction-factors of rectangular ducts. *Air Infiltration Review*, 13.

FlowMarker lnstructions Manual (2001). Günther Schaidt Safex Chemie.

Grieve PW (1989). Measuring Ventilation Using Tracer-gases, Brüel and Kjaer.

Indoor Climate and Ventilation (2001). Measurement of main air flows using tracer gases. *Dantec Dynamics Application Note*.

INNOVA Air Tech Instruments (1998). Monitor Multigaz Type l3l2 Instructions.

International Standard ISO 3966. Mesure du Débit des Fluides dans les Conduites Fermées-Méthode d' Exploration du Champs des Vitesses au moyen de Tubes de Pitot Doubles", International Standards Organisation, Genève.

International Standard ISO 4053/I-1977 (F). Mesurage de Débits de Gaz dans les Conduites - Méthodes par.

McWilliams (2003). Review of airflow measurement techniques, energy performance of buildings group, Environmental Energy Technologies Division, Lawrence Berkeley National Laboratory, Berkeley.

Rifat SB (1990). Comparison of tracer gas techniques for measuring airflow in ducts. *Journal of the Institute of Energy,* 63.

Rifat SB, Cheong KW (1993). Tracer-gas techniques for design and commissioning of HVAC system. *Proceedings of First International Conference on Environmental Engineering*, Leicester, UK.

Rifat SB, Lee SF (1990). Turbulent flow in duct: Measurement by a tracer gas technique. *Building Services Engineering Research and Technology,* 11.

Silva AR (2002). Medição de Caudais de Ar pelo Método de Emissão Constante com Desenvolvimento de Sonda para Gás Traçador. *Ph.D. Thesis*, INETI, Lisboa.

Traceurs-Partie I: Généralités, International Standards Organisation, Genève.

Viegas DX (1981). Uma Técnica de Erosão Aplicada ao Estudo da Interação de Jatos Turbulentos com uma Superfície Plana. *Ph.D. Thesis*. Faculdade de Ciências e Tecnologia da Universidade de Coimbra, Portugal.

Challenge Journal of Structural Mechanics

Universal size effect of concrete specimens and effect of notch depth

Sıddık Şener [a,*], Kadir Can Şener [b]

[a] *Department of Civil Engineering, İstanbul Bilgi University, 34060 İstanbul, Turkey*
[b] *Department of Civil Engineering, Purdue University, Indiana 47907-2045, USA*

ABSTRACT

The universal size effect law of concrete is a law that describes the dependence of nominal strength of specimens or structure on both its size and the crack (or notch) length, over the entire of interest, and exhibits the correct small and large size asymptotic properties as required. The main difficulty has been the transition of crack length from 0, in which case the size effect mode is Type 1, to deep cracks (or notches), in which case the size effect mode is Type 2 and fundamentally different from Type 1. The current study is based on recently obtained comprehensive fracture test data from three-point bending beams tested under identical conditions. In this test, the experimental program consisted of 80 three-point bend beams with 4 different depths 40, 93, 215 and 500mm, corresponding to a size range of 1:12.5. Five different relative notch lengths, a/D = 0, 0.02, 0.075, 0.15, 0.30 were cut into the beams. A total of 20 different geometries (family of beams) were tested. The present paper will use these data to analyze the effects of size, crack length. This paper presents a studying to improve the existing universal size effect law, named by Bazant, using the experimentally obtained beam strengths for various different specimen sizes and all notch depths. The updated universal size effect law is shown to fit the comprehensive data quite well.

ARTICLE INFO

Article history:
Received 25 December 2016
Accepted 24 February 2017

Keywords:
Concrete fracture
Scaling of strength
Fracture testing
Notch-depth effect
Flexural testing

1. Introduction

The proceeding conference articles and paper (Şener at al., 2014a; Çağlar and Şener, 2015; Çağlar and Şener, 2016; Şener and Şener, 2016) presented an introduction to the problem and reported comprehensive test data for fracture of concrete specimens. The experimental program, also described in (Şener et al., 2014b), consisted of 80 three-point bend beams with 4 different depths 40, 93, 215 and 500mm, corresponding to a size range of 1:12.5. Five different relative notch lengths, a/D = 0, 0.02, 0.075, 0.15, 0.30 were cut into the beams. A total of 20 different geometries (family of beams) were tested. The present paper will use these data to analyze the effects of size, crack length. A special case of this law is a formula for the effect of notch or crack depth at fixed specimen size, which overcomes the limitations of a recently proposed empirical formula by Duan et al. (2003, 2006).

The Scientific and Technological Research Council of Turkey (TUBITAK) provided funding to carry out comprehensive fracture tests of beam specimens made from the almost the same age and same concrete mix to investigate the influence of size and notch length on specimen strength.

2. Reviews of Size Effect and Crack Length Effect

The nominal strength of geometrically similar structures, defined with Eq. (1) is

$$\sigma_N = c_N \frac{P_u}{bD}, \tag{1}$$

independent of structure size D (P = maximum load; b = structure width; and c_N = dimensionless constant chosen for convenience). Size effect is defined as any dependence

* *Corresponding author*. Tel.: +90-212-3117376 ; Fax: +90-212-4278270 ; E-mail address: siddik.sener@bilgi.edu.tr (S. Şener)
ISSN: 2149-8024 / DOI: https://doi.org/10.20528/cjsmec.2017.02.003

of σ_N on D, which is a phenomenon typical in fracture or damage mechanics.

According to linear elastic fracture mechanics (LEFM) theory, which applies to homogeneous perfectly brittle materials, and for geometrically similar structures with similar cracks, $\sigma_N \propto D^{-1/2}$, which is the strongest possible size effect. For quasi-brittle materials such as concrete, one can distinguish two simple types of size effect as shown in Eq. (2).

$$\sigma_N = \frac{Bf_t}{\sqrt{1+D/D_0}}. \tag{2}$$

Here B and the transitional structure size D_0 are empirical parameters to be identified by data fitting and f_t is tensile strength of concrete introduced for convenience. Eq. (2) was derived (Bazant, 1984) by simple energy release analysis and later by several different approaches such as by asymptotic matching based of the asymptotic power scaling laws for very large and very small D (Bazant and Planas, 1998). In the standard size effect plot of log σ_N versus log D, Eq. (2) gives a smooth transition from a horizontal asymptote to an inclined asymptote of slope -1/2 (Fig. 1).

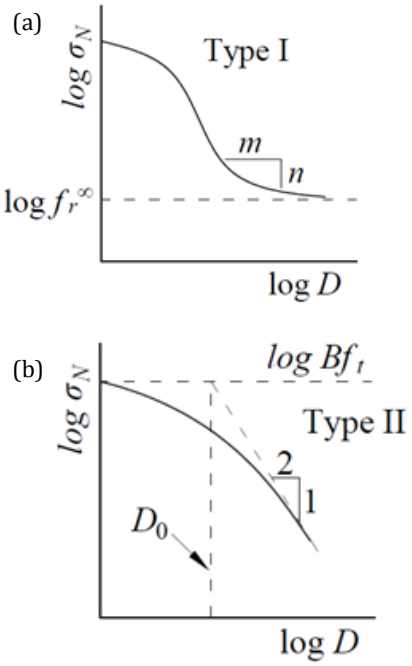

Fig. 1. Dependence of σ_N on structure size D of beams with (a) no notched and (b) deep notch.

In Eq. (2),

$$Bf_t = \sqrt{\frac{E'G_f}{g_0'c_f}}, \quad D_0 = \frac{c_f g_0'}{g_0}, \tag{3}$$

where $g_0 = g(\alpha_0)$; $g_0' = g'(\alpha_0)$; $\alpha = a/D$ = relative crack length; $\alpha_0 = a_0/D$ = initial value of α; $g(\alpha) = k^2(\alpha)$ = dimensionless energy release rate function $g(\alpha)$ of LEFM; $k(\alpha) = b\sqrt{(DK_I/P)}$ where K_I = stress intensity factor, P = load; $g'(\alpha) = dg(\alpha)/d\alpha$, $E' = E$ = Young's modulus for plane stress and $E' = E/(1-\nu^2)$ for plane strain (where ν = Poisson ratio), G_f=initial fracture energy = area under the initial tangent of the cohesive softening stress-separation curve; c_f = characteristic length, which represents about a half of the Fracture Process Zone (FPZ) length. Eq. (2) may be rewritten as shown in Eq. (4).

$$\sigma_N = \sqrt{\frac{E'G_f}{g_0 D + g_0' c_f}}. \tag{4}$$

Because function $g(\alpha)$ or $k(\alpha)$ embodies information on the effects of crack length and structure geometry, Eq. (4) is actually a size effect law for Type 2 failures.

The Type 1 size effect, σ_N approaches, for large D, a constant value (a horizontal asymptote in the size effect plot), since the Weibull statistical size effect (Weibull, 1939) is unimportant. For three point bend beams, it is indeed unimportant. Because the zone of high stresses is rather concentrated, even do not exist along a notch. This prevents the critical crack from forming at widely different locations of different random local strength (for the same reason, the statistical size effect is negligible in Type 2 failures also).

The large size asymptote for Type 1 size effect is, in the log-log plot, a downward inclined straight line of a slope $-n/m$, which is much milder than the slope of -1/2 for LEFM (Weibull, 1939) (Fig.1); here m = Weibull modulus and n = number of spatial dimensions of fracture scaling (n = 2 for the present tests). The small size asymptote is also a horizontal line and, for medium sizes, the size effect is a transition between these two asymptotes. In absence of the statistical size effect, Eq. (5) was used by Hoover and Bazant (2014).

$$\sigma_N = f_r^\infty \left(1 + \frac{rD_b}{D+l_p}\right)^{1/r}. \tag{5}$$

Here f_r^∞, D_b, l_p, and r are empirical constants to be determined from tests; f_r^∞=nominal strength for very large structures, assuming no statistical size effect (in the special case of very large beams, f_r^∞ represents the flexural strength, also called the modulus of rupture); and D_b = depth of the boundary layer of cracking (roughly equal to the FPZ size). In all previous works, D = same characteristic structure size as used for the Type 2 size effect (Eq. (4)). Furthermore, l_p = material characteristic length, which is related to the maximum aggregate size d_a. If the structure is larger than $10l_p$, one can set $l_p \approx 0$, which corresponds to the original formulation of the Type I law.

It was further shown that the Type 1 and 2 Size Effect Laws (SELs) satisfy the large-size and small size asymptotic properties of the cohesive crack model applied to Type 1 and 2 failures. Furthermore, it was experimentally confirmed that, within the range of inevitable experimental scatter, the SEL of Type 2 gives about the same values of fracture energy G_f when applied to notched fracture specimens (e.g., compact compression test (Abusiaf et al., 1996; Barr et al., 1998), torsional test (Abusiaf et al., 1997)).

3. Application of Universal Size Effect Law by Fracture Tests

To calibrate the deterministic Universal Size Effect Law (USEL), the mean of data was computed separately for each family of identical specimens from comprehensive fracture tests (Şener et al., 2014a; 2014b), Çağlar and Şener 2015). The surface of the optimized USEL is plotted in Fig. 2. In this Fig. 2 size effect curves were given for only $\alpha = 0$, 0.15 and 0.3. Transition from these curves for calibrating USEL is just used with smooth curves. The studies on these transition curves are still on going.

In particular, the fracture parameters G_f and c_f should not be influenced by the data for beams with no notches (Type I data) or shallow notches and f_r^{∞}, D_b, l_p and r should not be influenced by the data for deep notches. Therefore, these parameters were determined first by separate fitting of specimens with deep notches ($\alpha = 0.30$ or 0.15) and specimens with shallow or no notches ($\alpha = 0$). Only the nonstatistical USEL (Bazant and Yu, 2009) in Eq. (6) was considered. Nonlinear fitting of the Type I, SEL (Eq. (5)) to the notchless ($\alpha = 0$) beams gave (Şener et al., 2014a, b) values in Eq. (6) with coefficient of variation of fit 9.4%.

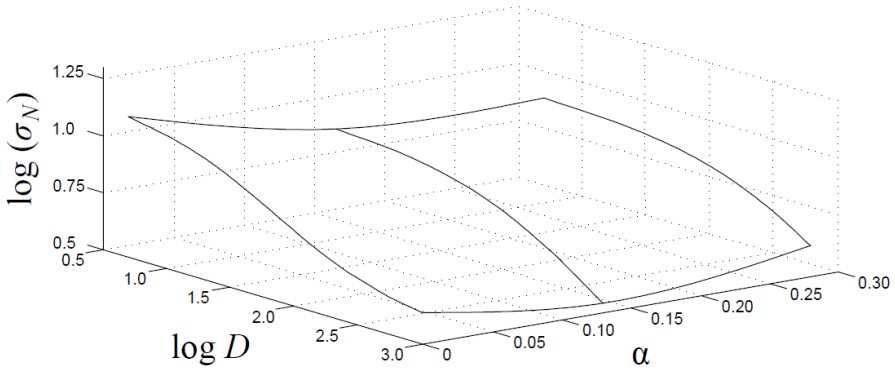

Fig. 2. Entire Universal Size Effect law surface.

$$D_b = 90\ mm,\ l_p = 50\ mm,\ f_r^{\infty} = 4\ MPa,\ r = 0.52\ . \quad (6)$$

These values are different from than the studies by Hoover and Bazant's (2014) D_b=73.2 mm, l_p=126.6 mm, f_r^{∞} =5.27 MPa. The difference between some of the parameters was in the order of two for especially l_p value. The size range 1:12.5 was large enough to identify all the fracture parameters in Eq. (5). The USEL can be drawn for a fixed α, which gives a size effect plot of log(σ_N) versus log D (Fig. 2).

In Fig. 3, this plot is created and compared with the data from Şener et al. (2014a, 2014b). The results obtained from the tests for Type II size effect (Eq. 2) was used for deep (α=0.3) and big (α=0.15) notches are shown at the Figs. 3(a, b). For the crack initiation specimens were fitted using Eq. (5), and the resulting constants were calculated. The calculated constants are given in Table 1 for the shallow notch (Fig. 3(d)) and notchless beams (Fig. 3(e)). Type I parameters, which are presented in parenthesis in Table 1 were compared with Bazant's (Hoover and Bazant, 2014) results. The parameters obtained from the results of shallow notch specimens were not compared with Bazant's results, because of insufficient data in their work for α=0.02. But Type I size effect parameters for notchless and shallow notch specimens obtained from this study were consistent between the two test programs.

In Fig. 3, for α=0.3 and 0.15, Type II (Figs. 3(a, b)) size effect was used, for unnotched specimen α=0, Type I (Fig. 3(e, f)) size effect was used. For the medium size notched (α=0.075) beams, the failure stress was in between the Type I and Type II curves, so these curves are not shown in the figure (Fig. 3(c)).

Table 1. Type I size effect coefficients.

α	D_b (mm)	l_p (mm)	f_r^{∞} (MPa)	r
0	90	50	4	0.52
(0)	(73.2)	(126.6)	(5.27)	(0.52)*
0.02	110	66	3.2	0.52

*Parameters inside parenthesis are Bazant's (Hoover and Bazant, 2014) values.

4. Comparison with Duan-Hu's Boundary Effect Model

The analysis of the test results were performed using Bazant's Type II size effect formulas and Type I. There are many widely accepted and practical size effect evaluation approaches such as; multifractal scaling law of Carpinteri (Carpinteri et al., 1995), asymptotic analysis of size effect of Karihaloo (Karihaloo et al., 2003), and boundary effect model of Hu and Duan (Duan et al., 2003, 2006). The size effect model of Hu and Duan is a boundary effect model, which was recently developed, by scaling of quasi-brittle size effect on strength of finite sized specimens. The test results were also analyzed using Hu and Duan's approach for comparison with Type I size effect of specimens with α=0. The nominal strength (σ_N) formula of Hu and Duan which accounts for size effect in concrete is given in Eq. (7) for un-notched specimens.

$$\sigma_N = \sigma_o(1 + B_1 D)^{-0.5}\ , \quad (7)$$

where σ_0 is the maximum tensile stress in the ligament based on a linear stress distribution over the ligament based on three-point bend specimens and B_1 is a constant. σ_0 and B_1 can be obtaining from linear regression analysis. Eq. (7) is mathematically similar to the Type II size effect formula given in Eq. (2).

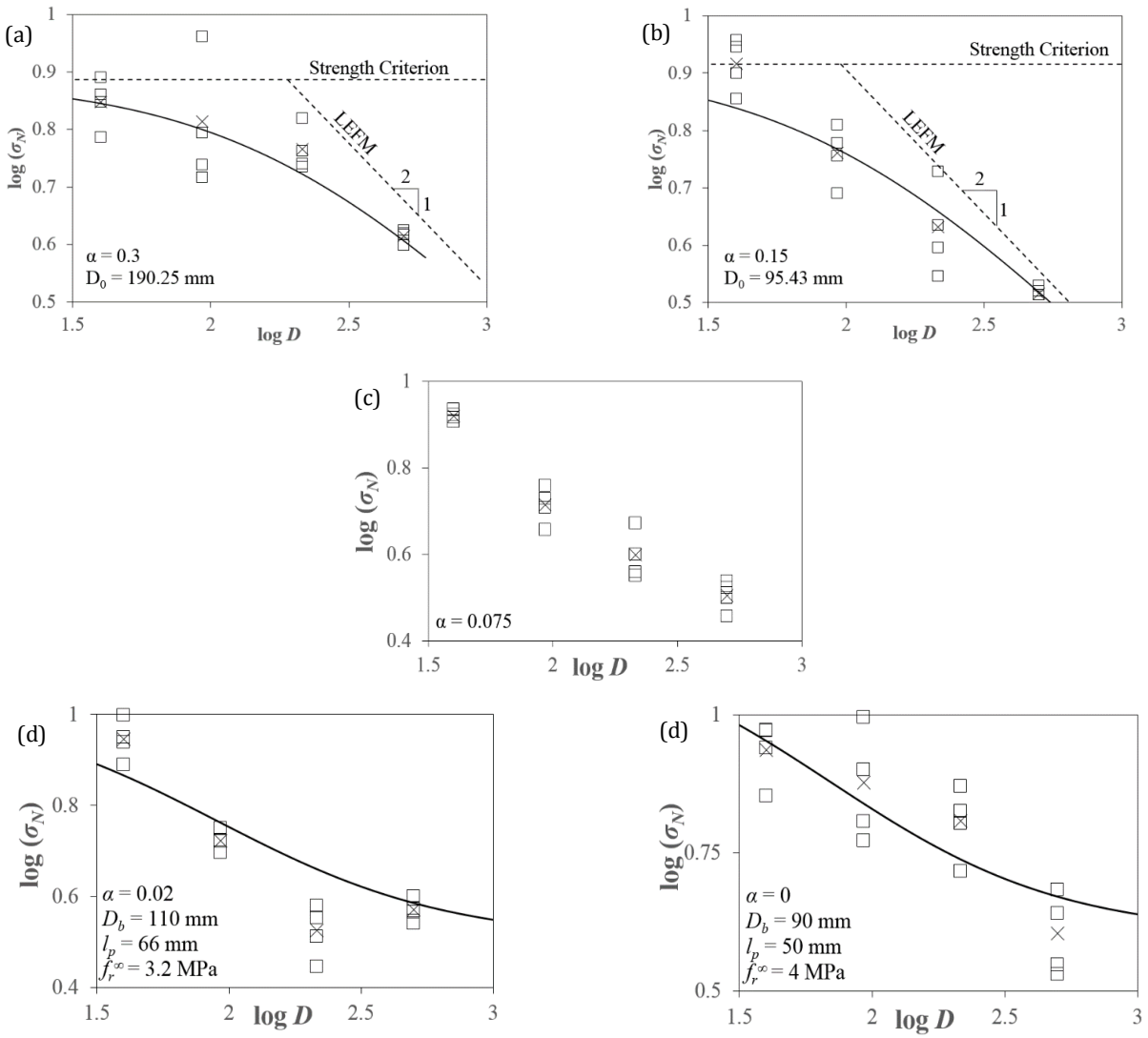

Fig. 3. Effect of structure size on the nominal strength of the data from Şener et al. (2014a).

The comparison of size effect plots of Type I and Duan's model are given in Fig. 4 for α=0. The plots indicate that Type I size effect and Duan's boundary effect model differs significantly for members' smaller depth. In the Type I (solid line) Eq. (2) the parameters were taken from Table 1 for α=0, for Duan's (broken line) Eq. (7) σ_0= 11.62 MPa, B_1= 0.0135 values were used.

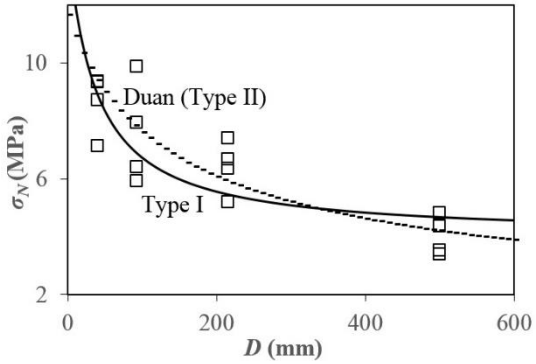

Fig. 4. Size effect plots of test results overlaid with Type I and Duan's size effect model for α=0.

5. Conclusions

- The Type 2 size effect in specimens with deep notches or cracks does not give a correct transition to of Type 1 in specimens with no notch or crack.
- The size effect data from deeply notched specimens (α=0.3 and 0.15), and parameters f_r^{∞}, D_b, l_p, and r were determined separately by fitting only the size effect data for unnotched specimens (α=0).
- USEL fits the measured nominal strength quite well.
- Both Type I and Type II size effect were observed in this study and confirmed the need to be account for size effect in design codes.
- The comparison of Type I and Duan's boundary effect formulas (Type II) exhibit difference for members with small depth for α=0.

Acknowledgements

Financial support from the Scientific and Technological Research Council of Turkey (TUBITAK) was provided through Grant No.111M374 from the Gazi University and Istanbul Bilgi University, is gratefully appreciated.

References

Abusiaf HF, Barr BIG, Şener S (1997). Application of the Torsional Damage Test in High Strength Concrete. *Fourth International Conference on Civil Engineering*, Tehran, Iran, 355-362.

Abusiaf HF, Şener S, Barr BIG (1996). Size effect in eccentrically loaded compact specimens. *Concrete Technology for Developing Countries, Fourth International Conference*, Eastern Mediterranean University, North Cyprus, 631-639.

Barr BIG, Abusiaf HF, Şener S (1998). Size effect and fracture energy studies using compact compression specimens, *RILEM, Materials and Construction,* 31(1), 36-41.

Bazant ZP (1984). Size effect in blunt fracture: Concrete, rock, metal, *Journal of Engineering Mechanics, ASCE*, 110, 518-535.

Bazant ZP, Planas J (1998). *Fracture and Size Effect in Concrete and Other Quasibrittle Materials*. CRC Press, Boca Raton, FL.

Bazant ZP, Yu Q (2009). Universal Size Effect Law and effect of crack depth on quasi-brittle structure strength. *Journal of Engineering Mechanics, ASCE,* 135, 78-84.

Carpinteri A, Chiaia B, Ferro G (1995). Multifractal scaling law: an extensive application to nominal strength size effect of concrete structures. *Atti del Dipartimento di Ingegneria Strutturale*, 2(2), Politechnico de Torino, Italy.

Çağlar Y, Şener S (2015). Size effect for notched, unnotched concrete beams, *XIX. National Mechanics Conf.,* August 24-28, Trabzon, Turkey.

Çağlar Y, Şener S (2016). Size effect tests of different notch depth specimens with support rotation measurements. *Engineering Fracture Mechanics,* 157, 43-55.

Duan K, Hu X, Wittmann FH. (2003). Boundary effect on concrete fracture and non-constant fracture energy distribution. *Engineering Fracture Mechanics,* 70, 2257-2268.

Duan K, Hu X, Wittmann FH (2006). Scaling of quasi-brittle fracture boundary and size effect. *Mechanics of Materials*, 38, 128-141.

Hoover CG, Bazant ZP (2014). Universal size-shape effect law based on comprehensive concrete fracture tests. *Journal of Engineering Mechanics, ASCE,* 140, 473-479.

Karihaloo, B. L. Abdalla, H. M., Xiao (2003). Size effect in concrete beams. *Engineering Fracture Mechanics,* 70, 979-993.

Şener S, Çağlar Y, Belgin ÇM (2014a). Size effect tests for Type I and Type II, *11th International Congress on Advances in Civil Engineering,* 51, Istanbul, Turkey.

Şener S, Belgin ÇM, Çağlar Y, Hasanpour R, Topgül S, Boduroğlu VB, Negin M, Çağlar NM (2014b). Size effect tests and fracture mechanics analysis of concrete with carbon nano tubes. *Technical report for TUBITAK*, *111M374*, Istanbul, Turkey.

Şener S, Şener KC (2016). Universal size effect studies using three point beam tests, *The First European and Mediterranean Structural Engineering and Technology Conference*, and published in *Interaction between Theory and Practice in Civil Engineering and Construction*, 67-72.

Weibull W (1939). The phenomenon of rupture in solids. *Proc. R. Swedish Inst. Eng. Res.,* 153, 1-55.

Challenge Journal of Structural Mechanics

Non-linear behaviour modelling of the reinforced concrete structures by multi-layer beam elements

Mourad Khebizi [a,*], Hamza Guenfoud [b], Mohamed Guenfoud [b]

[a] *Department of Civil Engineering, Mentouri University, 25017 Constantine, Algeria*
[b] *Department of Civil Engineering, 8 Mai 1945 University of Guelma, BP.401, 24000 Guelma, Algeria*

ABSTRACT

A two-dimensional multi-layered finite elements modeling of reinforced concrete structures at non-linear behaviour under monotonic and cyclical loading is presented. The non-linearity material is characterized by several phenomena such as: the physical non-linearity of the concrete and steels materials, the behaviour of cracked concrete and the interaction effect between materials represented by the post-cracking field. These parameters are taken into consideration in this paper to examine the response of the reinforced concrete structures at the non-linear behaviour. Two examples of application are presented. The numerical results obtained, are in a very good agreement with available experimental data and other numerical models of the literature.

ARTICLE INFO

Article history:
Received 18 October 2016
Accepted 30 December 2016

Keywords:
Modelling
Reinforced concrete
Multi-layered elements
Non-linear behaviour
Unilateral model

1. Introduction

The non-linear behaviour modelling of reinforced concrete structures is an important objective for the civil engineering researchers. The response of a structure under a loading results from a strong interaction between the materials effects (local non-linearity), the structures effects (geometry, distribution of forces and stiffness, links) and the environment effect (soil-structure interaction). The local non-linearities are related particularly to the formation, the opening and reclosure of cracks, on one hand, to the link and to the behaviour of the reinforcements (plasticity of steels) on the other hand. A good description of these phenomena has to be done in order to represent the variations of the structural stiffness and to have access to the behavior until to the collapse (Khebizi and Guenfoud, 2015).

In this paper we have presented a numerical method for modelling planar reinforced concrete structure (2D) under static and cyclical loading. This method uses multi-layered beams elements of which the stiffness matrix is computed using a beam discretization according to the height in superimposed successive layers (Fig. 1). The summation of these layers allows the calculation of stiffness in a correct manner and takes into account the behaviour variations (Khebizi and Guenfoud, 2015). The Bernoulli hypothesis (section remaining plane and perpendicular to the neutral axis of the beam) confers for different layers a uniaxial behaviour. Hence, this allows as to treat the local behaviours through uniaxial laws for the concrete and steel, laws that are assigned to each layer. The calculation of inelastic efforts is carried through to an iteration method based on the initial secant stiffness.

A particular treatment is reserved for the layers including simultaneously concrete and steel (Khebizi and Guenfoud, 2015). The behaviour of the mixed layers (Fig. 1.) is homogenized by a mixing law permitting to calculate the stress layer in proportion to each material:

$$\sigma_{layer} = \left(1 - C_{a/b}\right)\sigma_{concrete} + C_{a/b}\,\sigma_{steel}\,, \qquad (1)$$

where σ_{layer} denote axial stresses in the layer, $\sigma_{concrete}$ and σ_{steel} axial stresses in the concrete and the steel respectively in the layer and $C_{a/b}$ is the ratio surface of steel within the reinforced layer. The steel-concrete adherence is supposed to be perfect (identical strain of the two materials at their frontier: $\varepsilon_{concrete} = \varepsilon_{steel}$).

* *Corresponding author*. Tel.: +213-37-215848 ; Fax: +213-37-215848 ; E-mail address: mourad_gc@yahoo.fr (M. Khebizi)
ISSN: 2149-8024 / DOI: https://doi.org/10.20528/cjsmec.2016.11.034

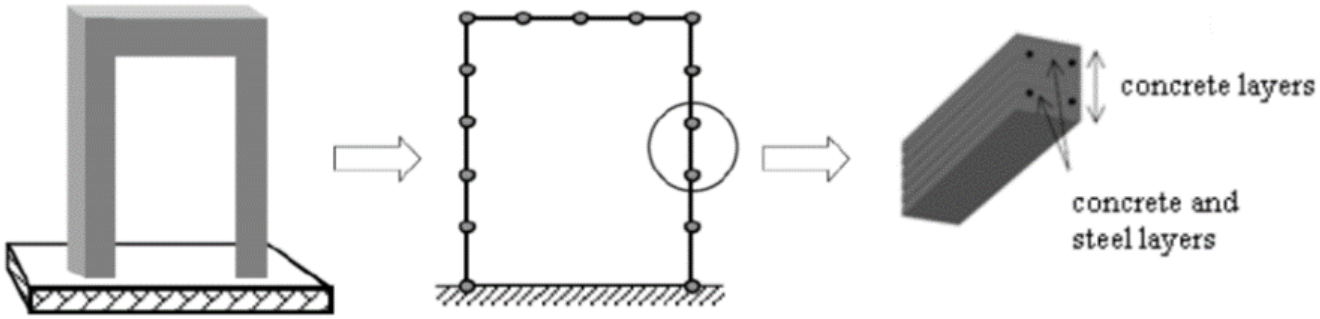

Fig. 1. Discretisation principal of reinforced concrete structures with multi-layered beam.

2. Formulation of Multi-Layered Beam Element

The elements used are beams with tow nodes, the Bernoulli hypothesis confers on the various layers a uniaxial behaviour. The relation giving the element equilibrium is obtained by the virtual work principle, expressed in terms of generalized coordinates.

$$\delta U^T F = \int_\Omega \delta\varepsilon^T \sigma dV = \int_\Omega \delta(BU)^T \sigma dV = \int_\Omega \delta U^T B^T \sigma dV \,, \quad (2)$$

where B depends on the derived shape functions.

If can be introduced a behaviour law with damage and inelastic,

$$\varepsilon = \frac{\sigma}{E(1-D)} + \varepsilon_{an}(D) \Rightarrow \sigma = E(1-D)(\varepsilon - \varepsilon_{an}) \,. \quad (3)$$

The virtual work principle takes the following form:

$$\delta U^T F = \int_\Omega \delta U^T B^T E(1-D)(\varepsilon - \varepsilon_{an}) dV$$
$$\Rightarrow F = \int_\Omega B^T E(1-D)(\varepsilon - \varepsilon_{an}) dV \,. \quad (4)$$

Eq. (4) can be rewritten in the following form:

$$F = \left[\int_\Omega B^T E(1-D) B dV\right] U - \int_\Omega B^T E(1-D)\varepsilon_{an} dV \,. \quad (5)$$

By putting:

$$\begin{cases} K = \int_\Omega B^T E(1-D) B dV \\ F = -\int_\Omega B^T E(1-D)\varepsilon_{an} dV \end{cases}, \quad (6)$$

we end up with the final system to solve:

$$F = KU + F_{an} \,. \quad (7)$$

K is the element stiffness matrix:

$$K = \int_0^l B^T k_s B dx \,. \quad (8)$$

The section stiffness matrix is expressed as follows:

$$k_s = \begin{bmatrix} k_{11} & k_{12} \\ k_{21} & k_{22} \end{bmatrix}. \quad (9)$$

$$k_{11} = \int_s E ds \quad k_{12} = k_{21} = \int_s E y ds \quad k_{22} = \int_s E y^2 ds \,. \quad (10)$$

The discretization of the cross-section in superimposed layers according to the Bernoulli hypothesis allows to be obtaining the following stiffnesses (Belmouden, 2004; Khebizi and Guenfoud, 2015; Khebzi, 2015):

$$k_{11} = \sum_{k=11}^{nlayers} E_k A_k \,,$$

$$k_{12} = k_{21} = \sum_{k=11}^{nlayers} E_k y_k A_k \,,$$

$$k_{22} = \sum_{k=11}^{nlayers} E_k y_k^2 A_k \,. \quad (11)$$

E_k, A_k and y_k are respectively the Young's modulus, the layer area and the centre position layer to the reference axis.

3. Damage Model for the Concrete (Unilateral Model)

The unilateral model (Laborderie, 2003; Kotronis, 2000; Davenne et al., 2003) is an isotropic model where two scalar damage variables, are used to describe the consequences of the evolution of the mechanical characteristics of material, the irreversible strains and the unilateral effect when the sign of the stresses changes. Considering the partition of the strain tensor as the sum of an elastic part and an inelastic part, calculated as follows:

$$\varepsilon = \varepsilon_e + \varepsilon_{an} \,, \quad (12)$$

$$\begin{cases} \varepsilon_e = \frac{\sigma^+}{E_0(1-D_1)} + \frac{\sigma^-}{E_0(1-D_2)} + \frac{V}{E_0}(\sigma - (Tr\sigma)I) \\ \varepsilon_e = \frac{\beta_1 D_1}{E_0(1-D_1)} \frac{\partial f(\sigma)}{\partial \sigma} + \frac{\beta_1 D_2}{E_0(1-D_2)} I \end{cases}, \quad (13)$$

where E_0 is the initial Young's modulus and ν the Poisson's ratio. ‹•›+ denotes the positive part of a tensor, D_1 and D_2 are scalar damage variable in tension and scalar damage variable in compression respectively (their evolution between 0 – i.e, healthy material- to 1 - i.e, broken material- is related to the local elastic energy). β_1 and β_2 are material parameters to be identified in order to describe the evolution of the inelastic strains can be described, $f(\sigma)$ is the crack closure function which cancels the inelastic strains of the tension during the recovery of stiffness and σ_f the crack closure stress:

$$\begin{cases} Tr(\sigma) \in [0, +\infty[\rightarrow \frac{\partial f(\sigma)}{\partial \sigma} = 1 \\ Tr(\sigma) \in [-\sigma_f, 0[\rightarrow \frac{\partial f(\sigma)}{\partial \sigma} = (1 + \frac{Tr(\sigma)}{\sigma_f}) = 1 \\ Tr(\sigma) \in [-\infty, -\sigma_f[\rightarrow f(\sigma) = 0.1 \end{cases}. \quad (14)$$

The evolution laws for the damage are finally written as:

$$D_i = 1 - \frac{1}{1+(A_i(Y_i - Y_{0i}))^{B_i}}, \quad (15)$$

where Y_i is the variable associated to damage (energy refund ratio, tension or compression). A_i and B_i are material constants. Y_{0i} is the damage threshold (tension or compression).

The stress-strain relation-ship and the crack closure function in the uniaxial model (Fig. 2) can be written as follows:

$$\varepsilon = \frac{\sigma^+}{E_0(1-D_1)} + \frac{\sigma^-}{E_0(1-D_2)} + \frac{\beta_1 D_1}{E_0(1-D_1)} F(\sigma) + \frac{\beta_2 D_2}{E_0(1-D_2)}, \quad (16)$$

$$\begin{cases} F(\sigma) = 1 \; if \; \sigma \geq 0 \\ F(\sigma) = 1 - \frac{\sigma}{\sigma_f} \; if \; -\sigma_f \leq \sigma \leq 0 \\ F(\sigma) = 0 \; if \; \sigma < -\sigma_f \end{cases}. \quad (17)$$

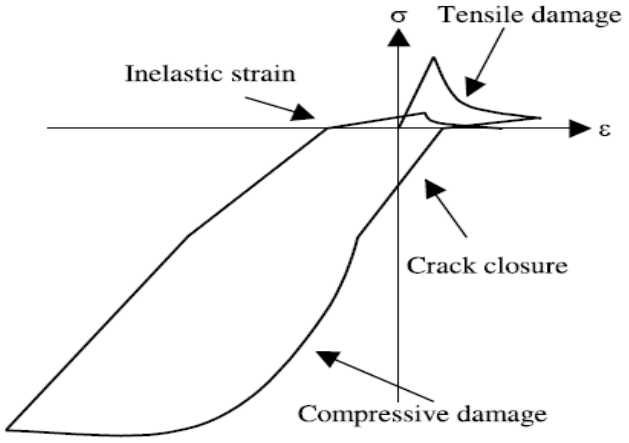

Fig. 2. Uniaxial response of the unilateral model.

4. The Behaviour of Steel

In order to describe the non-linear behaviour of reinforcement, one chooses the classical plasticity model which take into account the non-linear kinematic hardening is used.

The reinforcement has a privileged orientation and the uniaxial law is sufficient to reproduce its behaviour (Kotronis, 2000; Khebizi et al., 2014). The reinforcement can be considered as concentrate or diffuse in the concrete elements. In the first case, elements bars with non-linear behaviour, whose position and section coincide with the position and section of real reinforcement, are used. In the second case the behaviour of the mixed layers (Fig. 1) is homogenized by a law of mixtures to calculate the stress layer in proportion to each material (The adherence steel-concrete is supposed perfect; i.e, identical strain on the two materials at their frontier). Thus, in each layer (Mazars, 2001):

$$\begin{cases} \varepsilon_{concrete} = \varepsilon_{steel} \\ E = (1 - C_{a/b}) \times E_{an-concrete} + C_{a/b} \times E_{an-steel} \\ \varepsilon_{an} = (1 - C_{a/b}) \times \varepsilon_{an-concrete} + C_{a/b} \times \varepsilon_{an-steel} \\ C_{a/b} = \frac{A}{B} \end{cases}, \quad (18)$$

where E is the homogenized Young's modulus (steel + concrete), $C_{a/b}$ is the ratio surface of reinforcement, A is the relative steel air within the reinforced layer and B is the relative concrete air within the reinforced layer.

$\varepsilon_{an\text{-}concrete}$ is the inelastic concrete stain, $\varepsilon_{an\text{-}steel}$ is the inelastic steel stain; and ε_{an} is the inelastic strain homogenized of the reinforced layer (steel + concrete).

5. Applications

5.1. Column buckling

The purpose of this example is to perform a modelling of a reinforced concrete column with rectangular section subjected to an axial loading with an eccentricity e=1.50cm (Fig. 3(a)). The same column was studied experimentally by Fouré (Fouré, 1978) and numerically discretization by Franz (Franz, 1994) with multi-fiber elements (Willam-Warnke behaviour law).

In this paper, the column is modeled by 11 multi-layered elements with 2 nodes and 2 integration points. The section of each element is discretized by 6 superimposed layers, of which 4 in concrete alone and 2 in concrete and steel (Fig. 3(b)). The eccentric axial load is modelled by a centered axial load F and a bending moment M=F×e. The weight of the column is neglected. The concrete behaviour obeyed the Laborderie damage model (unilateral law behaviour). The characteristics considered for the concrete are shown on Table 1. The steel behaviour is supposed elastoplastic with kinematic hardening. The steel's characteristics used are: Young's modulus of 200,000 MPa and elastic limit of 400 MPa.

Fig. 4 shows the load variation according to the horizontal displacement of the top of the column. This figure gives a comparison between the results obtained by the present modelling, the experimental results of Fouré (1978) and those obtained by Franz (1994). As it can be seen from Fig. 4, there is a good agreement between these models.

Table 1. Concrete characteristics for Laborderie model (Khebizi and Guenfoud, 2015).

Parameter	Value
Young's modulus	30000e6 Pa
Density	2500 kg/m^3
Damage threshold in tension	220 Pa
Damage threshold in compression	9000 Pa
Damage parameter in tension	9e-3 Pa^{-1}
Damage parameter in compression	5.30e-6 Pa^{-1}
Parameter for tension	1.20
Parameter for compression	1.40
Permanent strain activation in tension	1.00e6 Pa
Permanent strain activation in compression	-40e6 Pa
Crack closure stress	1.30e6 Pa

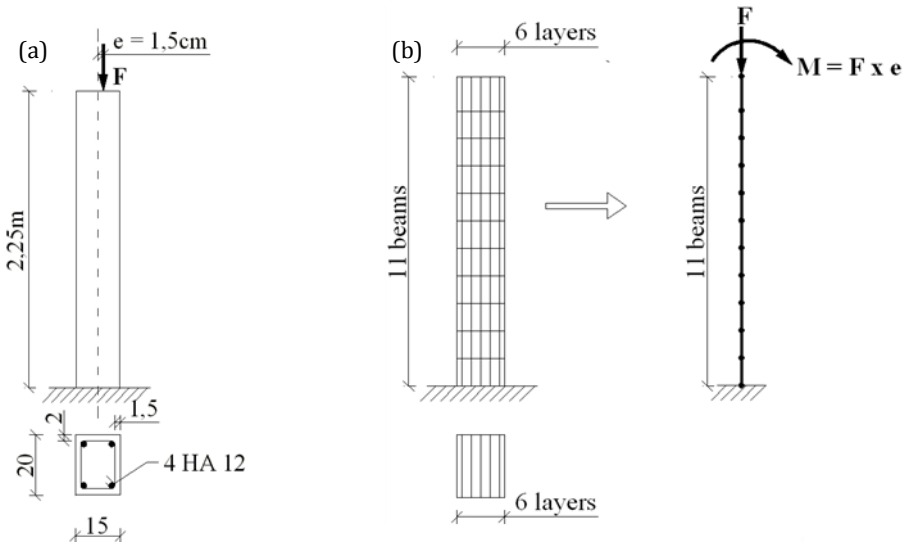

Fig. 3. Fouré Column: (a) Geometry and loading system; (b) Numerical model (2D).

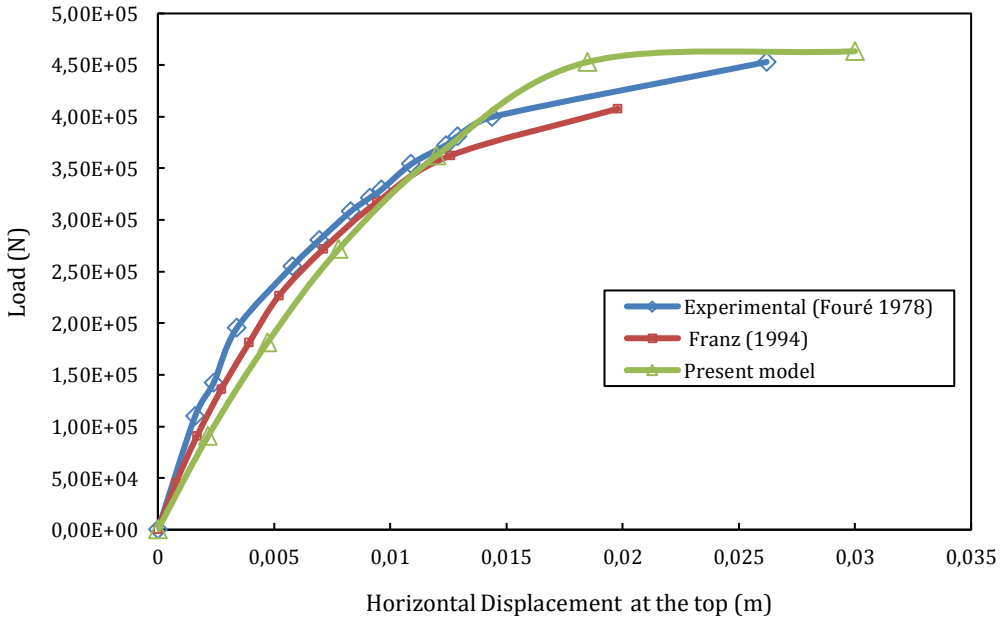

Fig. 4. Load-displacement graph of the top column.

5.2. Cyclic response modelling of a reinforced concrete beam

This example is used to validate the cyclic bending behaviour of a reinforced concrete beam (Fig. 5(a)). The loading is composed of an amplitude cycle of 1mm followed by an amplitude cycle of 2mm (Fig. 5(b)).

The model used in this paper is a structure of 20 beams elements with 2 nodes and 2 integrations points. The section of each element is discretized by 10 superimposed layers, including 8 out of concrete alone and 2 simultaneously including concrete and steel (Fig. 6). The same concrete and steel behaviour as the previous example is used in this case.

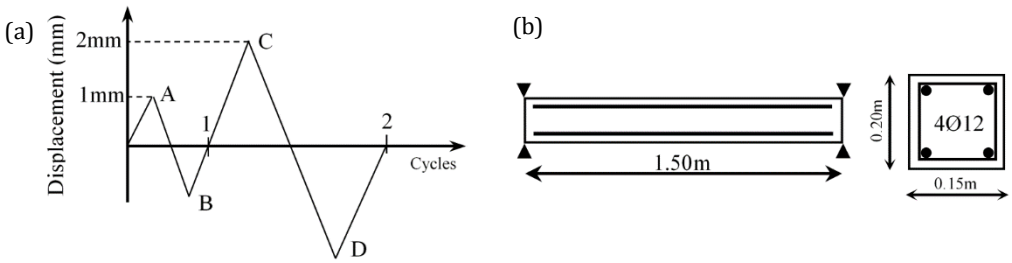

Fig. 5. Reinforced concrete beam: (a) Geometry; (b) Numerical model (2D).

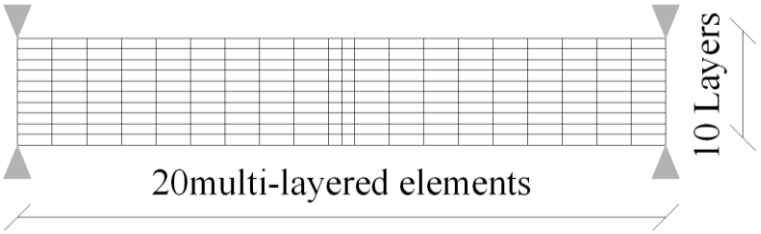

Fig. 6. Beam discretisation in multi-layered elements.

The cyclic response of the beam shown on the Fig. 7, is compared with the test results. As it can be seen from this figure, a very good coherence between the two results. This figure shows also presents a comparison of the load-displacement response obtained by the present simulation (modeling by multi-layered elements with a Laborderie law) and that obtained by Matallah (2009). The two numerical models gave similar results in first cyclic loading. However, for the second cyclic loading, a light difference is observed.

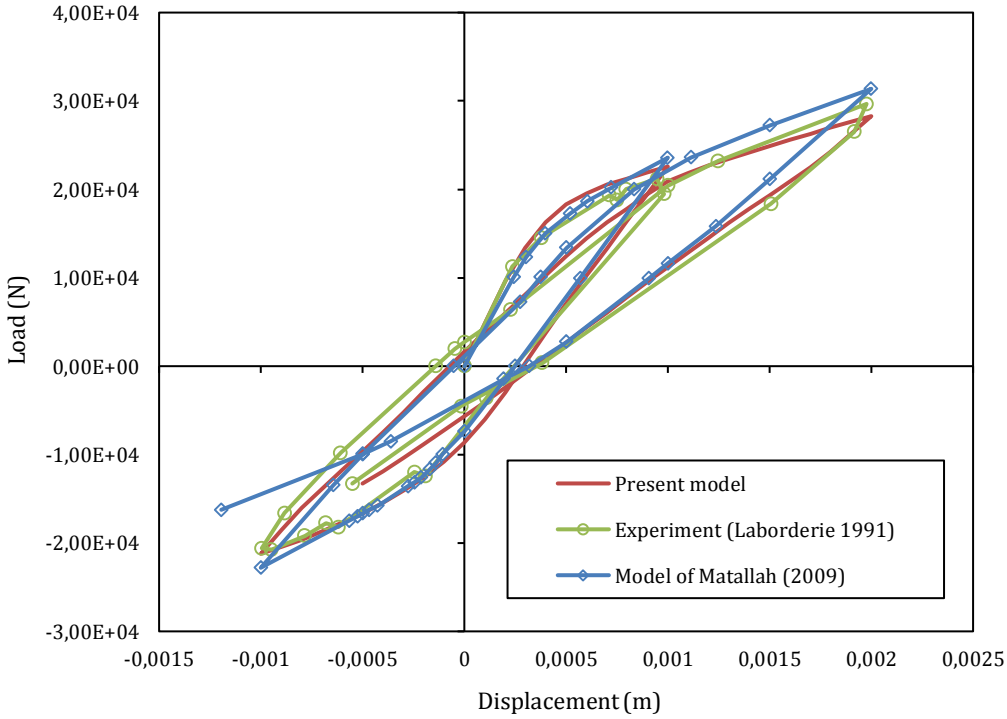

Fig. 7. Load-displacement response for different models.

Fig. 8 presents the damage chart of the beam for the first cyclic loading. In the loading state «A», the higher part of the beam is damaged (Fig. 8(a)). The loading state «B» corresponds to an opposed loading, the damage state initially product is always stored whereas a new damage state is created in the lower part of the beam (Fig. 8(b)). The damage chart of the beam during the second cyclic loading is shown in Fig. 9.

6. Conclusions

A simple modelling of the non-linear behaviour of the reinforced concrete structure is presented. It uses multi-layered beam elements which obeyed the Bernoulli hypothesis to confer to the various layers a uniaxial behaviour. It also allows the description of the structures damage state during a loading. Two examples of applications were presented. The first on is a column buckling test (Fouré column) and the second one was a beam subjected to a 3 points flexion with cyclic loading applied to the mid-span of the beam (cyclic bending). According to these examples it was noticed:

- A very good coherence between the present numerical results and the experimentation results.
- A good concordance between the results of present numerical models and those of other numerical models of references.
- The non-linear analysis reflects the real behavior of reinforced concrete structures.
- If the material is discharged after having undergone a damage state, it restores its stiffness, the crack previously open are closed again but the internal structure of material remains always damaged.

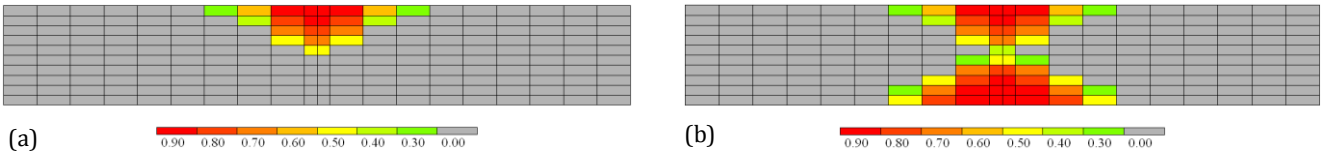

Fig. 8. Damage chart in tension «D1» for the first cyclic loading: (a) Loading State «A»; (b) Loading State «B».

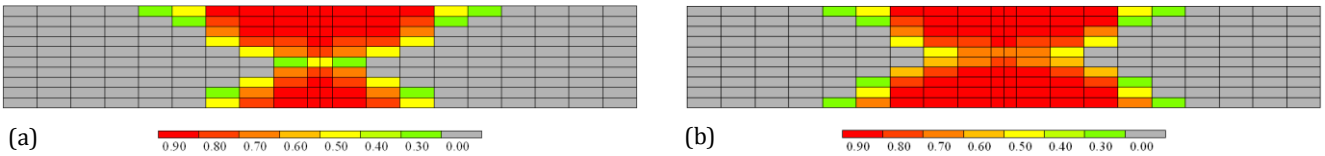

Fig. 9. Damage chart in tension «D1» for the second cyclic loading: (a) Loading State «C»; (b) Loading State «D».

REFERENCES

Davenne F, Ragueneau F, Mazars J (2003). Efficient approaches to finite element analysis in earthquake engineering. *Computers and Structures*, 81, 1223-1239.

Fouré B, Virlogeux M (1978). Le flambement des poteaux compte tenu du fluage du béton. *Annls. de l'I.T.B.T.P.*, No 359.

Franz J (1994). Modélisation Elastoplastique Avec Endommagement du Béton de Structures. Application Aux Calculs Statiques et Dynamiques de Structures en Béton Arme et Béton Précontraint. *Ph.D. Thesis*, Ecole Nationale des ponts et Chaussées, Paris, France.

Ghavamian S (2001). *MECA project benchmark: Three dimensional nonlinear constitutive models of fractured concrete. Evaluation-Comparison-Adaptation*. Edited by EDF R&D.

Khebizi M (2015). Comportement Mécanique D'une Demelle Duperficielle Dous l'effet D'un Déisme. *Ph.D. thesis*, 8 Mai 1945 University of Guelma, Guelma, Algéria.

Khebizi M, Guenfoud M (2015). Numerical modelling of the damaging behaviour of the reinforced concrete structures by multi-layers beams elements. *Computers and Concrete*, 15(4), 547-562.

Khebizi M, Guenfoud H, Guenfoud M (2014). Modélisation des poutres en béton arme par des éléments Multicouches. *Courrier du Savoir*, 18, 111-115.

Kotronis P (2000). Cisaillement Dynamique de Murs en Béton Armé. Modèles simplifies 2D et 3D. *Ph.D. thesis*, Ecole normale supérieure de Cachan, Cachan, France.

Kotronis P, Ragueneau F, Mazars J (2005). A simplified modelling strategy for R/C walls satisfying PS92 and EC8design. *Engineering Structures*, 27, 1197-1208.

Laborderie C (2003). Stratégies et Modèles de Calculs pour les Structures en Béton. *Thèse d'habilitation à diriger les recherches*, Université de Pau et des Pays de l'Adour.

Matallah M, Laborderie C (2009). Inelasticity–damage-based model for numerical modeling of concrete cracking. *Engineering Fracture Mechanics*, 76, 1087-1108.

Mazars J, Ragueneau F, Kotronis P (2001). La simulation numérique, la simulation physique, 2 approches complémentaires pour l'analyse des effets des risques naturels : le cas des séismes. *XVème Congres Français de Mécanique,* 3–7 September, 719-725, Nancy, France.

Ragueneau F (1999). Fonctionnement dynamique des structures en béton – Influence des comportements hystérétiques locaux. *Ph.D. Thesis*, Ecole normale supérieure de Cachan, Cachan, France.

Ragueneau F (2006). Comportements endommageants des matériaux et des structures en béton armé. *Mémoire d'habilitation à diriger des recherches*, Université Pierre et Marie Curie, Paris, France.

Challenge Journal of Structural Mechanics

Effect of time step size on stress relaxation

Abdullah Fettahoğlu

Department of Civil Engineering, Eastern Mediterranean University, Famagusta, North Cyprus, 10 Mersin, Turkey

ABSTRACT

Many materials used in industry show time and temperature dependant stress strain relationship. While essentially most of the materials exhibit stress relaxation or in general viscoelastic material properties, some of them are assumed as linear elastic to be able to make their stress calculations simpler. On the contrary, there are some materials showing intense viscoelastic stress strain relationship even at lower temperatures and short time periods. Most of these materials are employed in construction industry as pavements on roads or bridges and needed a better understanding of their viscoelastic material properties and calculation methods for their design. For a better understanding and comparison between several material products in industry, their stress strain behavior shall be evaluated. Stress relaxation of materials, which shows time and temperature dependant properties, is investigated in this paper. For that reason first, relaxation test results existed in the literature are used to verify the numerical stress relaxation calculation of commercial FEM program, ANSYS. Second, the determination of Prony series parameters and the commands to be entered in ANSYS to perform stress relaxation are given. Finally, the amount of error in the numerical calculation depending on time step sizes at different temperatures is presented.

ARTICLE INFO

Article history:
Received 27 September 2016
Accepted 13 November 2016

Keywords:
ANSYS
Prony series
Time step size
Viscoelasticity

1. Introduction

Viscoelasticity is an interesting topic to model time and temperature dependant material behavior. Therefore, several researchers use viscoelasticity to predict stress strain relationship of materials, which are of interest. (Delgadillo R, 2010; Findley WN et al., 1989). In this study, using viscoelasticity by means of Prony series in ANSYS is explained first. Then, stress relaxation test results of Monismith and Secor (1962) are used to indicate the validity of Prony series for viscoelastic analysis. Afterwards, amount of error occurred in ANSYS (2014) calculations depending on selected time step size is illustrated. Numerical ANSYS calculations and stress relaxation tests are presented at three different isothermal environmental temperatures to investigate the effect of time step size at different temperatures on the values calculated by ANSYS.

2. Properties of Tested Specimen

An 85-100 penetration asphalt cement is used in stress relaxation tests done by Monismith and Secor (1962). The properties of mix tested is briefly given below,

Test name	Result
• Penetration at 77°F, 100gm, 5 secs.	96
• Penetration at 39.2°F, 200gm, 60 secs.	24
• Penetration proportion	25
• Flashpoint, Pensky-Martens, °F	445
• Viscosity at 275°F, SSF	138
• Heptane-xylene Equivalent	20/25
• Soften point, Ring and Ball, °F	110
• Thin – film – oven – test, 325°F, 5h:	
◦ Percentage weight lose	0.51
◦ Percentage penetration back gained	53
◦ Ductility of rest	100+

* *Corresponding author*. Tel.: +90-392-6301111 ; E-mail address: abdullah.fettahoglu@emu.edu.tr (A. Fettahoğlu)
ISSN: 2149-8024 / DOI: https://doi.org/10.20528/cjsmec.2016.11.029

In addition to standardized tests, a lot of tests are done in this research paper of Monismith and Secor (1962), which provides detailed information regarding type of tests and methods employed. Stress relaxation tests are performed using universal test machine, but the hydraulic loading system of the test machine is not used. Here, only the relaxation curves obtained from these tests are employed to make a benchmark comparison with the numerically obtained stress relaxation curves using ANSYS.

3. Using Prony Series in ANSYS

In this section, the background of viscoelastic equations employed by ANSYS is explained (2014). A material is called viscoelastic, when its strain comprises both elastic (reversible) and viscos (irreversible) parts. Under loading elastic strains develop instantly, whereas developing viscos strains take time. Such materials behave at higher temperatures like a liquid, but at lower temperatures like a stiff body. The viscoelastic material behavior in ANSYS is defined using the theory of Thermorheological Simplicity (TRS). TRS means: The reaction of a material under loading at higher temperatures and a small time period is similar to the reaction of same material at lower temperatures and a larger time period. ANSYS employs two different methods to represent viscoelastic material behavior of bodies, namely, generalized Maxwell elements (for small strains and small displacements) and Prony series (for small strains and large displacements). In this study, Prony series method is used to represent stress relaxation, since it is more robust and reliable than generalized Maxwell elements method. The equations of viscoelasticity by means of Prony series are given below,

$$s_{ij}(t) = \int_0^t 2 \cdot G(t-\tau).\frac{de_{ij}}{d_\tau} d\tau \,, \tag{1}$$

$$\sigma_K(t) = \int_0^t 3 \cdot K(t-\tau) \cdot \frac{d\Delta}{d\tau} d\tau \,, \tag{2}$$

$$\sigma_{ij}(t) = s_{ij}(t) + s_{ij} \cdot \frac{\sigma_K(t)}{3} \,. \tag{3}$$

Replacing Eqs. (1, 2) in Eq. (3), the following equation is supplied,

$$\sigma_{ij}(t) = \int_0^t 2 \cdot G(t-\tau).\frac{de_{ij}}{d_\tau} d\tau + \delta_{ij} \cdot \int_0^t K(t-\tau) \cdot \frac{d\Delta}{d\tau} d\tau \,. \tag{4}$$

The definitions of symbols in Eqs. (1-4) are given below,

σ_{ij} : Cauchy stress
e_{ij} : Deviatoric part of strain
Δ : Hydrostatic part of strain
$G(t)$: Deviatoric relaxation module
$K(t)$: Hyrostatic relaxation module
t : Real time
τ : Elapsed time

For Prony series (Park and Kim, 2001; Ghoreishy, 2012), the expressions of relaxation moduli are given as

$$G(t-\tau) = G_\infty + \sum_{i=1}^{n_G} G_i \cdot e^{-(t-\tau)/\tau_i^G} \,, \tag{5}$$

$$K(t-\tau) = K_\infty + \sum_{i=1}^{n_K} K_i \cdot e^{-(t-\tau)/\tau_i^K} \,, \tag{6}$$

whereas,

$$G_0 - G_\infty = \sum_{i=1}^{n_G} G_i \,, \tag{7}$$

$$K_0 - K_\infty = \sum_{i=1}^{n_K} K_i \,. \tag{8}$$

Or with introducing relative moduli,

$$a_i^G = \frac{G_i}{G_0}, \qquad a_\infty^G = \frac{G_\infty}{G_0} \,, \tag{9a}$$

$$a_i^K = \frac{K_i}{G_0}, \qquad a_\infty^K = \frac{K_\infty}{K_0} \,, \tag{9b}$$

expressions of relaxation moduli result in following forms:

$$G(t-\tau) = G_0 \cdot \left[a_\infty^G + \sum_{i=1}^{n_G} a_i^G \cdot e^{-(t-\tau)/\tau_i^G}\right], \tag{10}$$

$$K(t-\tau) = K_0 \cdot \left[a_\infty^K + \sum_{i=1}^{n_K} a_i^K \cdot e^{-(t-\tau)/\tau_i^K}\right]. \tag{11}$$

4. Verification of ANSYS Results

A three dimensional brick element is modeled in ANSYS to enable visual observation of shear deformation. Afterwards, this three dimensional geometry is reduced into a single freedom system using necessary restraints, where only shear deformations are permitted. Below, Figs. 1 and 2 serve for illustration of applied restraints and deformed shape of FE- model used in this study.

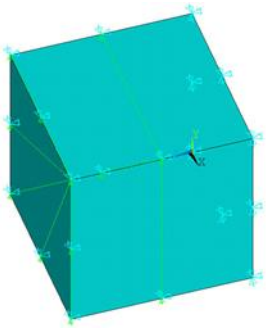

Fig. 1. The geometry and restraints of FE- model.

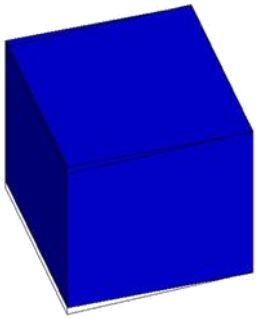

Fig. 2. The deformed geometry of FE- model.

4.1. Stress relaxation at 4.444°C

First, using Eq. (12), the values of shear relaxation module is calculated at specific times from the test output provided by Monismith and Secor (1962).

$$s_{11}(t) = G(t) \cdot 2e_{11} \,. \tag{12}$$

Second, to calculate the constants of Prony series, the values of shear relaxation module, $G(t)$, is written in a text file.

```
/temp,4.4444
0               32316.48878
0.205789129     26394.01207
0.57880812      20759.52444
0.790884086     19802.05426
0.977393582     18700.58954
1.997118533     15781.42751
2.991277014     14268.54982
3.985016372     13127.81385
4.977917485     12190.91432
5.980458415     11549.48410
7.992246234     10655.59592
9.962960052     9774.798151
11.93996071     9376.475593
```

Third, this text file has been read into ANSYS using Viskoelastic Material Curve Fiting (VMCF). Then, again using VMCF the constant of Prony series are determined as follows,

$PRXY = 0.4$ (This value is arbitrarily selected to be able to enter K_0 in ANSYS)

$EX = 2 \cdot G_0 \cdot (1 + PRXY) = 90486.1686$

$a_1^K = 0.3494$

$\tau_1^K = 4.2965$

$a_2^K = 0.38013$

$\tau_2^K = 0.36619$

Finally, commands required to be entered in ANSYS to perform the analysis are determined as follows,

```
MP, EX, 1, 90486.1686
MP, PRXY, 1, 0.4
TB, PRONY, 1, ,2, SHEAR
TBDATA, 1, 0.34941, 4.2965
TBDATA, 3, 0.38013, 0.36619
```

The results given in Fig. 3 show that Prony series can represent the test data good in general, nevertheless the initial stress values cannot be approximated like other time points.

4.2. Stress relaxation at 25°C

Because the steps of procedure explained in the previous subsection applies also here, solely the data used at 25°C is given here.

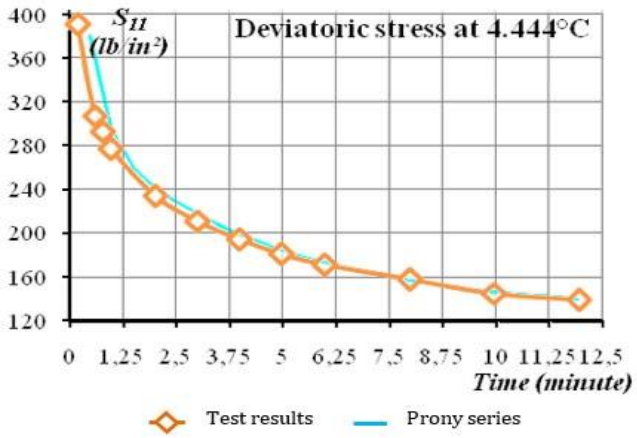

Fig. 3. Comparison of stress relaxation test results of Monismit and Secor (1962) with ANSYS results at 4.4444°C under constant strain e_{11}=0.0074.

The text file of $G(t)$:

```
/temp,25
0              12660.930968302
0.171748276     6800.598244922
0.359977447     6012.191506357
0.577698747     5609.332973279
0.795420046     5412.624705174
1.000130112     5252.897591472
2.025415275     4813.057903990
3.034219543     4608.481305161
4.056468751     4539.239994788
6.055427853     4372.431383435
8.068265603     4235.522428834
10.07763369     4189.099277561
12.09047144     4120.644800261
14.09290020     4014.422335484
16.03027280     3968.786017284
18.00798022     3961.704519632
19.98091686     3961.704519632
```

Constants of Prony series are as follows,

$PRXY = 0.4$ (This value is arbitrarily selected to be able to enter K_0 in ANSYS)

$EX = 2 \cdot G_0 \cdot (1 + PRXY) = 35450.606716$

$a_1^K = 0.13548$

$\tau_1^K = 0.56364$

$a_2^K = 0.45824$

$\tau_2^K = 0.066043$

$a_3^K = 0.093375$

$\tau_3^K = 5.4215$

The commands required to be entered in ANSYS to perform the analysis are as follows,

```
MP, EX, 1, 35450.606716
MP, PRXY, 1, 0.4
TB, PRONY, 1, , 3, SHEAR
TBDATA, 1, 0.13548, 0.56364
TBDATA, 3, 0.45824, 0.066043
TBDATA, 5, 0.093375, 5.4215
```

The results given in Fig. 4 show the same result obtained at 4.444°C, that Prony series can represent the test data good in general, nevertheless the initial stress values cannot be approximated like other time points.

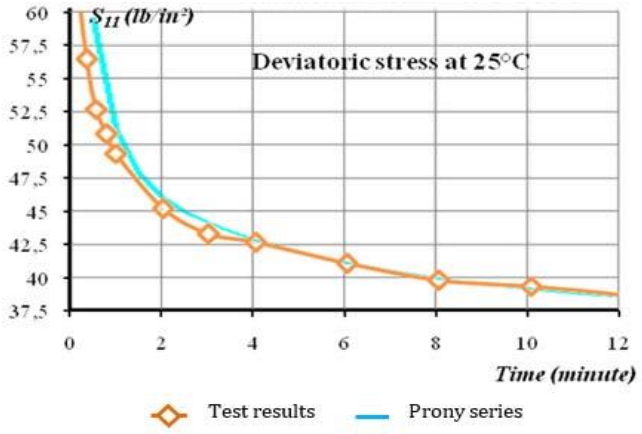

Fig. 4. Comparison of stress relaxation test results of Monismith and Secor (1962) with ANSYS results at 25°C under constant strain e_{11}=0.0047.

4.3. Stress relaxation at 60°C

Because the steps of procedure explained in the previous subsection applies also here, solely the data used at 60°C is given here.

The text file of $G(t)$:

```
/temp,60
0               3067.281051
0.071628428     2139.044636
0.182326906     1951.960548
0.337386173     1793.313241
0.536399247     1715.935261
0.758203185     1650.829999
0.924250903     1614.311184
1.356056367     1557.287954
1.942514117     1508.496424
2.939207407     1459.704894
3.935493717     1418.995396
4.976140815     1394.599631
5.950450221     1390.558614
6.946736532     1370.203866
7.87668515      1358.080817
```

Constants of Prony series are as follows,

$PRXY = 0.4$ (This value is arbitrarily selected to be able to enter K_0 in ANSYS)

$EX = 2 \cdot G_0 \cdot (1 + PRXY) = 8588.3871$

$a_1^K = 0.15448$

$\tau_1^K = 0.15675$

$a_2^K = 0.09066$

$\tau_2^K = 0.74528$

$a_3^K = 0.23555$

$\tau_3^K = 0.00090614$

$a_4^K = 0.087006$

$\tau_4^K = 3.8438$

The commands required to be entered in ANSYS to perform the analysis are as follows,

```
MP, EX, 1, 8588.3871
MP, PRXY, 1, 0.4
TB, PRONY, 1, , 4, SHEAR
TBDATA, 1, 0.15448, 0.15675
TBDATA, 3, 0.09066, 0.74528
TBDATA, 5, 0.23555, 0.00090614
TBDATA, 7, 0.087006, 3.8438
```

Fig. 5 supports the results obtained in Figs. 3 and 4, that the Prony series are in good agreement with the test data except the initial values.

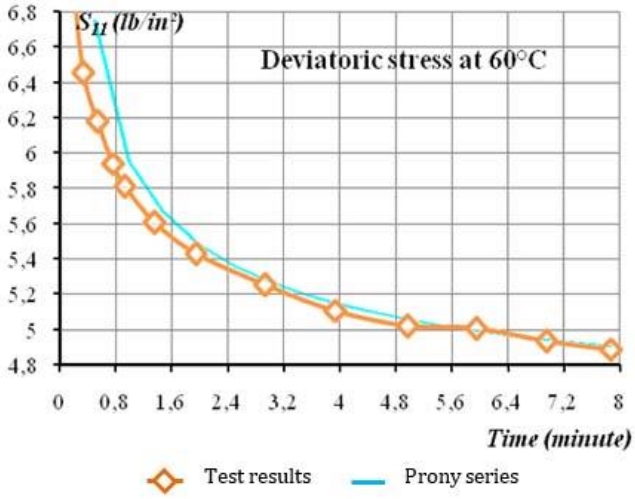

Fig. 5. Comparison of stress relaxation test results of Monismith and Secor (1962) with ANSYS results at 60°C under constant strain e_{11}=0.0018.

5. Results and Discussion

From the assessment of Figs. 3, 4 and 5; it is seen that Prony series approximate the relaxation test data well except the initial values. The reason of this error is that the relaxation test data is composed of scattered test data, whereas numerically calculated stress values using Prony series form a smooth curve. In addition to Figs. 3-5, Figs. 6-8 are given below to indicate the amount of error in calculated stress depending on selected time step size in minutes. It is concluded that the error in calculated stress values rise proportional to time step size. Briefly, the smaller time step size, the better for accuracy of stress results calculated using Prony series in ANSYS.

6. Conclusions

In this study it is verified that Prony series in ANSYS can approximate the stress strain behavior of viscoelastic bodies. In addition the effect of time step size on the amount of error occurred in calculated stress values is presented. Briefly, Prony series can approximate the general stress relaxation test result successfully except for the initial stress values due to the scattered stress

values of test data versus smooth transition of Prony series curve. This result is supported by the curves corresponded at 4.444°C, 25°C and 60°C. Later conclusion of this study is, the smaller the selected time step size for numerical calculation using Prony series, the better accuracy is obtained.

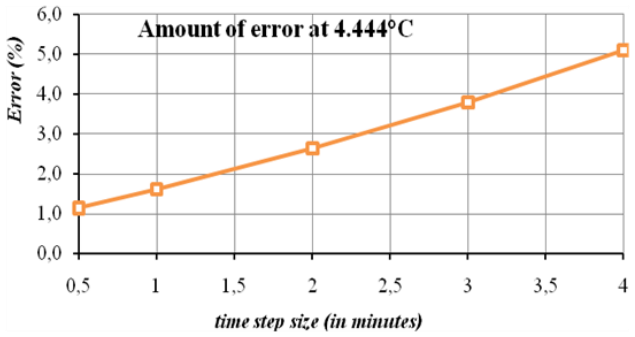

Fig. 6. The amount of error in max stress depending on time step size (in minutes) at 4.4444°C.

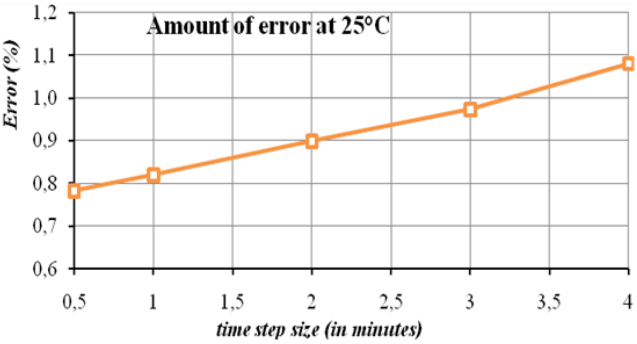

Fig. 7. The amount of error in max stress depending on time step size (in minutes) at 25°C.

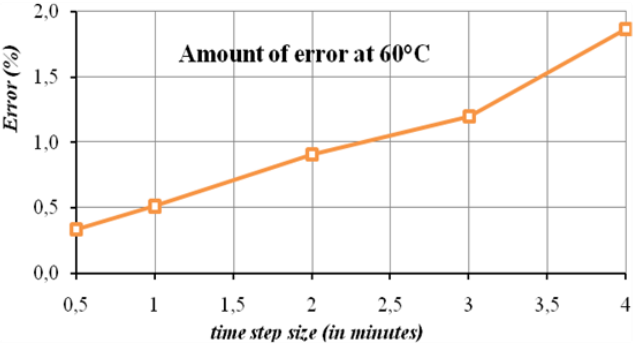

Fig. 8. The amount of error in max stress depending on time step size (in minutes) at 60°C.

REFERENCES

ANSYS (2014). User Manuals, Swanson Analysis System, USA.

Delgadillo R, Bahia H (2010). The relationship between nonlinearity of asphalt binders and asphalt mixture permanent deformation. *Journal of Road Materials and Pavement Design*, 1(3), 653-680.

Findley WN, Lai JS, Onaran K (1989). Creep and Relaxation of Nonlinear Viscoelastic Materials with an Introduction to Linear Viscoelasticity, Dover Publications.

Ghoreishy MHR (2012). Determination of the parameters of the Prony series in hyper-viscoelastic material models using the finite element method. *Materials and Design*, 35, 791-797.

Kontou E, Spathis G, Georgiopoulos P (2014). Modeling of nonlinear viscoelasticity-viscoplasticity of bio-based polymer composites polymer degradation and stability. *Polymer Degradation and Stability*, 110, 203-207.

Lee HJ, Kim YR (1998). A uniaxial viscoelastic constitutive model for asphalt concrete under cyclic loading. *Journal of Engineering Mechanics-ASCE*, 124(11a), 1224-1232.

Lee HJ, Kim YR (1998). A viscoelastic continuum damage model of asphalt concrete with healing. *Journal of Engineering Mechanics-ASCE*, 124(11b), 1-9.

Lewandowski M, Gajewski M, Jemioło S (2014). The material anisotropy ınfluence on modelling of rutting test with application of linear viscoelasticity constitutive equations. *Procedia Engineering*, 91, 93-98.

Mezger TG (2006). The Rheology Handbook, 2nd ed., Vincentz Network, Hanover, Germany.

Monismith CL, Secor KE (1962). Viscoelastic Behaviour of Asphalt Concrete Pavements. *Report*, Institute of Transportation and Traffic Engineering, University of California, Berkeley.

Park SW, Kim YR, Schapery RA (1996). A viscoelastic continuum damage model and its application to uniaxial behavior of asphalt concrete. *Mechanics of Materials*, 24, 241-245.

Park SW, Kim YR (2001). Fitting Prony-series viscoelastic models with power-law pre-smoothing. *Journal of Materials in Civil Engineering*, 13(1), 26-32.

Schapery RA (1984). Correspondence principles and a generalized J-integral for large deformation and fracture analysis of viscoelastic media. *International Journal of Fracture*, 25,195-223.

Schapery RA, Compos. Mat., Chap. 4, S. 85- 168 (1974). Viscoelastic Behaviour and Analysis of Composite Materials, 2, Academic, San Diego, USA.

Williams ML (1964). Structural analysis of viscoelastic materials. *AIAA Journal*, 2(5), 785-808.

Young K, And Choi (2011). Visco-elastic analysis of the elastomeric binder shear resistance in relation to asphalt rutting. *Road Materials and Pavement Design*, 12(4), 767-794.